THERMOKARST DISTRIBUTION AND SUSCEPTIBILITY IN YUKON: LAKES, LANDSLIDES AND PINGOS

OLIVER KARREN KIENZLE
Bachelor of Science, University of Lethbridge, 2019

A thesis submitted
in partial fulfilment of the requirements for the degree of

MASTER OF SCIENCE

in

GEOGRAPHY

Department of Geography and Environment
University of Lethbridge
LETHBRIDGE, ALBERTA, CANADA

THERMOKARST DISTRIBUTION AND SUSCEPTIBILITY IN YUKON: LAKES, LANDSLIDES AND PINGOS

OLIVER KARREN KIENZLE

Date of Defence: April 16th 2024

Dr. Hester Jiskoot Thesis Supervisor	Professor	Ph.D.
Dr. Craig Coburn Thesis Examination Committee Member	Professor	Ph.D.
Dr. René Barendregt Thesis Examination Committee Member	Professor Emeritus	Ph.D.
Dr. Laura Chasmer Chair, Thesis Examination Committee	Associate Professor	Ph.D.

Abstract

The most tangible consequence of permafrost thaw is thermokarst, which is landscape destabilization resulting from ground ice melt. The main objective of this thesis was to model and map thermokarst susceptibility across Yukon, Canada. An inventory of 3376 historically mapped thermokarst landform point locations was extracted from the Yukon Geological Survey's Digital Surficial Geology dataset. Of these, 25 lakes, 27 landslides and 93 pingos in the Dawson City study area were manually delineated on the World Imagery baselayer in order to assess their morphology and distribution relative to similar landforms in other regions. Subsequently, generalized linear models of thermokarst susceptibility in Yukon were constructed using a range of topographic, geologic, environmental and climatic predictor variables from existing regional or global datasets. A novel potential surface radiation adjustment was developed to correct for seasonal snow cover. Using the mapped thermokarst landforms in the Dawson City study area as a training dataset set, the resulting optimal lake and landslide susceptibility models use slope as the sole predictor variable, while the pingo susceptibility model uses profile curvature. Overall, 3, 34 and 0.1 % of Yukon is modelled as being highly susceptible to thermokarst lake, landslide and pingo development, respectively. The models were evaluated using the Yukon thermokarst point location dataset, randomly distributed points, and select multivariate logistic models. The thermokarst lake susceptibility model performed best overall. This study shows that relatively simple modelling techniques can be effective in mapping thermokarst susceptibility, and highlights the importance of rigorous, up-to-date thermokarst landform inventories to aid in future modelling efforts.

Acknowledgements

I would like to thank Ileana and my parents for their love and support throughout this thesis. I love you all, and I would not have achieved this without you.

Thank you to Hester for pushing me to be systematic, detail-oriented and critical of what I was doing and why I was doing it. I learned a lot about thermokarst with your help, but I learned much more about myself.

Thank you to Craig Coburn for getting me to distrust every black box, and to René Barendregt for helping me to understand Yukon's glacial history and its impacts on today's landscape.

Thank you to Kyle Bexte, Seamus Daly and Scott Vegter for showing me how this is all done, and for being good friends throughout this process. I acknowledge that Dr. Phil Bonnaventure initiated this research project. I am grateful for funding received from RemoteEx through Hester, which enabled me to attend UNIS in Svalbard to study snow and avalanche dynamics. Thank you to Brendan O'Neill at Natural Resources Canada, Derek Cronmiller and especially to Panya Lipovsky for helping me to find resources. Thank you to Laura Chasmer for providing feedback on the first chapters of this thesis.

Table of Contents

List of Tables

List of Figures

List of Abbreviations

AIC	Akaike Information Criterion
CDEM	Canadian Digital Elevation Model
CSS	Continuous Snow Season
DEM	Digital Elevation Model
FSS	Full Snow Season
GLM	Generalized Linear Modelling
IPA	International Permafrost Association
PRR	Potential Relative Radiation
YGS	Yukon Geological Survey

Chapter 1. Introduction

1.1 Permafrost and Thermokarst

Permafrost thaw is accelerating due to climate change, and its impacts can be observed both in the global climate system and at local scales. Permafrost is ground which remains at or below 0 °C for two or more consecutive years (Harris et al., 1988). These ground materials can include mineral and organic soils, sediments, bedrock, water, and air. Since permafrost is defined by the thermal state of the ground, it is affected by the climate of the past and the present and is thus sensitive to climate change. In addition, permafrost occurrence is influenced by hydrology, vegetation cover and edaphic conditions such as soil texture and organic matter content, as well as by anthropogenic disturbance (Nossov et al., 2013). The climatic limit of stable permafrost is a mean annual air temperature of 1 °C (Smith and Riseborough, 2002), though relic permafrost exists in some areas as a result of Pleistocene climates (Mackay et al., 1972).

Globally, permafrost mainly occurs in Arctic, Antarctic and alpine regions and is present beneath approximately 11 % of the Earth surface (Obu, 2021). Permafrost distribution is commonly classified according to percentage areal extent, following e.g. Heginbottom et al. (1993): continuous (90–100 %), extensive discontinuous (50–90 %), sporadic discontinuous (10–50 %), and isolated patches (0–10 %). Permafrost thickness (vertical extent to base) in North America ranges from around 1 m to over 500 m (French, 2018). In Canada, permafrost is estimated to underlie 34–46 % of the land and is found throughout each of the territories and in the northern portions of British Columbia, Alberta, Saskatchewan, Manitoba, Ontario, Quebec and Newfoundland and Labrador (Obu et al., 2019). Details and figures are provided in Chapter 2.

The layer of ground immediately above permafrost is called the active layer because it undergoes seasonal freeze-thaw cycles and, therefore, it is the most biologically and hydrologically active zone in a permafrost landscape (Bonnaventure and Lamoureux, 2013). Active layer depths across Canada were measured from 1990 to 2021 to be between 25 and 362 cm in depth, with an average of 84 cm (Nelson et al., 2021). The active layer is thickest at the southern extent of discontinuous permafrost and thinnest in the high Arctic. Active layer depth increases due to permafrost thaw in response to a warming climate or to disturbance to the physical properties of the land surface. Eventually, this process of permafrost thaw can result in the development of unfrozen zones called taliks and, eventually, complete permafrost collapse (O'Neill et al., 2020). The current global trend is towards increased active layer thickness, rising permafrost temperature and permafrost thaw (Biskaborn et al., 2019). The mean active layer thickness in the Northern Hemisphere has increased from 127 to 145 cm between 2000 and 2018 (Li et al., 2022a). Permafrost temperatures in the Northern Hemisphere have increased by up to 2 °C from the 1970s to 2009 (Romanovsky et al., 2010), and the Intergovernmental Panel on Climate Change's Sixth Assessment Report synthesizes that global permafrost temperature had increased by 0.29 °C ± 0.12 °C between 2007 and 2016 (Gulev et al., 2021).

Permafrost aggradation and seasonal freeze-thaw processes cause cryoturbation, which is the horizontal and vertical movement in sediment or soil due to contraction and expansion caused by the repeated growth and melt of ground ice (Harris et al., 1988). Several distinct periglacial landforms are formed in permafrost regions, which can be broadly divided into variations of geometric shapes, called patterned ground, and various types of frost mounds. Patterned ground includes sorted circles, sorted stripes, ice-wedge polygons, and on sloping ground solifluction lobes and block fields; while frost mounds include frozen earth hummocks, palsas and pingos (Washburn, 1956; Péwé, 1963; Lundqvist, 1969; Seppälä, 1988; Hallet, 1990; Price, 1991; French, 2018). The occurrence

and distribution of these landforms are related to the seasonal and climatic variations, the earth surface material and topography, and the presence of ground ice (O'Neill et al., 2019).

Permafrost thaw can have ecological and societal impacts at local and global scales. The term thermokarst describes both the process of thermal erosion in permafrost and the landforms that result from it. At the local scale, thermokarst can form where ground ice is present within the permafrost (Murton, 2009). Similar to limestone karst, a landscape characterized by chemically eroded caves and sinkholes (van Brahana, 2008), thermokarst landscapes are characterized by wetlands, lakes and slumps. Thermokarst landforms can develop rapidly over the course of days during summer months, or more slowly over the course of multiple summers.

Three broad types of thermokarst landforms exist: lakes, wetlands, and hillslope failures (Kokelj and Jorgenson, 2013), though as many as 23 unique thermokarst landform types have been identified by Jorgenson (2013). Landscape features that were formed through ground ice aggradation in permafrost, such as pingos and ice-wedge polygons, are at particular risk of degrading and developing into thermokarst landforms, as are coastal cliffs and river banks (Karjalainen et al., 2020). The abrupt thaw processes and related landscape changes associated with thermokarst can substantially affect the thermodynamics of permafrost by exposing the top of it to the atmosphere. This creates a local positive feedback loop serving to accelerate permafrost thaw (Kokelj and Jorgenson, 2013). Thermokarst is a hazard for people that live and work in permafrost regions since human infrastructure depends on ground stability (Orlov et al., 2020). Adaptation to and mitigation of permafrost thaw is therefore an important part of life in northern communities (e.g. Benkert et al. 2015a; 2015b; 2016; Daly et al., 2022).

On a global scale, the collapse of boreal permafrost in the Northern Hemisphere has been identified as a climate tipping point, a threshold in the global climate system

which triggers self-reinforcing positive feedback loops with irreversible consequences (Lenton, 2012; Armstrong McKay et al., 2022). This is in large part due to the amount of organic material stored in permafrost soils and deep sediments, estimated to be in the order of 1000 billion tons (Schuur and Abbott, 2011; Schuur et al., 2015). As permafrost thaws and becomes biologically active, this organic material begins to decompose and is released into the atmosphere as either methane or carbon dioxide, depending on the water content of the thawed ground (Schädel et al., 2016; Turetsky et al., 2019). Inundation of the active layer as a result of ground ice melt provides the anaerobic conditions necessary for methane production (Walter et al., 2007). Because of the impact that permafrost thaw has both on the global climate system and on human infrastructure, it is a key concern both for people that live above and near permafrost and for the rest of the world.

1.2 Thesis Research Objectives

The objectives of this thesis research project are the following:

1. Describe the distribution and characteristics of manually mapped thermokarst lakes, landslides and pingos across the landscape for an area of 9103 km^2 within the Dawson City study area, Yukon, Canada.
2. Use topographical, geological and climatological data to develop statistical models to map the susceptibility of the development of thermokarst lakes, landslides and pingos within the Dawson City study area.
3. Apply the optimal statistical models to map thermokarst susceptibility across the whole of the Yukon, and validate the models using the mapped distribution of thermokarst lakes, landslides and pingos from the Yukon Geological Survey (2020a).

1.3 Thesis Structure

This master's thesis consists of six chapters. The first introduces permafrost and thermokarst and their importance to people, as well as listing the objectives of this project. The second chapter is a literature review synthesizing research on permafrost distribution and thaw, thermokarst, ground ice and hazard mapping as they pertain to this project. The third chapter describes the study area, data and methods used in the analysis. The fourth chapter presents the results of those analyses. The fifth chapter is a discussion of the limitations and potential applications of this work, and the final chapter is a summary and conclusion, with suggestions for future research.

Chapter 2. Permafrost and Thermokarst

This chapter is a literature review synthesizing research on permafrost distribution and thaw, thermokarst, ground ice and hazard mapping as they pertain to the thesis research.

2.1 Permafrost Distribution

Mapping permafrost presents an interesting challenge, since its subterranean nature makes it hard to verify without field excavation (Heginbottom, 2002; Westermann et al., 2015) or borehole temperature interpretation (Ran et al., 2022). Several permafrost maps exist for the Northern Hemisphere: the International Permafrost Association (IPA) produced the Circum-Arctic Map of Permafrost and Ground Ice Conditions at a 1:10 000 000 scale (called the IPA map) (Heginbottom et al., 1993), Obu et al. (2019) generated a modelled estimate of circum-Arctic permafrost occurrence at a 1 km^2 resolution, and, for Canada, the Geological Survey of Canada produced the Permafrost Map of Canada at a 1:7 500 000 scale, which is also classified by distribution and ground ice content (Heginbottom et al., 1995). Neither of these maps give enough detail to be useable for planning or hazard mitigation purposes. Based on the IPA map, an estimated 12.8–17.8 % of the Northern Hemisphere is underlain by permafrost (Zhang et al., 2000). As of 2022, the scientific consensus is that approximately 15 % of the Northern Hemisphere is underlain by permafrost (Figure 2.1) (Obu et al., 2019; Obu, 2021; Ran et al., 2022). The southern limit of lowland permafrost in Canada is around 50°N, occurring in Saskatchewan, Manitoba, Ontario and Quebec, with these regions being dominated by permafrost peatlands (Beilman et al., 2001). In Alberta and British Columbia the southern limit of lowland permafrost is closer to 55°N, while alpine permafrost is present along the

extent of the Canadian Rockies. Alpine permafrost has been observed at an elevation of 2224 m at 50°N in Alberta (Harris and Brown, 1978).

Vegetation plays a significant role in modifying the thermal regime of permafrost (Brown, 1963). For example, a difference in mean annual ground surface temperature of 0.7 °C was observed in adjacent permafrost sites in the high Arctic with different ground cover, while mean annual ground temperature at 30 cm depth was identical between the sites (Guglielmin et al., 2008). The relationship between vegetation and permafrost is complex because both of these systems are dynamic, and in many cases each only exists because of the other. Key examples of plant communities with well-studied effects on ground temperature are peatlands and Arctic shrublands. The *Sphagnum* mosses and lichens which constitute peat have significantly higher thermal conductivity when frozen compared to when unfrozen (Brown, 1963). This leads to a higher thermal connectivity between the atmosphere and the ground in winter compared to summer, and colder mean annual ground temperature in peatlands compared to surrounding areas. The ranges of tree and shrub species (primarily in the genera *Betula, Salix* and *Alnus*) in the Northern Hemisphere are expanding northwards with climate change (Myers-Smith et al., 2011), and these upright plants impact ground temperature in two contrasting ways (Way and Lapalme, 2021). The dominant effect occurs in winter, when snow accumulates on shrubs and reduces thermal connectivity with the cold atmosphere. In summer, the shadow cast by these plants effectively cools the ground surface.

Permafrost can be broadly classified according to the relative importance of climate and vegetation in its stability (Shur and Jorgenson, 2007). According to this classification system, continuous permafrost in colder climates is more climate-driven and less influenced by the vegetation above it, while discontinuous permafrost in warmer climates is more ecosystem-driven. Isolated patches of permafrost in climates with mean

annual air temperatures > 0 °C are classified as ecosystem-protected, meaning that they would not exist without the effects of the ecosystems above them.

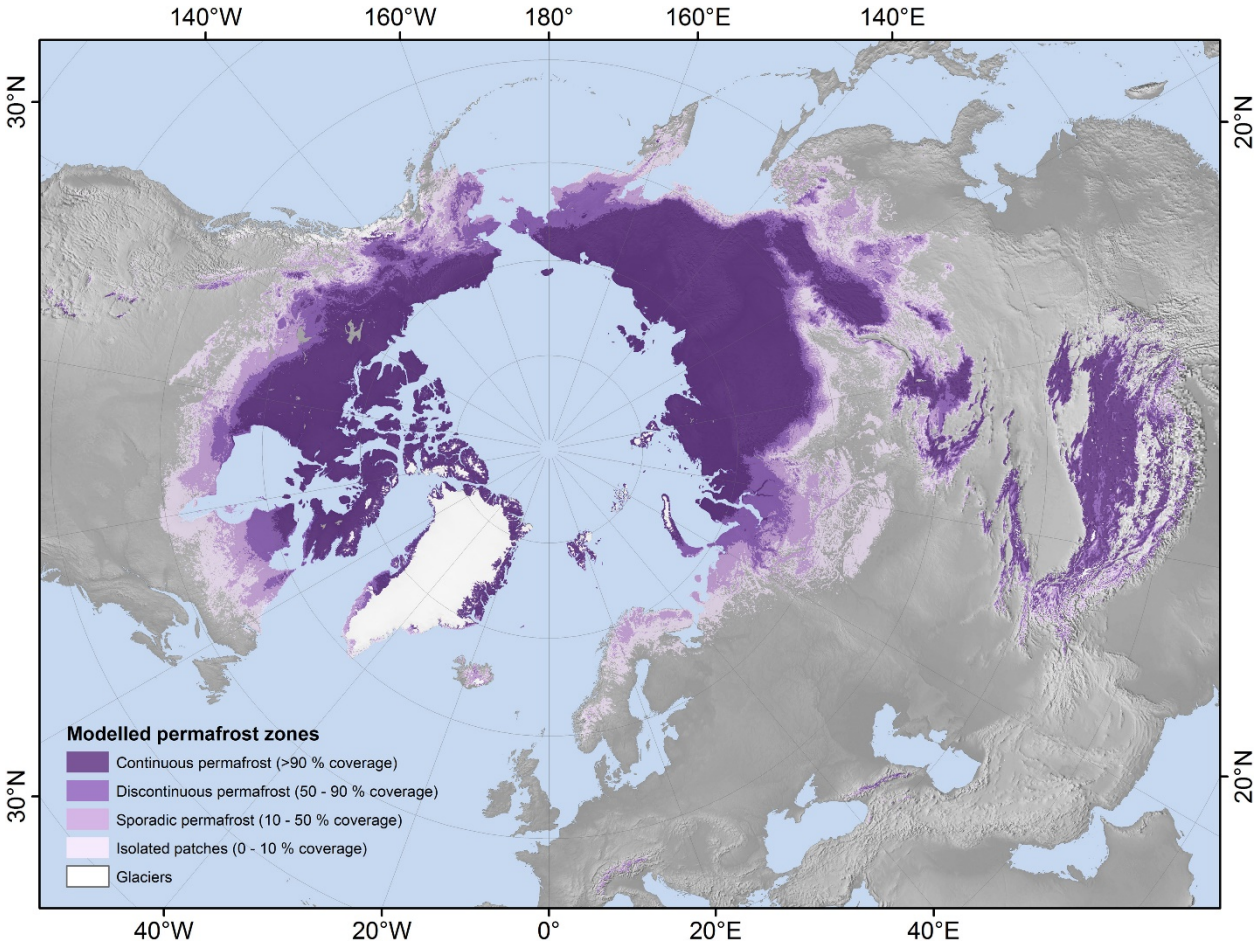

Figure 2.1. Map of permafrost zones in the Northern Hemisphere, from Obu et al. (2019).

While direct observation of permafrost with optical remote sensing is challenging since the physical characteristics (temperature, water/ice content) are not directly measureable, various optical and other remote sensing methods have been successfully applied to map permafrost, in part because periglacial landforms indicative of the presence of permafrost are recognizable and because vertical and horizontal movement due to frost action and thaw can be measured (Westermann et al., 2015). On the ground, geophysical methods such a ground-penetrating radar (Hinkel et al., 2001; Wu et al., 2005; Munroe et al., 2007) and electrical resistance tomography (Daily et al., 2004; Hilbich et al.,

2009; Lewkowicz et al., 2011) have been used to generate tomographic maps in order to monitor permafrost bodies. Unfortunately, these technologies have limitations: due to the size and weight of the equipment and the time involved in recording data, ground-penetrating radar and electrical resistance tomography are only suitable for small study areas. However, proxies for permafrost, such as land surface or near-surface temperature have been used to model ground temperature globally at a 1 km resolution (Bartsch et al., 2023).

Modelling permafrost presence in mountainous areas such as Yukon is challenging due to the heterogeneity of these landscapes (Etzelmüller et al., 2001; Etzelmüller, 2013). This is due to the more complex climates caused by mountains, the difficulties associated with working in mountains, and the issues associated with sloped area under-estimation. In order to account for the prevalence of inverted lapse rates below treeline in mountains and valleys, and the subsequently unique distributions of air temperature across these regions, equivalent elevation was developed (Lewkowicz and Bonnaventure, 2011). Equivalent elevation is a modified topographic surface which allows for a single average surface lapse rate to be applied to regions which otherwise exhibit distinct lapse rates above and below treeline. Using this and other topographic and climatic data, a permafrost presence probability model was created for southern and central Yukon capturing the effect of persistent inversions on mean annual air temperature (Bonnaventure et al., 2012). This model indicates that southern and central Yukon have an average permafrost probability of 58 % (see section 3.1). While permafrost probabilities are > 60 % in all of Yukon's mountains, lowland permafrost is latitudinally controlled.

2.2 Periglacial Landforms Indicative of Permafrost

Several types of landforms exist which can indicate permafrost presence, and can be broadly divided into variations of geometric shapes called patterned ground and different

types of frost mounds (Figure 2.2). Gelisols, cryosols, and histosols are terms for soils associated with permafrost identifiable by cryoturbation (Ahrens et al., 2004). So-called "drunken forests" are the result of trees, most often *Picea mariana*, being destabilized and tilted off-angle by cryoturbation (Zoltai, 1975). As soil and sediment are redistributed and sorted by cryoturbation they can be deposited in very distinctive shapes such as circles and groupings of circles called nets which can form on flat ground, or more elongated features called stripes which form on slopes (Hjort et al., 2010). Circles are generally less than 0.5 m high and from 0.5–3 m wide, while stripes are generally 0.3–1 m wide.

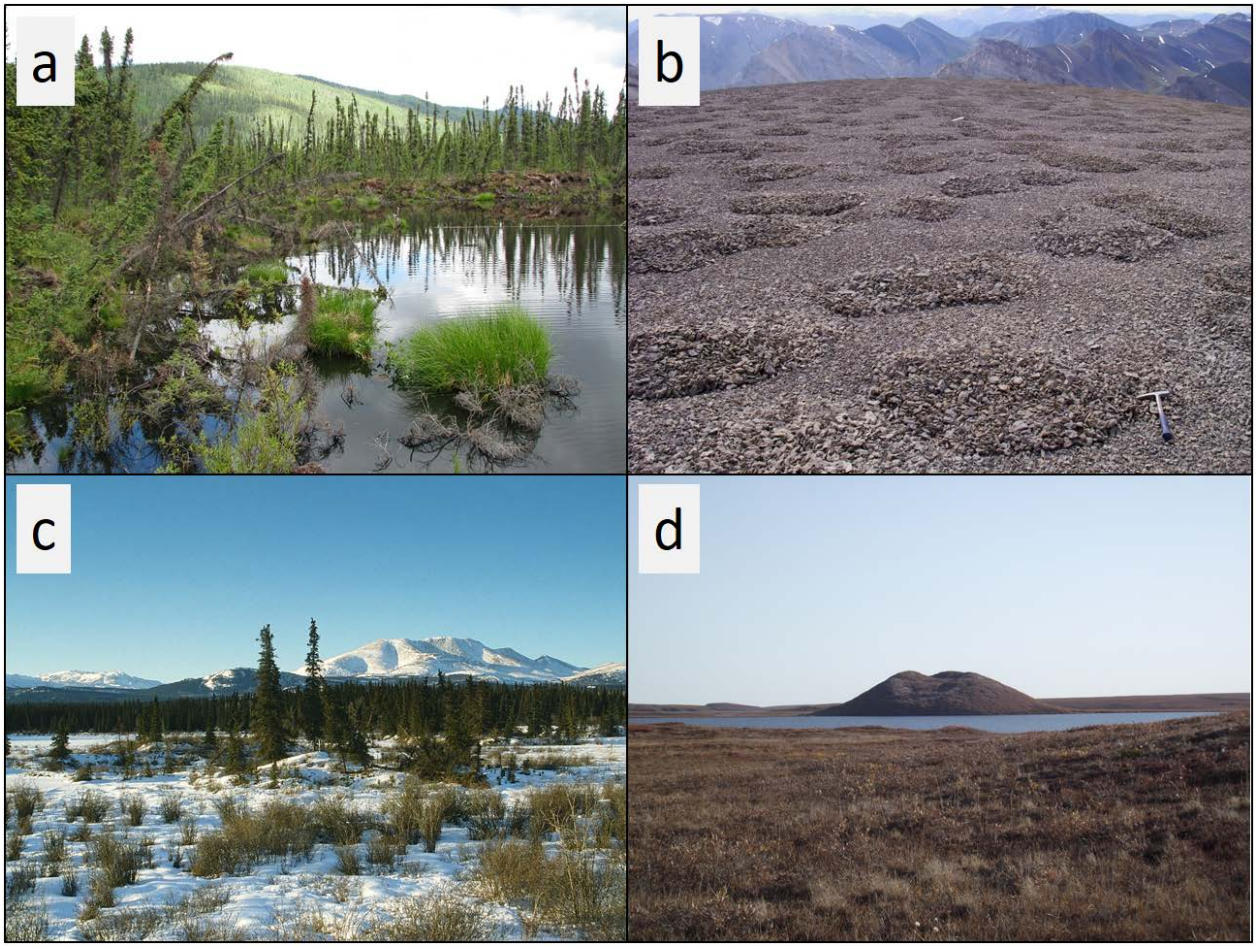

Figure 2.2. Periglacial landforms indicative of permafrost presence. (a) Drunken forest of *Picea mariana* surrounding a thaw lake in the Klondike Plateau, Yukon. (b) Circular formations of sorted limestone in the Mackenzie Mountains, Yukon. (c) Lithalsa near Fox Lake, Yukon. (d) Pingo near the Arctic coast in Tuktoyaktuk, Northwest Territories. (a), (b) and (c) from Huscroft et al. (2020), (d) from Hester Jiskoot.

Ice wedges form as ice aggrades over consecutive seasons in fissures left by the thermal contraction of ground (Péwé, 1963; Harry and Gozdzik, 1988; French and Shur, 2010) (Figure 2.3c). Three distinct types of ice wedges exist: epigenetic, syngenetic, and anti-syngenetic (Mackay, 1990). Epigenetic wedges are the most common in Canada (French, 2018) and form within existing permafrost on flat topography, pushing sediment up into ridges as they expand downwards. Syngenetic wedges form as permafrost develops in active floodplains and expand upwards as sediment accumulates on the surface, and anti-syngenetic wedges expand downwards on receding slopes. Ice wedges leave distinctively polygonal patterns on the ground surface in flat areas, resulting in a landscape called polygonal patterned ground (Washburn, 1956). These polygons are most often square or hexagonal, and form complexes upwards of 40 m wide. Polygonal patterned ground generally begins with the formation of low-centred polygons, with the ice wedges delimiting the polygons being taller than the ground around them. During periods of warming these transition into high-centred polygons as the ice in the wedges melts (MacKay, 2000).

Pingos are ice-cored hills found across the Arctic and Sub-Arctic, though generally not in great numbers (Gurney, 1998). They can be either open- or closed-system. Open-system pingos form when artesian pressure forces groundwater through taliks, which freezes once it is exposed to the atmosphere (O'Neill et al., 2020). As more water is pushed up, the mound can reach up to 60 m in height and up to 300 m in diameter (French, 2018). Closed-system pingos form in saturated sands and silts, often within alases, when permafrost aggrades after the drainage of a lake exposes the former lakebed to the cold atmosphere, and the pore water within the sediment beneath freezes. The former lakebed is then uplifted due to frost heave. The tops of pingos often have thinner snowpacks than surrounding areas due to a lack of vegetation and wind scouring, which leads to lower ground temperature due to reduced winter insulation.

Palsas, lithalsas and peat plateaus are other types of frost mounds which are common throughout northern Canada (Lundqvist, 1969; Zoltai and Tarnocai, 1975). They differ from pingos in that they are composed of segregated ice rather than intrusive ice (see Section 2.4.1). They form in peatlands, which normally have lower mean annual ground temperatures than surrounding areas because *Sphagnum* moss, a component of peat, has a higher thermal conductivity when it is frozen than when it is thawed (Seppälä, 1988). The smallest of these are hummocks, mounds up to 0.5 m high and 1.5 m wide evenly space about 1 m apart (Zoltai and Tarnocai, 1974). Palsas are mounds consisting of organic soil and segregated ice layers which form in areas with high amounts of organic matter, normally 1 to 7 m tall and less than 100 m in diameter (Zoltai and Tarnocai, 1975; Kershaw and Gill, 1979; Coultish and Lewkowicz, 2003; Seppälä, 2006). Lithalsas are a similar landform to palsas, except that they form in silty mineral soils due to the propensity for ice lenses to aggrade in those soils (Seppälä, 1988). Peat plateaus form in a similar way but are lower in prominence, normally being 1 m tall and up to several km^2 in extent (Zoltai and Tarnocai, 1975; Kershaw and Gill, 1979).

2.3 Permafrost Thaw

Air temperature in the Arctic is warming at a rate 1.9 times faster than the global average through a phenomenon called arctic amplification (Serreze and Barry, 2011; Ballinger et al., 2022). This has a clear impact on permafrost stability, since permafrost exists mainly in the areas which are experiencing the most rapid effects of climate change, and colder permafrost in Arctic tundra regions is warming faster than sub-Arctic taiga permafrost (Smith et al., 2022). The 2016 annual average temperature anomaly relative to the 1961–1990 normal in Yukon was been between 1.5 and 3.0 °C (Morice et al., 2021). Accordingly, permafrost in southern Yukon has warmed at a rate of < 0.1–0.3 °C per decade since the 1970s (Smith et al., 2022). Permafrost thaw is the result of ground temperatures coming out of equilibrium with surface temperatures (French, 2018).

Permafrost thaw manifests itself as a thickening of the active layer, the development and expansion of taliks, and eventually permafrost collapse. Talik development is a tipping point for permafrost stability, as advective thaw accelerates permafrost temperature increase (Connon et al., 2018; Devoie et al., 2019). This disruption of the thermal gradient between the surface and the atmosphere can occur for a number of reasons: changes in climate, hydrology, and surface features, such as vegetation and infrastructure, can all affect the ground thermal regime in an area. As such, permafrost thaw can result directly from human activities such as the construction of transport and hydrological infrastructure and buildings, deforestation and land clearance, and through anthropogenic climate change (Raynolds et al., 2014; French, 2018).

While climate-driven permafrost is more vulnerable to climate change than to landscape disturbance, ecosystem-driven and ecosystem-protected permafrost are more vulnerable to landscape disturbance due to fire or human activity than to climate change (Yoshikawa et al., 2002; Shur and Jorgenson, 2007; Jafarov et al., 2013; Gibson et al., 2018). Though peatlands can protect permafrost from thaw, climate warming is predicted to bring many permafrost peatlands beyond the climatic thresholds of permafrost stability within the 21st century (Fewster et al., 2022; Könönen et al., 2022). Human activity can affect plant communities in negative ways and has been observed to instigate or exacerbate permafrost thaw (Greller et al., 1974; Raynolds et al., 2014). Vegetation communities in permafrost peatlands shift from mosses and lichens to woody shrubs in response to increased air temperature and a lower water table (Chasmer and Hopkinson, 2017; Carpino et al., 2021; Fewster et al., 2023). Another example of permafrost-ecosystem dynamics in response to a warming climate is shrubification in the Torngat Mountains, which has caused active layer thickening and permafrost temperatures to warm due to increased snow accumulation in the shrubs (Lewkowicz et al., 2017).

Globally, permafrost is following a warming trend and is degrading at high rates (Biskaborn et al., 2019). An estimated 1400 km^2 of permafrost has thawed each year in the Northern Hemisphere since 1969 (Li et al., 2022b). There are many reasons why permafrost thaw is important to people around the globe, some more publicized than others (Bowden, 2010). The resurrection of prehistoric viruses (Legendre et al., 2015) and the thaw of Spanish flu victims (Davis et al., 2000) are two lesser known pathogenic threats of permafrost thaw. However, the most important aspects of permafrost degradation are the associated landscape degradation processes and the positive feedback loop between climate warming and permafrost thaw. During thaw, the organic carbon sequestered in permafrost soils begins to decompose and releases the greenhouse gases methane and carbon dioxide into the atmosphere (Grosse et al., 2011; Schuur et al., 2015), further accelerating climate change. This further warming climate leads to more thaw and lengthening of the fire season, which exacerbates thaw in ecosystem-protected permafrost (Woo et al., 1992).

2.4 Ground Ice and Associated Landforms

Ground ice is frozen water which exists within permafrost (Mackay, 1972). Unfrozen water also exists in permafrost and migrates through soil and sediment matrices due to gravity, hydrostatic pressure, thermodynamic disequilibrium and vapor flux (Burt and Williams, 1976; Williams and Smith, 1989; Fu et al., 2022). An understanding of ground ice is essential to this thesis research because its abundance is the principal variable which determines the geomorphological and biological outcomes of permafrost thaw (French, 2018; Devoie et al., 2024). This is due to the combination of the difference in volume between liquid water and ice, and the loss of cohesion in earth materials and subsequent softening of the ground. To illustrate: a frozen, dry lump of soil will likely not change form if it thaws, however, if a similar volume of soil is saturated when it freezes, it will become a puddle of mud when it thaws. Since water expands by 9 % when it freezes,

ground ice can affect the topography above it when it forms. The uplifting of the ground surface due to this expansion is called frost heave (Taber, 1929), and is the process through which frost mounds form, while frost cracking causes ice wedge patterns (Kachurin, 1964).

The ice content of a permafrost body can be measured as a percentage of soil volume or as a ratio of ice mass to dry soil mass. High ice content is generally classified as > 20 % ice content by volume (e.g. Heginbottom et al., 1993), though some organic soils have been observed with ice contents of around 2000 % dry mass (Washburn, 1980). As seasonal ice melts in the active layer during the summer and percolates downwards it accumulates at the permafrost table, leading to most ground ice occurring within the top 1–3 m of permafrost (Kokelj and Burn, 2005; French, 2018). However, ice content can vary greatly over small areas and depths (Fan et al., 2021).

2.4.1 Ground Ice Types

Ground ice can exist in many forms and aggrades through different processes. The resulting shape and distribution of ice within permafrost is called cryostructure (Murton and French, 1994), some examples of which are shown in Figure 2.3. There is such a variety of cryostructures that there has yet to be a consensus on their classification (Murton and French, 1994; Shur and Jorgenson, 1998; French and Shur, 2010; O'Neill et al., 2019). The most common cryostructures are sill ice, pingo ice, ice wedges, reticulate ice and ice lenses. Other less common cryostructures include ataxitic or suspended ice, in which rock fragments are suspended within a massive body of ice, and crustal ice, in which an ice crust forms around individual rocks within sediments (French and Shur, 2010). French (2018) describes four main types of ground ice, based on the process of their formation. In order of prevalence in Yukon, these are pore ice, vein ice, segregated ice and intrusive ice. Relict ice is ancient ice which has been buried by sediments (French, 2018).

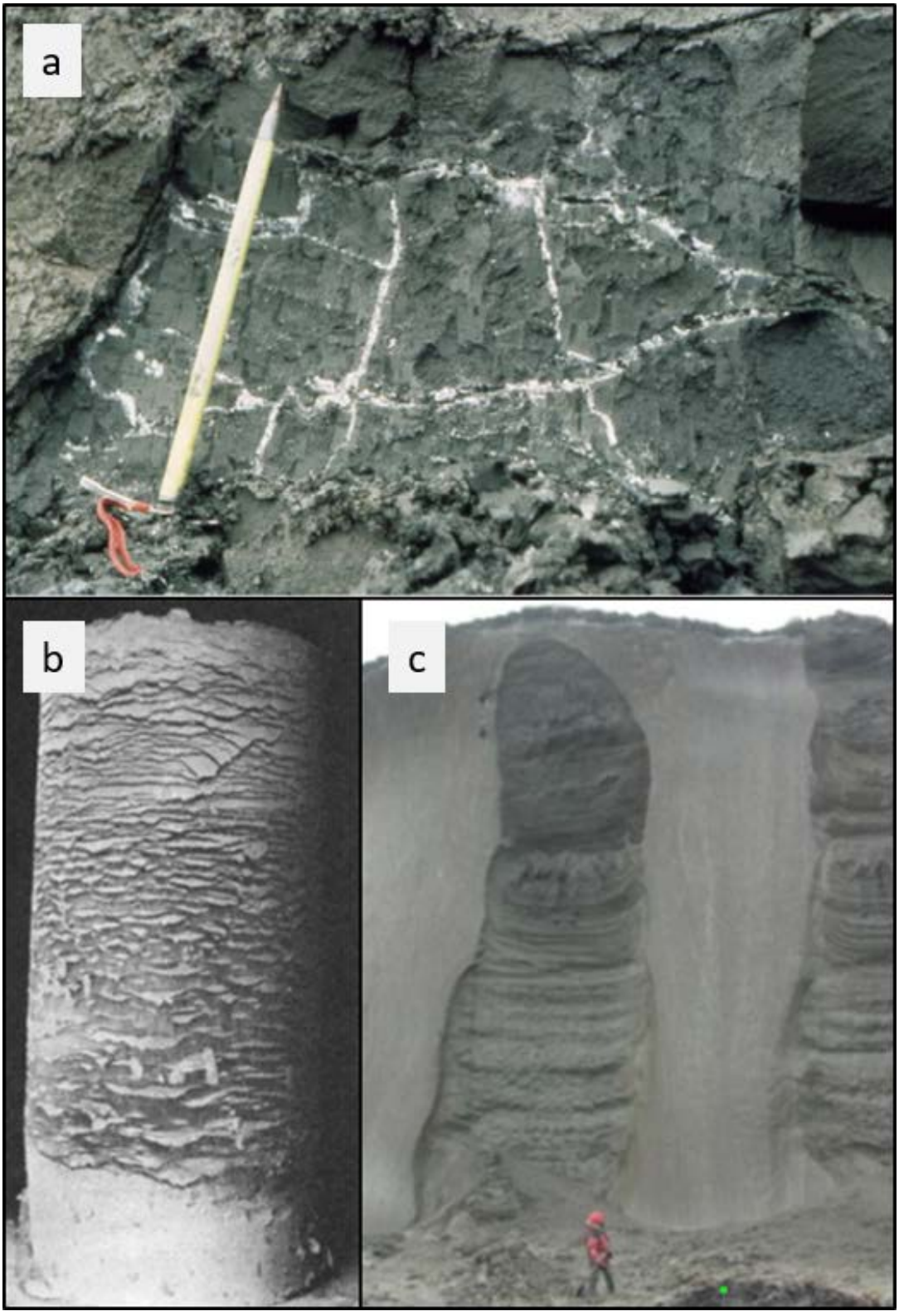

Figure 2.3. Three ground ice cryostructures: (a) Reticulated ice in silty clay from French (2018), (b) clay cylinder exhibiting excessive ice lens segregation in a lab setting from Taber (1929), and (c) syngenetic ice wedges in yedoma silt on a Siberian island with person for scale from Schirrmeister et al. (2013).

Pore ice, also called interstitial ice or cement ice, is found in all types of frozen ground that contain some amount of moisture, and is therefore the most common type of ground ice (Vtyurin, 1989; French, 2018). It forms sand-sized ice crystals in the pores between soil particles, and its presence is indicative of unsaturated permafrost (< 10 % volume). Pore ice provides some integrity and rigidity to the soil matrix, acting as a cement (French, 2018). Due to its small volume and relatively even distribution within soil, pore ice is the least significant type of ground ice when considering the consequences of thaw (French, 2018). Pore ice is most prevalent in low-humidity environments at freezing temperatures close to 0 °C (Huang and Aughenbaugh, 1987).

Vein ice forms when water accumulates and freezes in cracks on the ground surface. Frost cracking occurs when surficial materials contract as they cool. When this happens on the ground surface ice wedges develop, and when it occurs within permafrost soils and sediments a 3D matrix of ice veins develops, forming a cryostructure called reticulated ice (Figure 2.3a) (Mackay, 1974). Reticulated ice predominantly forms in frost-susceptible sediments such as silts and clays (Mackay, 1974).

Segregated ice refers to ice that has migrated through a body of frozen ground and has accumulated in lenses or layers (Figure 2.3b) (Mackay, 1972; French, 2018). Ice lenses are lenticular in shape, up to several metres in thickness (French, 2018), and form perpendicular to the temperature gradient (Watanabe, 2002). Thus, they are generally in a horizontal orientation in near-surface permafrost (Hallet, 1990). Ice segregation occurs due to cryosuction, a process in which liquid water in frozen soils follows a gradient of Gibbs free energy towards ice (Loch, 1978; Williams and Smith, 1989). Gibbs free energy is the thermodynamic potential energy associated with changes in state of matter (Hillig, 1997) (e.g. the phase change between liquid water and ice requiring 334 kJ/kg, meaning that ice has less Gibbs free energy than liquid water). Unfrozen water capacity has been shown to increase with decreasing soil particle size, with sands having next to no

unfrozen water and silt to clay-type soils having up to 50 % unfrozen water depending on temperature (Burt and Williams, 1976; Williams and Smith, 1989). Fine-textured soils and sediments are termed 'frost susceptible' for this reason. Since cryosuction depends on liquid water availability, ice lenses form predominantly in fine-grained soils where there is a source of liquid water. A large body of research on the formation of ice lenses exists in the fields of materials engineering and crystallography (e.g. Hillig, 1997; Watanabe, 2002). This research is often based on experiments involving the directional freezing of saturated synthetic sediments, commonly glass beads, in settings which allow for careful observation of ice lens growth. This research builds on the foundational report by Taber (1929) which asserted that ice crystal growth was responsible for the phenomenon of frost heaving, and that soil particle size, water availability, and cooling rate were the variables controlling lens formation. Soil particle size is inversely related to the specific surface area of a soil (the combined surface area of all particles in a soil sample) and is the most important variable (Rieke et al., 1982). These experiments confirmed the field observations that ice lenses preferentially form in fine-grained sediments (Burt and Williams, 1976), though ice segregation has been observed in all sediment sizes and has even been identified as the mechanism causing bedrock fracture that results in felsenmeer landscapes (Murton et al., 2006). One type of sediment especially known for its frost susceptibility and for containing massive quantities of ground ice is yedoma, a Pleistocene-aged silt and clay sediment, often loess, found in Siberia, Alaska, and Yukon (Schirrmeister et al., 2013; Strauss et al., 2014; Fortier et al., 2018). Other soil properties such as solute content also affect the unfrozen water content of soils (Banin and Anderson, 1974).

Intrusive or injection ice forms when water is forced into confined spaces within permafrost by artesian pressure where it freezes (French, 2018). It is this type of ice which forms the core of pingos when artesian pressure forces groundwater through taliks. Ice

sills and dykes form when water is forced into permafrost bedrock, sometimes causing bedrock fracturing (Murton et al., 2006). Ice sills form between horizontal bedrock strata, while dykes are vertical planar masses which form in sediments.

Relict ice is a type of ground ice that is buried ancient glacial ice, preserved over long-term changes in climate, sometimes through multiple glacial and interglacial periods (French, 2018). Due to this, relict ice is restricted in distribution to past glacial limits and areas that are prone to avalanches, such as at the base of steep slopes. New ice can aggrade onto relict ice as ground- or meltwater moves through permafrost (O'Neill et al., 2019). Relict ice is similar in appearance to segregated ice, as it is often found in thick horizontal bands.

2.4.2 Ground Ice Mapping

Despite the importance of ground ice to permafrost thaw outcomes, knowledge of its distribution is still limited compared to knowledge of permafrost distribution (De Pascale et al., 2008; Couture and Pollard, 2017; Zwieback and Meyer, 2021). The Circumarctic Map of Permafrost and Ground Ice Conditions (the IPA map) was developed in 1993 by the International Permafrost Association (Heginbottom et al., 1993). The IPA map shows permafrost extent and ground ice abundance at a scale of 1:10 000 000 and uses a ground ice abundance classification by percent volume as high (> 20), medium (10–20) and low (< 10) for the upper 10–20 m of overburden, with known distribution of ice wedges, massive ice and pingo ice appended to these classes. The IPA map indicates that there are between 10.80 and 35.46 x 10^3 km^3 of ground ice in Canada's permafrost, with the majority being in the continuous permafrost zone (Zhang et al., 2000). All data in the IPA map came from previous national, regional and local mapping efforts.

Since the publication of the IPA map, knowledge of ground ice distribution has evolved through three approaches: models, geophysical observations and remote-sensing

techniques. All three of these methods have inherent problems. The models depend upon the quality of input data and result in coarse outputs which are often not applicable to regional projects. The geophysical observation methods are not practical to apply to large areas, and most of the remote sensing techniques are relatively new and can only detect specific cryostructures or the effects of melting ground ice.

Various models have been employed to map ground ice distribution across national or circum-Arctic scales. The ground ice map of Canada shows the modelled distribution of relict, segregated and wedge ice across Canada at a 1:5 000 000 scale using a paleogeographic method which incorporates paleoclimate data, glacial extents, permafrost distribution (from the IPA map) and surficial geology data (Figure 2.4) (O'Neill et al., 2022). This map indicates that ground ice occurs in very high abundance (> 30 % excess ice volume in top 5 m of permafrost), high abundance (> 20–30 %), medium abundance (> 10–20 %), and low abundance (> 5–10 %) in 2, 5, 21 and 26 % of Canada's permafrost regions respectively. The western Arctic has the highest abundance of ground ice, especially Banks Island, Victoria Island and coastal NWT. This is most likely due to thick frost susceptible overburdens and relict ice from the Laurentide Ice Sheet.

At the circum-Arctic scale, the SOC-ICE model uses biogeochemical, hydrological, and climatological input data from the past 125 000 years to estimate soil organic content and ground ice content (Saito et al., 2021). While the SOC-ICE model's main purpose was to model relative distribution of ground ice for inclusion in a permafrost vulnerability model, it is in general agreement with the ground ice map of Canada, except in bedrock areas.

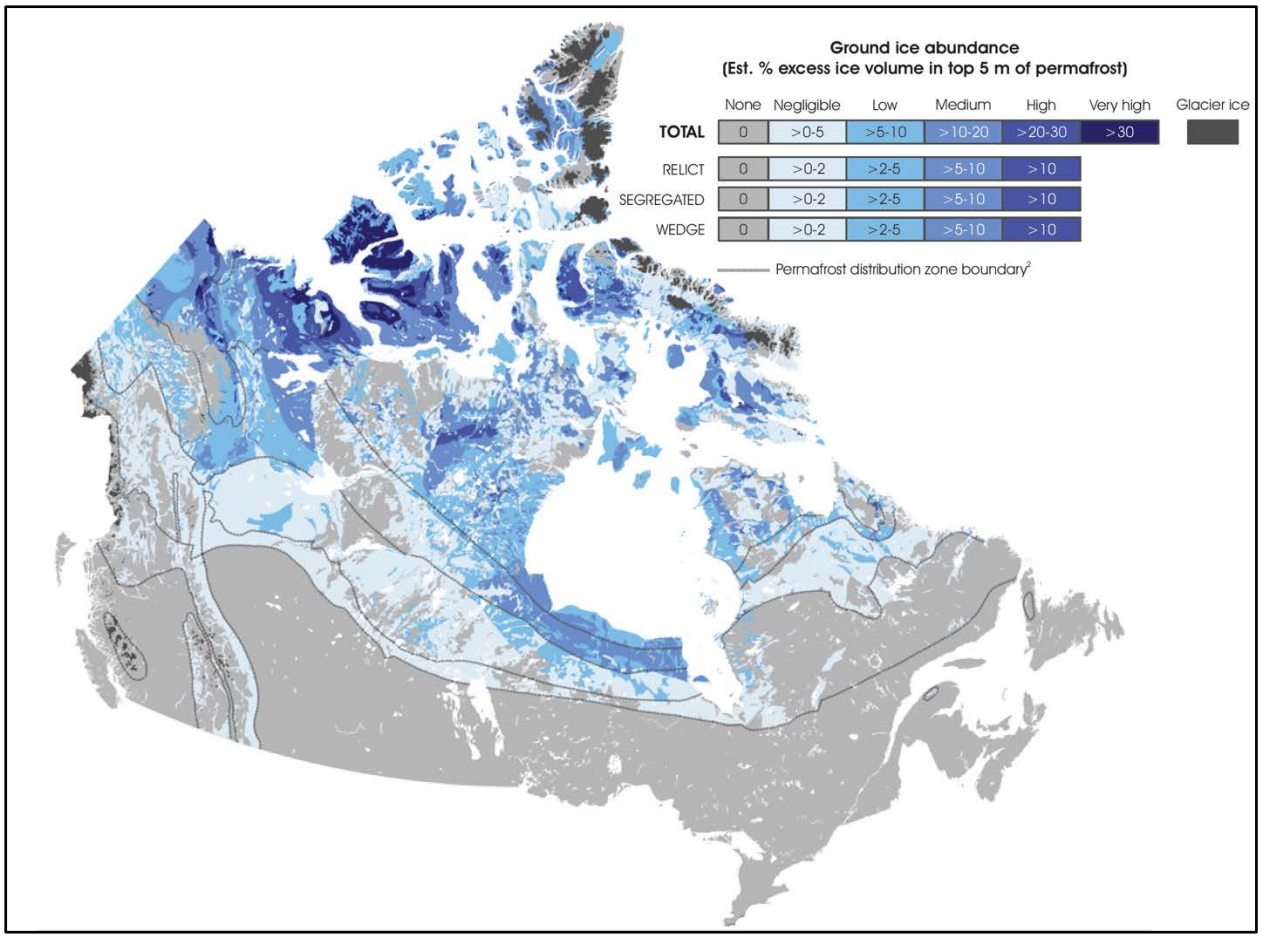

Figure 2.4. Ground Ice Map of Canada showing classified ground ice abundance by excess ice volume in the top 5 m of permafrost, from O'Neill et al. (2022). Gray lines are permafrost distribution zones from Heginbottom et al. (1995).

Three geophysical monitoring techniques are commonly used in detailed permafrost mapping: electrical resistivity tomography, capacitively coupled resistivity and ground-penetrating radar (Van Dam, 2012). These permafrost mapping techniques are rarely applied to ground ice distribution (Kneisel et al., 2008), however some examples exist of these techniques being used to create highly detailed ground ice distribution maps for small areas (< 10 km^2), showing features such as ice wedges and lenses (e.g. De Pascale et al., 2008; Lewkowicz et al., 2011; Herring and Lewkowicz, 2022). Optical remote sensing of ground ice is challenging because, except in the case of ice wedge polygons, it is buried under the active layer. Ice wedge polygons have been mapped in some areas of Yukon

using elevation models and drone imagery, which has allowed for the inference of permafrost ice content in those areas (Frappier and Lacelle, 2021), and pingos have been mapped in Alaska and Yukon using airborne surveys (Hughes, 1969). Lidar has been used to map ice wedge polygon distribution in Alaska and Svalbard (Lousada et al., 2018; Abolt and Young, 2020). Lidar, aerial photography and satellite remote sensing have also been used to measure ground surface subsidence as an indicator of permafrost and ground ice presence in areas of about 50 to 150 km^2 in Alaska and Canada (Chasmer et al., 2010; Chasmer and Hopkinson, 2017; Zwieback and Meyer, 2021).

2.5 Thermokarst Landforms

Thermokarst processes result in ground subsidence and destabilization and the formation of distinct landforms through the collapse of existing periglacial landforms (Figure 2.5). There are up to 23 unique thermokarst landform types listed by Jorgenson (2013): deep thermokarst lakes, shallow thermokarst lakes, glacial thermokarst lakes, glacial thermokarst, thermokarst basins, thermokarst-lake basins, thaw sinks, thermokarst fens, thermokarst bogs, thermokarst shore fens, thaw slumps, detachment slides, collapsed pingos, beaded streams, thermal erosion gullies, thermokarst water tracks, collapse-block shore, ice-block landslide, thermokarst troughs and pits, thermokarst pits, conical thermokarst mounds, irregular thermokarst mounds and sink holes. Of course, this type of exhaustive framework is too complex for the purposes of susceptibility modelling. There are three broad categories of thermokarst landform: lakes, wetlands and hillslope failures (Kokelj and Jorgenson, 2013). Within those categories, the most common types of thermokarst are thaw lakes, thermokarst bogs and fens, active layer detachments and retrogressive thaw slumps. Pingo degradation and collapse often involves a suite of thermokarst processes (Babiński, 1982; Matthews et al., 1997; Mackay and Burn, 2011). The type of landform that results from permafrost thaw depends primarily on ground ice

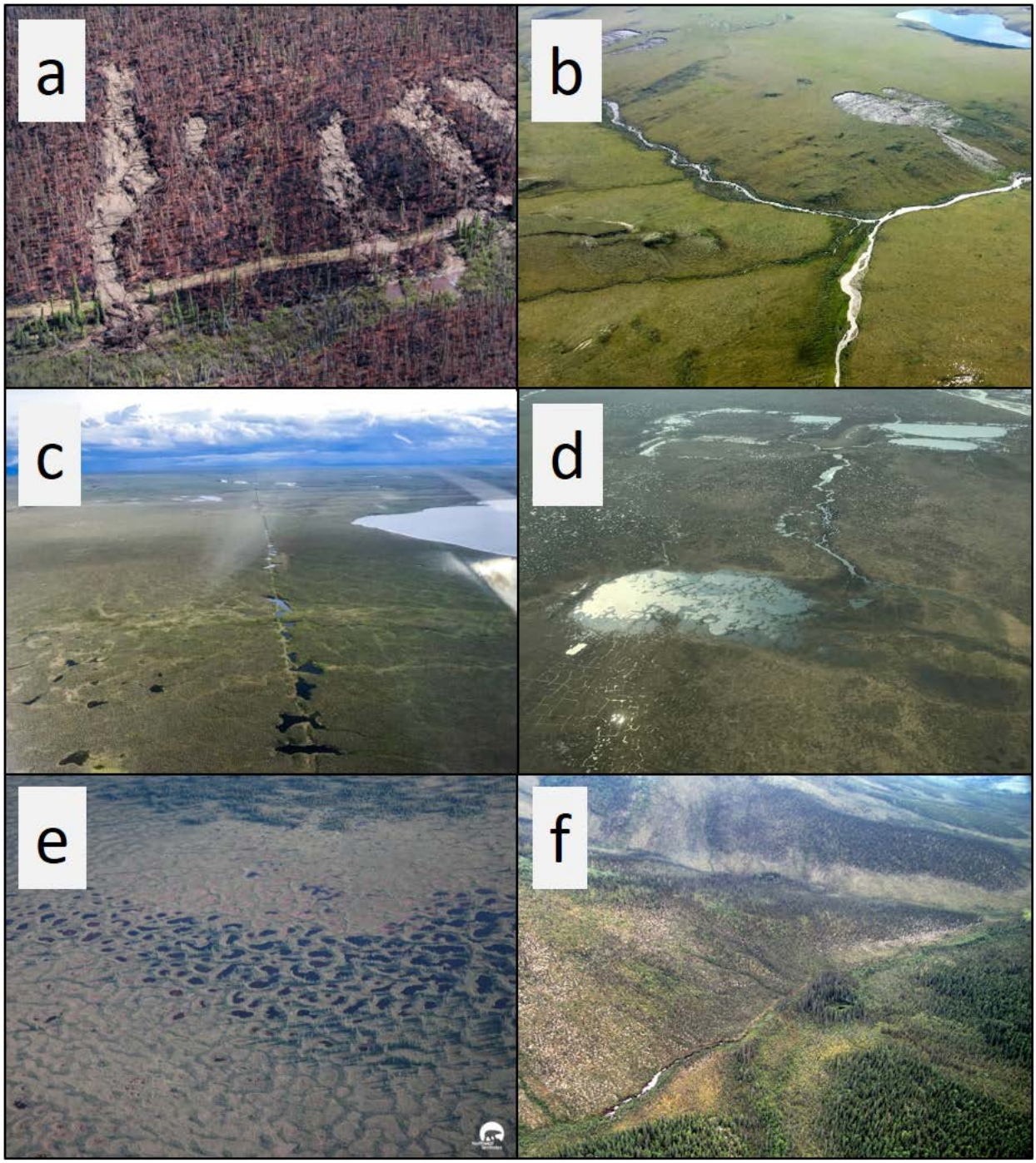

Figure 2.5. Various thermokarst landforms and their effects on surrounding environment and infrastructure. (a) Widespread active layer detachment slides in Steele Creek, Yukon after an intense wildfire. (b) Multiple retrogressive thaw slumps in the Noatak valley, Alaska. (c) Thermokarst thaw ponds developing along a 50-year old seismic line in northern Alaska. (d) Partially drained thermokarst lake, with high- and low-centred ice wedge polygons visible. (e) Fen and accompanying thermokarst ponds near Hay River, Northwest Territories. (f) Collapsed pingo with a thaw lake in its centre in the Klondike Plateau, Yukon. (a), (b) and (f) from Huscroft et al. (2020), (c) and (d) from Nolan (2018), and (e) from Northwest Territories Geological Survey (2019).

content, the steepness of slopes in the surrounding area and the surficial material forming the active layer.

2.5.1 Thaw Lakes

Thaw lakes are widespread in arctic and subarctic lowland areas with low topographic relief, especially in tundra regions (French, 2018). Most lakes are smaller than 300 m in diameter, though large lakes can exceed 2 km in diameter (French, 2018). Not all lakes in permafrost regions are a result of thermokarst processes, and their development is not entirely understood, but, in general, they result from ground ice melt and ground subsidence (Jorgenson and Shur, 2007). Beneath tree line, the presence of standing dead trees within a lake, or of a drunken forest along the shoreline are indicators that a lake formed due to thermokarst processes (Kokelj and Jorgenson, 2013; Roy-Léveillée and Burn, 2017).

Thaw lake development starts with the growth of small ponds, also called thermokarst troughs and pits, in degrading permafrost (Jorgenson et al., 2008). Shallow thermokarst lakes often develop in the place of collapsing palsas and lithalsas (Matthews et al., 1997). Taliks form beneath these ponds as massive ground ice in the form of wedges or lenses begins to melt. This progresses to the formation of a depression and the accumulation of surface water during spring and summer. The presence of standing water changes the ground thermal regime in a number of ways. Most importantly, water has a low albedo (for most incidence angles), the ability to absorb light through depth, a high heat storage capacity and high thermal conduction (Kokelj and Jorgenson, 2013). All of these effects serve to increase the rate of thaw under the lake, leading to lake expansion at an average rate of 15 to 25 cm/yr (French, 2018). In addition, lake depth has an impact on thermal regime, as lakes shallower than 2 m generally freeze to depth during the winter (Jorgenson et al., 2008; Kokelj and Jorgenson, 2013). Hence, deep thaw lakes almost always have taliks beneath them, while shallow thaw lakes can be underlain by

permafrost in climates with mean annual air temperature ≤-6 °C (Jorgenson et al., 2008). Thaw lakes can develop into flat-bottomed grassy basins called alases, from the Sakha word *alaas,* through decades or centuries of desiccation, or through rapid drainage due to gully and stream development (Soloviev, 1962; Morgenstern et al., 2013; Crate, 2022). Permafrost often begins to aggrade once the old lakebed in an alas is exposed to the atmosphere, and ice wedge polygons and closed-system pingos are commonly found at the bottom of alases (Jorgenson and Shur, 2007).

Oriented lakes are elongated and share a common orientation, and are a ubiquitous feature in Arctic coastal lowlands (Black and Barksdale, 1949). They are also present in the Qinghai-Tibet Plateau (Niu et al., 2015). It is theorized that their orientation is a result of wave action caused by prevailing winds, with the long axis of the lakes being normal to the prevailing wind, and varying by less than 5° (Côté and Burn, 2002; Morgenstern et al., 2008). Since these lakes have also been observed in permafrost areas with little ground ice, not all oriented lakes are necessarily thaw lakes (Wolfe et al., 2020). Oriented lakes occur in lowland tundra and are rarely found outside of these areas. Therefore, it is unlikely that any oriented lakes would be found in the mountainous areas in Yukon south of the Mackenzie Mountains.

The percentage areal coverage of lakes within a region, called limnicity, can vary greatly in permafrost landscapes: for example, the Old Crow Basin in northern Yukon contains > 2500 lakes in a 5600 km^2 area with a limnicity of 35 % (Roy-Léveillée and Burn, 2017), while in the smaller area of Old Crow Flats limnicity is only 6 % (Labrecque et al., 2009). Studies in Alaska and Siberia showed a range in limnicity between 0.8 and 20 %. Alases covered between 26 and 33 % of those study regions, which, combined with those areas' limnicity means that up to 50 % of the landscape could be susceptible to lake development in the future (Frohn et al., 2005; Hinkel et al., 2005; Grosse et al., 2008;

Farquharson et al., 2016). Limnicity is highest in areas with more yedoma sediment (Veremeeva and Glushkova, 2016).

While climate warming will result in an increase in thaw lakes, trends in their current distribution in the Northern Hemisphere are mixed: the discontinuous permafrost zone has experienced a decrease in lake area, while the continuous permafrost zone has not exhibited a marked change in lake area (Webb and Liljedahl, 2023). Thaw lakes emit methane as decomposing organic matter in the lake bed is released through ebullition (Walter et al., 2006). However, lake drainage reduces the amount of methane emission as an aerobic environment develops and permafrost aggrades (van Huissteden et al., 2011). Currently, thaw lake development and drainage cycles are predicted to act as a carbon sink as permafrost aggrades in alases, while in a warmer climate permafrost will not aggrade as readily in newly-drained lakes (Jones et al., 2022).

2.5.2 Hillslope Thermokarst

When thermokarst processes occur on steep slopes, such as riverbanks, hillsides or coastlines, they can instigate a variety of forms of mass movement. Hillslope thermokarst is generally the most rapidly developing type of thermokarst and can have the most immediate impacts on landscapes and ecosystems. Hillslope thermokarst is a natural hazard with the potential to cause catastrophic loss of life and damage to infrastructure (Harris, 2005). The distribution of this type of thermokarst is dependent on slope, vegetation, bedrock and surficial geology and glacial history (Balser et al., 2009). There are four types of hillslope thermokarst landforms: (1) active layer detachments, (2) retrogressive thaw slumps, (3) thermo-erosion gullies and (4) collapse blocks (Jorgenson et al., 2008; Kokelj and Jorgenson, 2013).

Active layer detachments are a type of landslide in which surficial material slides or flows over the top of permafrost (Harris and Lewkowicz, 1993; French, 2018). They

occur when the active layer detaches from the top of permafrost in response to saturation of the active layer. This excess water can come from heavy precipitation events (Kokelj et al., 2015b), snowmelt or rapid melt of ice lenses at the top of permafrost in response to prolonged above-freezing air temperatures (Lewkowicz, 2007; Lamoureux and Lafrenière, 2009; Lewkowicz and Way, 2019). Additionally, these landforms have been observed to increase in frequency in response to fire-induced permafrost thaw (Lewkowicz and Harris, 2005; Lipovsky et al., 2005; Holloway et al., 2020; Young et al., 2022). Active layer detachments are typically between 10 to 20 m wide and 20 to 40 m long, but can be up to 600 m in length (Harris and Lewkowicz, 1993), and they often occur in clusters. The scars left by these mass wasting events are usually recolonized by plant communities after 50 years (Cannone et al., 2010).

Retrogressive thaw slumps occur when a slope is destabilized by erosion or ground subsidence, exposing ice-rich sediments to the air. The ablation of ground ice in these sediments leads to further erosion and the development of a headwall that retreats upslope over the course of years, exposing new frozen ground material to further ablation (Burn and Lewkowicz, 1990). Retrogressive thaw slumps have been observed to occur on upland plateaus and along lakeshores, riverbanks and coastal cliffs (Lantuit and Pollard, 2008; Kokelj et al., 2009; Lacelle et al., 2010). Headwall retreat rates in retrogressive thaw slumps depend upon ground ice content, slope morphometry and weather (Kokelj and Jorgenson, 2013; Balser et al., 2014). Retrogressive thaw slumps in the Mackenzie Delta region had average headwall retreat rates of 0.5 m/year (Lantz and Kokelj, 2008), while in slumps in the Noatak Valley of Alaska these rates were 38 m/year (Swanson and Nolan, 2018). A flat floor forms beneath the headwall, where meltwater, sediment and plant debris accumulate as a fine sediment (mud). Subsequently, mudslides transport material from the floor through evacuation channels. Stratigraphic and plant community evidence suggest that retrogressive thaw slumps are polycyclic, and go through cycles of initiation,

stabilization and re-initiation, typically over the course of less than 100 years (Kokelj et al., 2009; Lacelle et al., 2010). This type of thermokarst can rapidly alter water quality in lakes and streams by increasing turbidity and solute content (Bowden et al., 2008; Mesquita et al., 2008), and by damming streams (Malone et al., 2013; St. Pierre et al., 2018). The effects of thermokarst mass wasting in headwater regions can be seen in waterbodies hundreds of kilometers downstream (Kokelj et al., 2021).

Thermal erosion gullies are 1 to 5 m deep incisions that form in ice wedge polygon networks when surface water alters the ground thermal regime, inducing thaw (Fortier et al., 2007). These features can grow over multiple seasons due to the positive feedbacks caused by the erosion of subterranean tunnels, advective heat transfer and increased snow accumulation (Godin and Fortier, 2012). They can occur anywhere that ice wedge polygons are present, and have been observed on Herschel Island in Yukon (Lantuit and Pollard, 2008).

Between 30 and 34 % of the world's coast is affected by permafrost (Lantuit et al., 2013). Increased air and water temperature and sea level rise exacerbate the erosion of these coastlines as permafrost thaws (Jones et al., 2018). As wave action undercuts a cliff face, large blocks up to 25 m wide break off and fall into the sea (Hoque and Pollard, 2016). This process can instigate other thermokarst processes such as thaw lake drainage and retrogressive thaw slumps. Permafrost coastal erosion is a recognized hazard across the coasts of arctic Alaska and Canada, especially in the Canadian Arctic islands (Hoque and Pollard, 2016; Fritz et al., 2017; Berry et al., 2021). The failure point in these events is most often at ice wedges.

2.5.3 Wetland Thermokarst

Thermokarst bogs and fens form in response to permafrost degradation in low-lying peatlands where water accumulates. Apart from chemical and ecological differences, bogs generally have no water flow, while fens experience slow drainage through seepage and are a part of a larger hydrological system (Zoltai and Vitt, 1995; Warner et al., 1997). As described in Section 2.1, peatlands have lower ground temperatures than adjacent areas due to the thermodynamic properties of peat (Seppälä, 1988). The typically high ice content of peatlands raises the risk of ground subsidence, or thaw settlement, when permafrost degrades. The pits and troughs formed by degrading ice wedge polygons often develop into thermokarst wetlands as thaw progresses (Steedman et al., 2017). This has been observed to greatly affect linear infrastructure such as roads and pipelines that travel though these areas (Smith et al., 2008). Degrading peat plateaus go through a cycle of desiccation, cracking and increased thaw and inundation, followed by the development of stable non-permafrost wetlands (Swindles et al., 2015; Chasmer and Hopkinson, 2017). Wildfire contributes to thermokarst wetland growth by increasing active layer thickness and the size of taliks (Gibson et al., 2018). While degrading peatlands are a source of methane, wetlands established after permafrost collapse have the potential for carbon sequestration (Swindles et al., 2015). The growth of thermokarst wetlands often leads to the fragmentation of forests and the loss of boreal habitats (Baltzer et al., 2014; Lara et al., 2016).

Beaded streams are ubiquitous landforms of wetland thermokarst and are a type of stream system interspersed with small pools that are often situated above taliks (Arp et al., 2015). These pools are typically ~ 60 m^2 in size, and form along ice wedge polygons. They can be many thousands of years old, making them a good indicator of climate change (Arp et al., 2015). About one third of all Arctic catchments contain beaded streams, and they are most prevalent in continuous permafrost (Harlan et al., 2023).

2.5.4 Pingo Degradation

Thermokarst processes are common in pingos (Liestøl, 1996), which can respond to permafrost thaw in a number of ways. Dilation cracking in the overburden material commonly occurs on the summit or along the periphery of the pingo mound during its growth (Mackay, 1998; Mackay and Burn, 2011). While epigenetic ice wedges can form in these dilation cracks in cold climates, thaw occurs if the climate is not conducive to permafrost aggradation (Babiński, 1982; Mackay, 1998). This process is exaggerated on the southern aspect of pingos in the Northern Hemisphere due to the increased effect of solar radiation on the ground thermal regime (Babiński, 1982; Mackay and Burn, 2011). Similar to the degradation of ice wedge polygons, water can accumulate in these cracks and can then initiate further thermal erosion of the pingo. Eventually, the pingo's ice core will completely melt, often leaving a thaw lake in the centre of the collapsed pingo surrounded by distinctive ramparts (French, 2018). The resulting landform can be called a dead pingo or a pingo scar and can occur in clusters (Flemal, 1976).

Open- and closed-system pingos undergo distinct forms of degradation due to the difference in water availability. In open-system pingos, groundwater can escape under artesian pressure once permafrost and ground ice have sufficiently degraded in response to climate warming (Babiński, 1982; Mackay, 1998). The flow of water from these springs can further erode the pingo through abrasion and thermal erosion. Similarly, wave action can rapidly degrade pingos adjacent to lakes and coasts (e.g. Tuktoyaktuk, NT). These hydrologically eroded pingos generally do not result in the formation of a thaw lake, as the meltwater and sediment are transported away from the pingo by spring, lake, or sea water (Babiński, 1982). These erosional processes can take place over the course of years to decades, while the mechanical failure of closed-system pingos can take many decades due to the lowered rate of hydrological erosion. Pingo scars can be identified by the presence of ramparts, ice wedge casts in dilation cracks, and fluvial deposits from the

drainage of the former thaw lake in the centre of the paleopingo (Flemal, 1976; Mackay, 1998).

2.6 Thermokarst Mapping and Modelling

Information about thermokarst landform distribution at national and circum-Arctic scales has lagged behind knowledge of permafrost and ground ice distribution (Kokelj and Jorgenson, 2013). Local- to landscape-scale thermokarst mapping projects focused on specific landform types in limited areas (e.g. Lipovsky et al., 2005; Grosse et al., 2008; Belshe et al., 2013; Arp et al., 2015) are important for the understanding of thermokarst processes, but are not ideal for use in susceptibility studies beyond their spatial scopes. While data scarcity has limited researchers' ability to model thermokarst susceptibility at any scale (Saito et al., 2020), mapping projects such as the Northwest Territories Thermokarst Mapping Collective (Kokelj et al., 2023) have developed landform inventories for increasingly large areas in recent years. A similar inventory showing lake distribution and limnicity change between the 1970s and 2010s using Landsat imagery was assembled in western Alaska (Lindgren et al., 2021).

Depending on the spatial scale of surficial geology maps, thermokarst landforms may or may not be mapped (Yukon Geological Survey, 2020a). The data available in these maps are not exhaustive, since these mapping projects were not intended to focus on thermokarst distribution, and many permafrost regions have not been mapped at a large enough scale to show individual landforms. Remote sensing is key to the development of landform inventories over larger areas (Kääb, 2008): visual image interpretation has been used to map the density of active thaw slumps in northern Yukon, Northwest Territories and Nunavut (Kokelj et al., 2015a) and the percent areal coverage of permafrost peatland complexes in the Taiga Plains of Northwest Territories, as well as the degree of degradation of those complexes (Gibson et al., 2020). Supervised classification of high

resolution satellite imagery has been used to map the development of thermokarst lakes and pools in Alaska (Belshe et al., 2013). These projects are labour intensive, and automation and machine learning have been applied to large-scale mapping projects. For example, tasselled cap trend analysis has been used to monitor retrogressive thaw slump development in northern Yukon and Northwest Territories (Brooker et al., 2014; Lacelle et al., 2015), and digital elevation model (DEM) differencing has been used to identify hillslope thermokarst development in the Canadian Arctic and Alaska (Swanson and Nolan, 2018; Pearson, 2020). Further, random forest modelling has been employed in the Qinghai-Tibet Plateau to compile inventories of 161 300 thaw lakes and 2669 active retrogressive thaw slumps (Wei et al., 2021; Luo et al., 2022).

At the circumpolar scale, the distribution of lake, wetland and hillslope thermokarst landscapes has been modelled using permafrost presence, ground ice content, overburden thickness, ecoregion, topographic ruggedness and soil classification data (Olefeldt et al., 2016). This model was combined with an inventory of thermokarst study sites to produce a map of thermokarst landscape coverage which estimated that lake, wetland and hillslope thermokarst landscapes covered 7.8, 7.1 and 4.9 % of the land area in the northern hemisphere, respectively (Figure 2.6). In North America, this model shows extensive lake and hillslope thermokarst in the Canadian Arctic islands and Arctic Alaska, NWT and coastal Yukon, with the mountainous sub-Arctic regions of Alaska and Yukon and having mainly hillslope and wetland thermokarst. Broadly, this distribution is controlled by overburden thickness, the presence of mountains and precipitation.

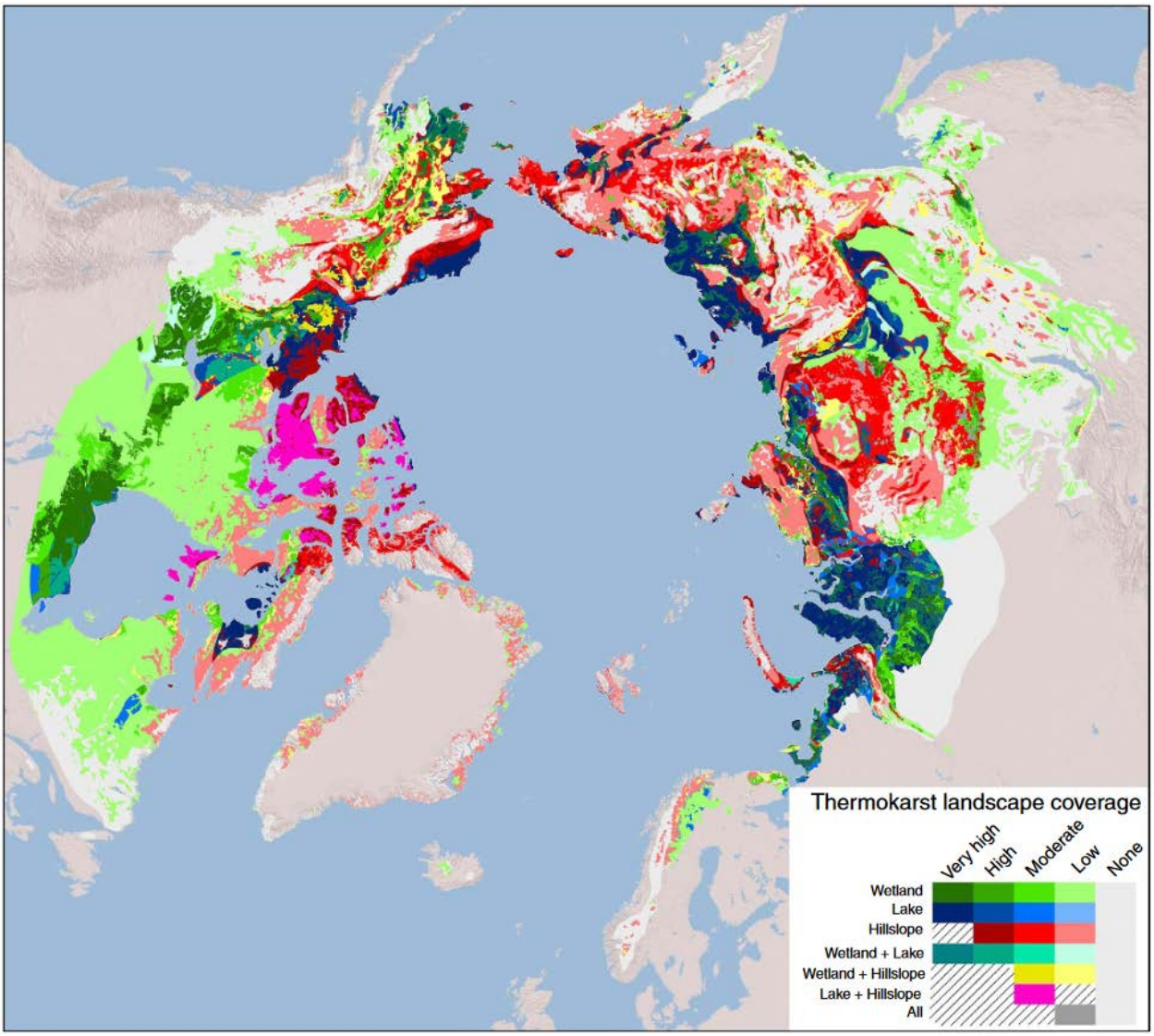

Figure 2.6. Map of wetland, lake and hillslope thermokarst landscape coverage across the circum-Arctic, from Olefeldt et al. (2016). Coverage is classified by percent areal coverage as 'Very High' (60–100), 'High' (30–60), 'Moderate' (10–30), 'Low' (1–10) and 'None' (0–1).

Thermokarst susceptibility hazard mapping faces some of the same challenges mentioned above: a focus on small areas centred on populations and infrastructure rather than national and hemispheric scales (Kokelj and Jorgenson, 2013) and the limited ability of remote sensing techniques to observe subsurface processes (Arenson et al., 2016). The Northern Climate ExChange working group (https://www.yukonu.ca/research/research-centre/climate-change) has produced community-scale permafrost hazard maps for communities in Yukon using topography, geology and permafrost data (Kennedy et al.,

2011a; Kennedy et al., 2011b; Benkert et al., 2015a; Benkert et al., 2015b; Benkert et al., 2016). An inventory of debris flows, active layer detachments and rock slides, as well as a landslide susceptibility model have been developed for a portion of the Yukon-Alaska Highway Corridor (Behnia and Blais-Stevens, 2018). A similar model of permafrost disturbance susceptibility has been developed in Nunavut using DEM-derived variables (Rudy et al., 2016). Machine learning methods have been used with the Qinghai-Tibet Plateau thermokarst inventories (Wei et al., 2021; Luo et al., 2022) to model thermokarst lake and landslide susceptibility in the region (Yin et al., 2021; Wang et al., 2023). Machine learning has also been applied to retrogressive thaw slump mapping at several sites across the Arctic (Nitze et al., 2021).

Several studies have looked at permafrost hazards and thermokarst susceptibility at the circumpolar scale. Using permafrost and ground ice data from the IPA map (Heginbottom et al., 1993) and an active layer thickness change model (Anisimov et al., 1997), a hazard zonation map of permafrost stability was produced for the Northern Hemisphere, which showed higher susceptibility to disturbance at the northern extents of permafrost, and placed all inland Canadian permafrost in the "Low" hazard zone (Nelson et al., 2002). More recently, more detailed data on potential active layer thickening, overburden thickness and mean annual ground temperature was used to develop a circumpolar index of low, moderate and high thermokarst hazard potential (Figure 2.7) (Karjalainen et al., 2019), and modelled ground ice and surface organic content has been used to model the vulnerability of ice-rich permafrost in the Northern Hemisphere to degradation (Saito et al., 2020).

An important aspect of hazards is their potential to bring harm to humans or ecosystems. A circum-Arctic permafrost hazard model which considers the spatial distribution of human populations, infrastructure and potential near-surface permafrost thaw, estimates that 3.6 million people and 69 % of current infrastructure in Northern

Hemisphere permafrost regions may be affected by permafrost thaw by 2050 (Hjort et al., 2018). Linear infrastructure such as highways, railways and pipelines are especially vulnerable. High risk areas are generally those that have high ground ice content and frost susceptible soils, as well as a high potential for thaw.

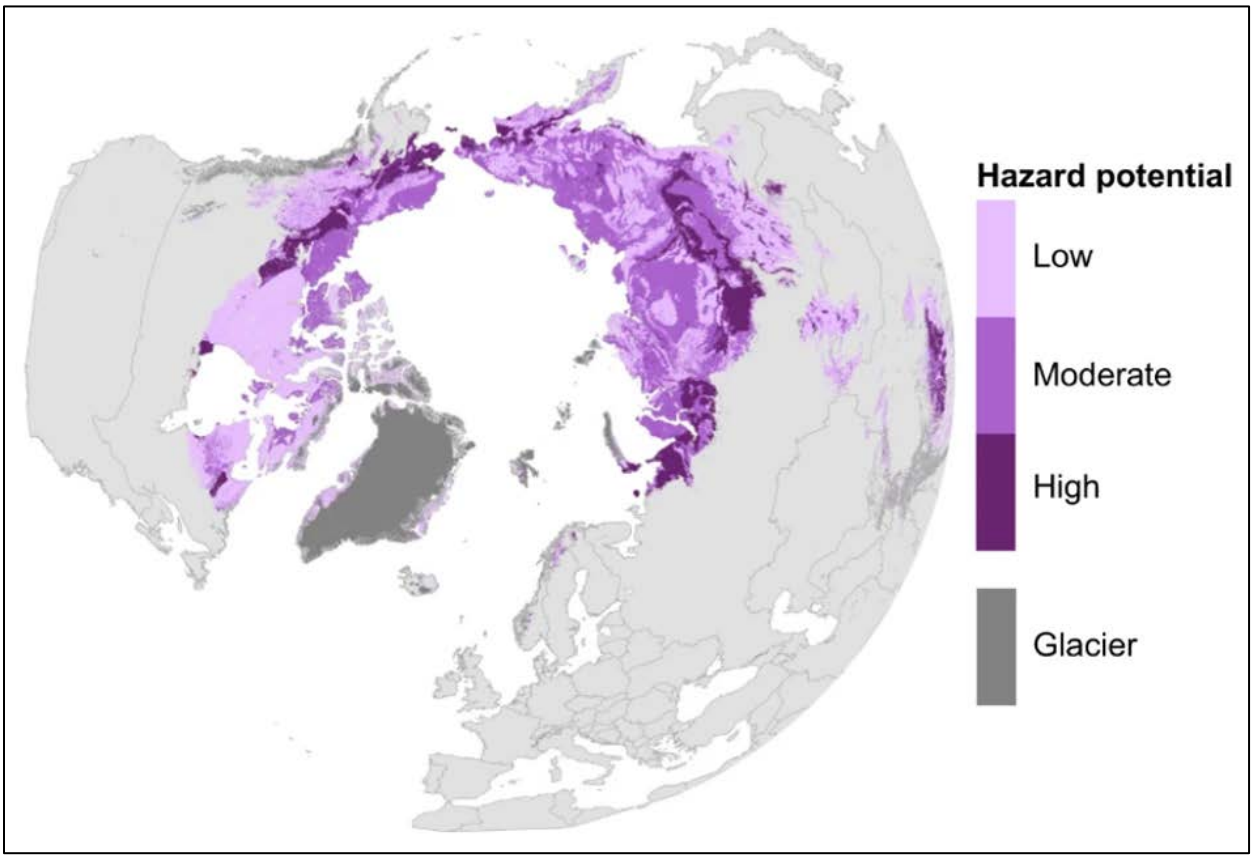

Figure 2.7. Permafrost hazard potential index in Representative Concentration Pathway 4.5 for 2041–2060, from Karjalainen et al. (2019). The index considers settlement potential, risk zonation and an analytic hierarchy process.

Chapter 3. Methods

3.1 Study Area

Yukon (formerly the Yukon Territory) is one of Canada's three territories, and covers 482 443 km^2, bordering Alaska, British Columbia and the Northwest Territories (Figure 3.1). Its southern border is the 60°N parallel and its northernmost point is 69° 38'N at the coast of the Beaufort Sea. Its western border is the 141°W meridian and its eastern border mainly follows the drainage divide between the Yukon and Mackenzie rivers. Yukon had an estimated population of 45 148 in 2023 (Statistics Canada, 2023), with 28 201 of those living in the capital, Whitehorse. 14 First Nations have their traditional lands in the territory, 11 of which are signatories to the Umbrella Final Agreement of 1992 (Umbrella Final Agreement, 1992).

Mountain ranges dominate Yukon's landscape. Most of the territory has a Köppen-Geiger climate classification of Dfc (subarctic), and Dsc (subarctic dry summer season) at lower elevations, while many of the mountain ranges and the Arctic coast have an ET tundra climate (Beck et al., 2023). Twenty-six ecoregions have been identified in the territory, based on differing physiographic, hydrographic, geologic, climatic, soil and ecologic properties (Figure 3.1) (Yukon Ecoregions Working Group, 2004a). The Saint Elias Mountains in southeastern Yukon are extensively glaciated, and much of Yukon is underlain by permafrost. The areal extent of permafrost varies from isolated patches in the extreme south to continuous permafrost found in most mountain ranges and north of the Ogilvie Mountains to the Arctic coast (Heginbottom et al., 1995; Bonnaventure et al., 2012). In much of southern Yukon ground ice content is negligible, while northern Yukon contains areas with medium to high ground ice content (O'Neill et al., 2022). As such, thermokarst affects many of Yukon's landscapes. Several thousand thermokarst

landforms appear in the Yukon Geological Survey's (YGS) Digital Surficial Geology dataset (Yukon Geological Survey, 2020a: see Section 3.2). Further, numerous studies detail thermokarst landslides along the Alaska Highway (e.g. Huscroft et al., 2003; Calmels et al., 2015; Behnia and Blais-Stevens, 2018) and ground subsidence along the Dempster Highway (e.g. Burn et al., 2015; Calmels et al., 2018; Cameron et al., 2023).

Figure 3.1. Map of Yukon. The 26 territorial ecoregions (Yukon Ecoregions Working Group, 2004b) are shown, as is the Dawson City study area.

The Dawson City study area is centred on the town of Dawson City in west-central Yukon, with an area of 9103 km^2 and an extent of 63.48°N to 64.23°N and 138.16°W to 140.44°W (Figure 3.2). Its elevation ranges from 265 to 1382 m, with an average elevation of 718 m. It was chosen as the study area for this project because of the presence of permafrost and thermokarst within it and because it is an area that I am familiar with, having visited Dawson City, the Top of the World Highway and the Klondike goldfields in Bonanza Creek (Figure 3.2) during fieldwork in August of 2018 and 2019.

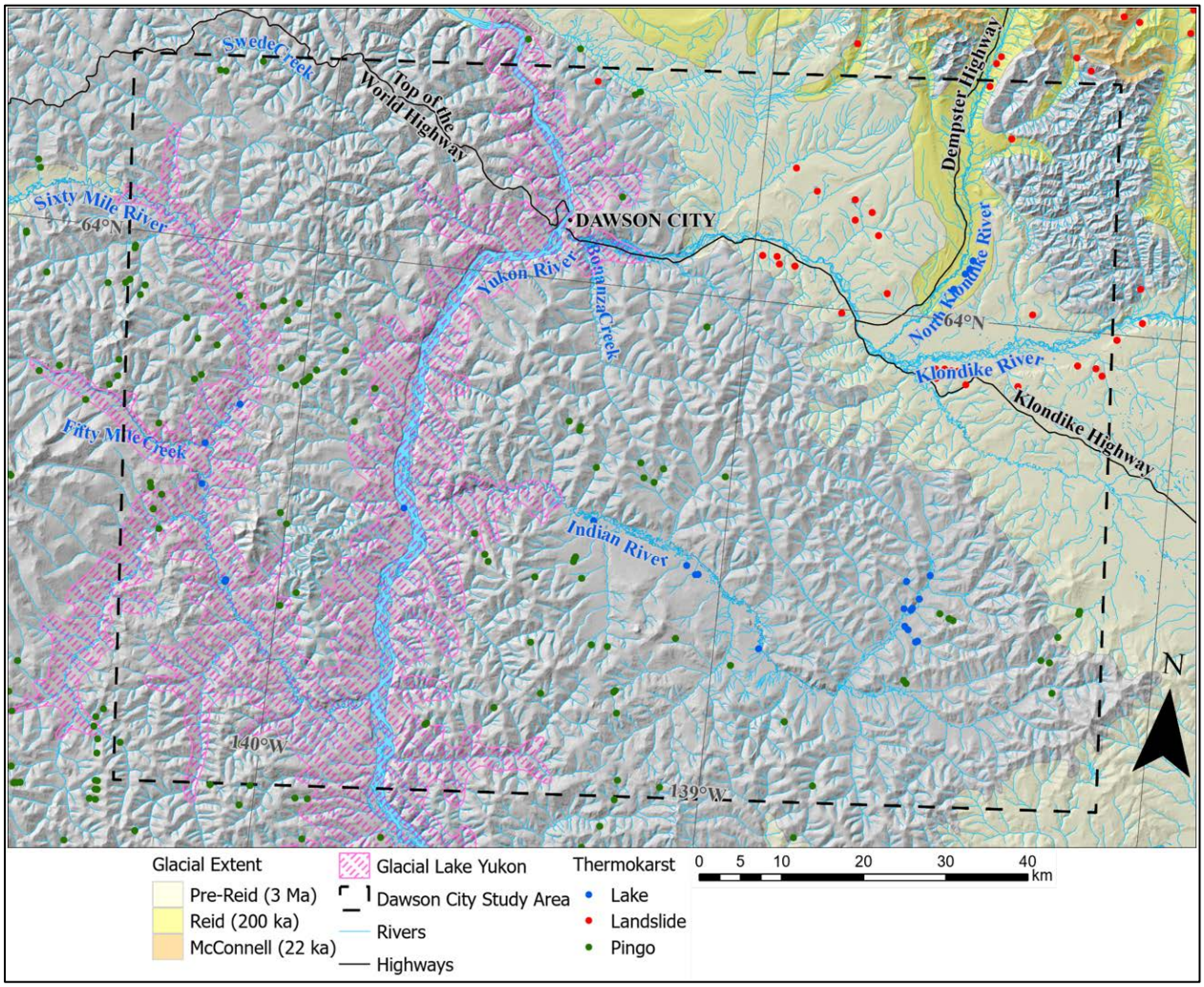

Figure 3.2. Dawson City study area. Thermokarst landforms from the Yukon Geological Survey (2020a) are shown as points. Glacial extents during the Pre-Reid (Pliocene to Early Pleistocene, 3 Ma), Reid (Middle Pleistocene, 200 ka) and McConnell (Late Pleistocene, 22 ka) glaciations are shown in shades of yellow (Yukon Geological Survey, 2020b) and the extent of glacial Lake Yukon is shown in hatched pink (Duk-Rodkin, 1999).

The study area is mainly within the Klondike Plateau Ecoregion, characterized by smooth ridges and V-shaped valleys, extensive colluvial deposits and glaciofluvial terraces, and spruce and mixed spruce-birch forests (Yukon Ecoregions Working Group, 2004b; Froese et al., 2009). The region has numerous open-system pingos (Hughes, 1969), active layer detachments and larger mass wasting events (Benkert et al., 2015b). The largest of these, the Moosehide Slide earth flow/rock glacier directly north of Dawson City, is 300 m high and 600 m long (Brideau et al., 2006). The Klondike Plateau is part of the Yukon-Tanana Terrane, predominantly composed of metasedimentary and metavolcanic rock of Paleozoic and Mesozoic ages (Mortensen, 1992). The Tintina Trench, an 800 km long graben valley resulting from right-lateral faults during the Eocene, passes through the northeast corner of the study area (Roddick, 1967; Duk-Rodkin et al., 2010).

The study area is at the extreme southeast extent of Beringia, the region of North America and Eurasia which remained unglaciated during the last ice ages (Duk-Rodkin and Barendregt, 2011). Local montane glaciers were present in the Ogilvie Mountains to the northeast during the Late Wisconsinan McConnell glaciation 23.9 to 10.7 ka ago, during marine isotope stages 1 and 2 (Figure 3.3) (Bond, 2003; Duk-Rodkin et al., 2010; Duk-Rodkin and Barendregt, 2023). These previously glaciated areas exhibit U-shaped valley systems. The modern Yukon River, which contributes 8 % of all freshwater inflow to the Arctic Ocean (Brabets et al., 2000) flows south-north through the study area. The Yukon River valley was formed by pre-Reid glacial outburst flood of glacial Lake Yukon circa 2.6 Ma ago, and many of its tributaries were formed during the Reid glaciation 311 ± 32 ka ago (Huscroft et al., 2004; Nelson et al., 2009). This glacial history affects the distribution of surficial materials in the study area. Colluvium, alluvium and regolith are the most common surficial materials, while tills are found in the northeastern portion, only in previously glaciated parts of the Tintina trench, and loess deposits are found distributed in some river banks and atop the glaciofluvial terraces.

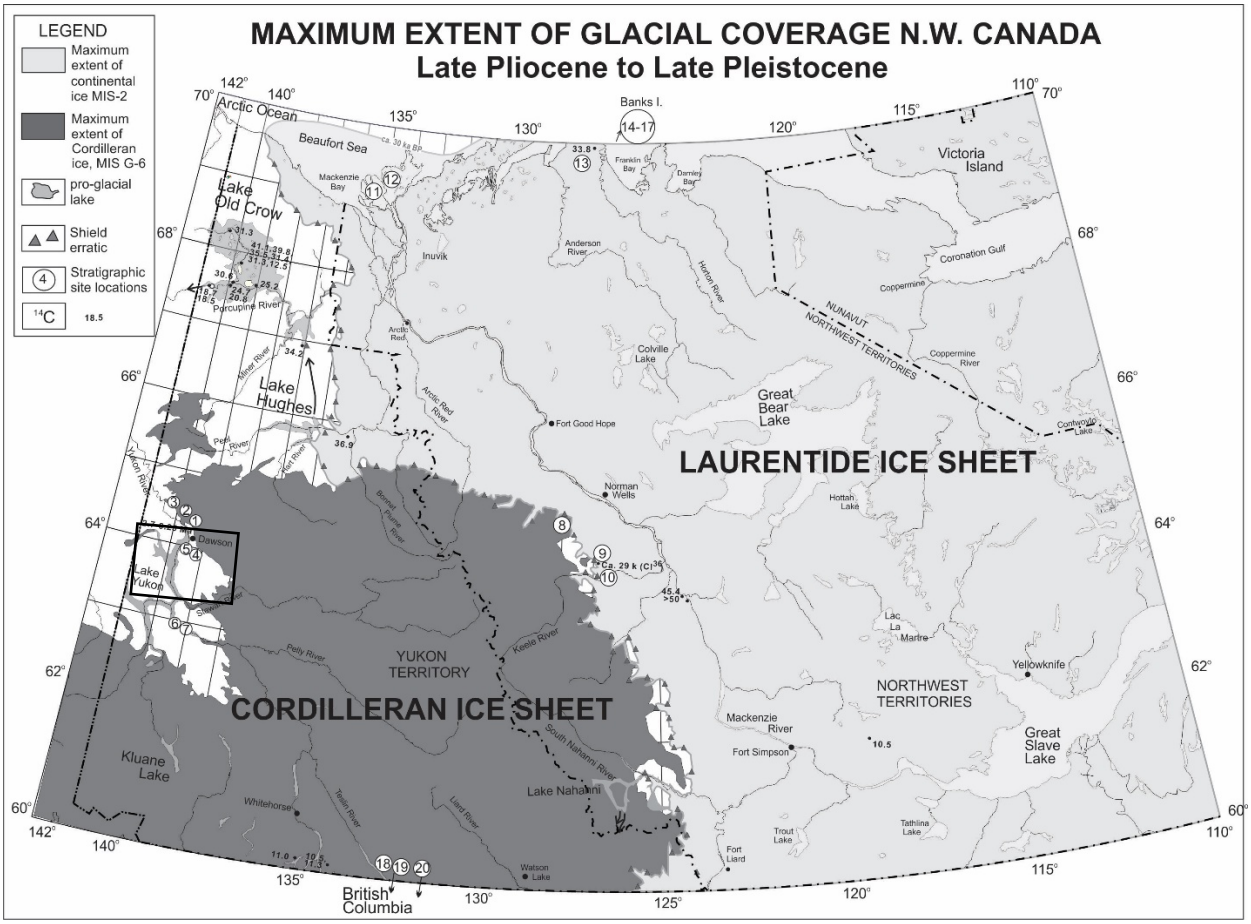

Figure 3.3. Maximum Extent of Glacial Coverage in Northwest Canada from the late Pliocene to the late Pleistocene, from Duk-Rodkin and Barendregt (2011). The Dawson City study area is visible near the western edge of the map, between glacial lake Yukon and the Cordilleran ice sheet.

The area around Dawson City has a subarctic climate in Köppen climate class Dfc (Beck et al., 2023) with a mean annual average temperature of -4.1 °C and an average annual precipitation of 201 mm of rain and 166 cm of snow over the 1981–2010 climate normal period (Environment and Climate Change Canada, 2023). Between 2001 and 2019, the length of the continuous snow season length was between 170 and 234 days (Lindsay et al., 2015). The region is projected to transition into Köppen climate class Dfb by 2070 under all of the representative concentration pathways (Beck et al., 2023), with a warm summer season instead of a cold one.

Currently, the Dawson City study area is within the extensive discontinuous permafrost zone (Figure 3.4) (Heginbottom et al., 1995; Bonnaventure et al., 2012), and permafrost is estimated to be up to 60 thick (Lewkowicz et al., 2011). There are generally negligible to low levels of ground ice (0–10 % volume) throughout the region (O'Neill et al., 2022), although high concentrations, up to 70 % by volume are present in organic and silty strata overlying alluvial gravels in the Klondike goldfields, mainly in the form of ice wedges (Kotler and Burn, 2000; Yukon Ecoregions Working Group, 2004b). Ice-rich alluvial silts have been identified under historical buildings in Dawson City itself (Laxton and Coates, 2010).

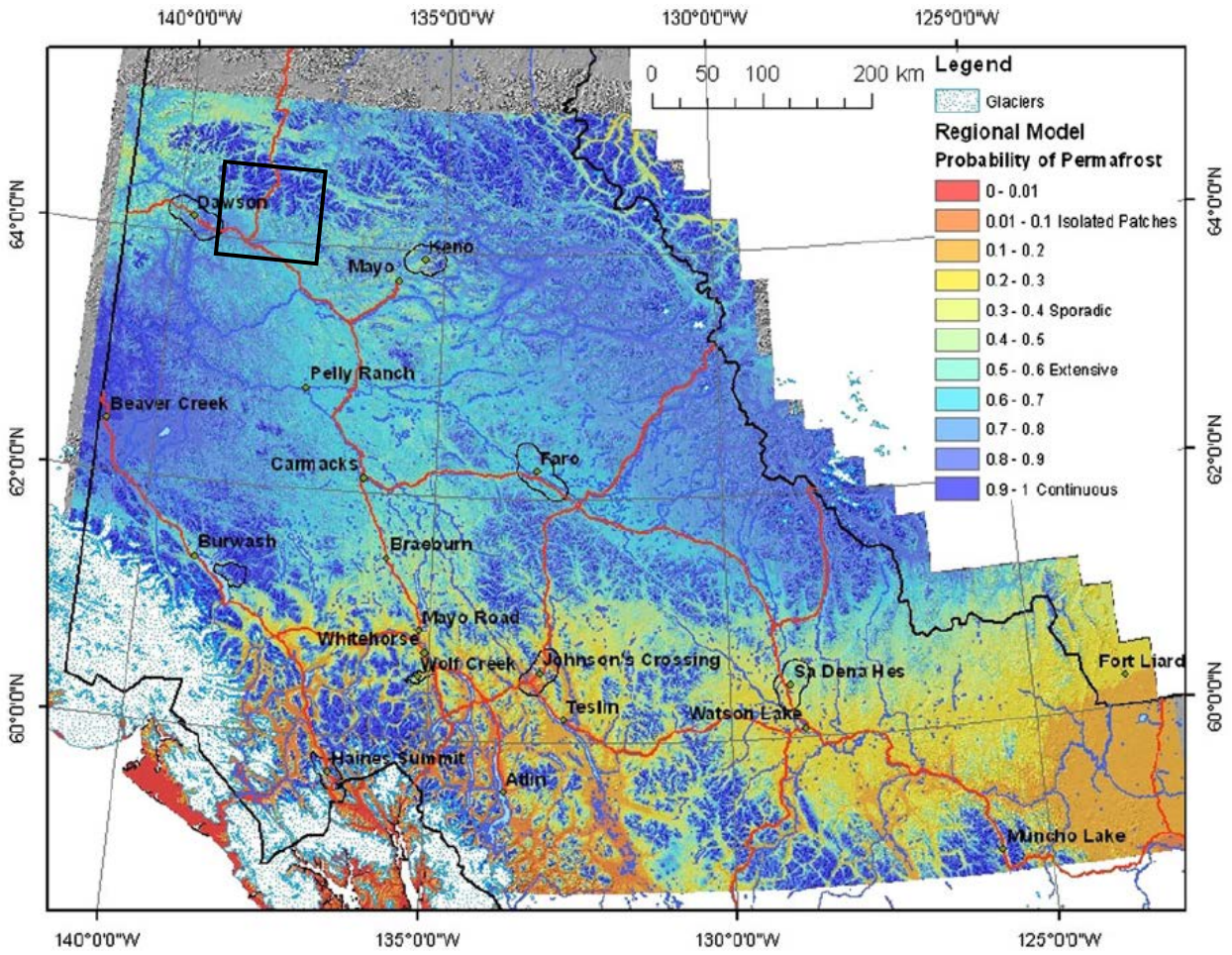

Figure 3.4. Permafrost presence probability map for southern Yukon, from Bonnaventure et al. (2012). The Dawson City study area is visible in the northwest corner, delineated in black.

Historically, the Tr'ondëk Hwëch'in First Nation used Tr'ochëk, at the confluence of the Yukon and Klondike rivers, as a hunting and fishing camp, as well as other sites along the Yukon River and its tributaries. Today, the First Nation has a registered population of 966 people (Government of Canada, 2024). In 2023, Tr'ondëk-Klondike was inscribed as a UNESCO World Heritage Site to protect and honour the history of Indigenous peoples' response to colonial pressures. Dawson City had a population of 1577 in 2021 (Statistics Canada, 2021), and has been continuously inhabited since the Klondike Gold Rush of 1896–1898, when its peak population was around 17 000. The town is the northern terminus of the Klondike Highway and the eastern terminus of the Top of the World Highway, with a ferry over the Yukon River connecting the two. The Dempster

Highway's southern terminus is 40 km east of the town. Over a century of anthropogenic disturbance such as road and building construction, placer mining and forest clearance, has led to thickened active layers and talik development, leading to ground subsidence and building condemnations (Benkert et al., 2015b; Grandmont et al., 2015).

3.2 Thermokarst Landform Inventory

Thermokarst landform data were extracted for the entire territory from the YGS Digital Surficial Geology dataset (Yukon Geological Survey, 2020a). This open access dataset is a digitization of all available Yukon surficial geology maps and includes a standardized terrain feature classification system that largely follows the British Columbia terrain classification system (Howes and Kenk, 1997). The original surface geology maps used for the YGS Digital Surficial Geology dataset were published between 1965 and 2013 with map scales ranging from 1:20 000 to 1:250 000. To create an inventory of thermokarst landforms for this project, a point file with all mapped thermokarst collapses, pingos, collapsed pingos, palsas and landslides in the territory was extracted from the surficial geology dataset. Unfortunately, individual thermokarst landform types were only

mapped in select surficial geology map sheets, and depend on the map series and the mapper(s). Figure 3.5 shows all of the mapped thermokarst features as well as the footprints of the map sheets in which of each of these landforms was mapped in the Dawson City study area. Landslides were mapped over the smallest portion of the study area, followed by pingos and lakes.

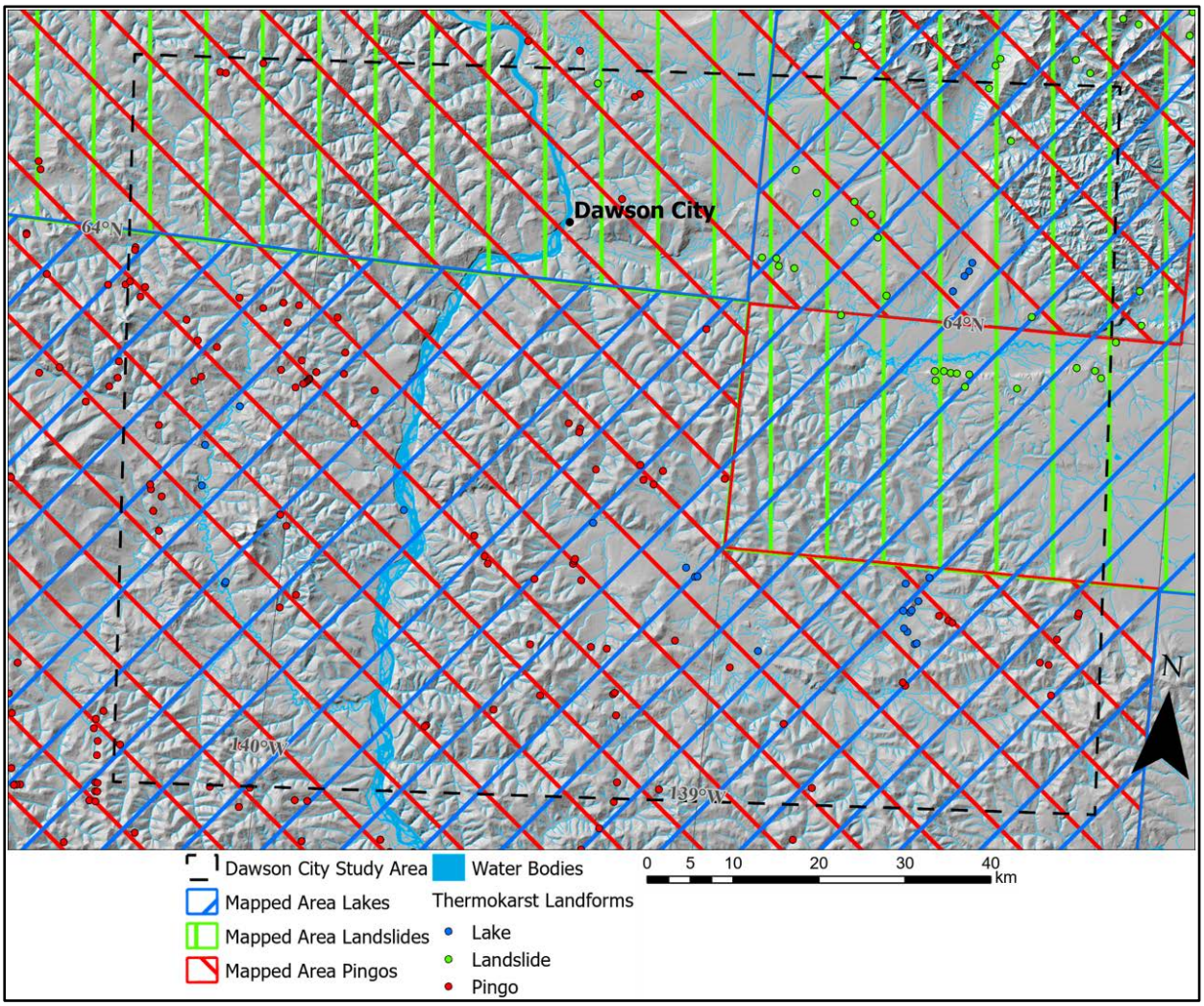

Figure 3.5. Mapping extent of thermokarst landform types extracted from Yukon Geological Survey (2020a). Lakes were mapped in the blue hatched area, landslides in the green hatched area, and pingos in the red hatched area.

For this study, a number of thermokarst classes were combined and others were selectively used. Pingos and collapsed pingos were combined into one 'pingo' group due to the cyclic nature of pingo development (see Section 2.5.4) and the range of years over which the pingos were originally mapped. Further, all features mapped as thermokarst collapses in the YGS Digital Surficial Geology dataset were in fact thermokarst lakes and were all retained for this study. Finally, the geomorphological process codes from Howes and Kenk (1997) were used to ascertain whether or not a landslide resulted from a permafrost process and only hillslope thermokarst features were retained, while landslides not associated with permafrost were omitted from this study's thermokarst dataset. Hence, only landslide features with the geomorphological process code *-LXl* (landslide in ice-rich permafrost) were extracted for this study. Some landslides seemingly associated with permafrost were excluded, either because the meaning of their process codes was unclear and undocumented (e.g. *-LeXl*), or because features with those codes were deemed too large and unspecific to be useful for analysis. The resulting database of thermokarst features used in this study for Yukon and the Dawson City study area is summarised in Table 3.1.

Table 3.1. Count of thermokarst landforms in Yukon and the Dawson City study area, and mapped area within the Dawson City study area from Yukon Geological Survey (2020a).

Landform Type	**Number in Yukon**	**Number of features in Dawson City study area**	**Mapped area within Dawson City study area (km²)**
Thermokarst Collapse	2201	25	7472
Pingo	778	93	7928
Landslide	397	27	3889

3.2.1 Thermokarst Inventory Polygonization

Landforms were delineated in three new feature classes, all mapped at 1:10 000 scale using Maxar Vivid satellite imagery in the World Imagery base layer (Figure 3.6). Most points from Table 3.1 were within 100 m of landforms visible in the imagery. When no landform was visible in the vicinity of the mapped point that feature was removed from the inventory. It is notable that, during this process, features of all three types were observed in the imagery that were not present in the YGS dataset. Lakes were delineated using the *Polygon* tool at the highest seasonal water level, identified by differences in vegetation (visible in Figure 3.6a). Landslides were mapped by the YGS as surficial geology units encompassing the entire landslide from crown to toe. These features were extracted from the digital surficial geology dataset and used for the morphometry analysis. Pingos were delineated using the *Circle* tool, starting in the centre of a visible pingo landform and enlarging the polygon until the edges lined up with the furthest extent of the pingo ramparts. All pingos in this area are circular, and this method of delineating pingos may not be suitable in areas with more varied pingo morphology (e.g. Demidov et al., 2022).

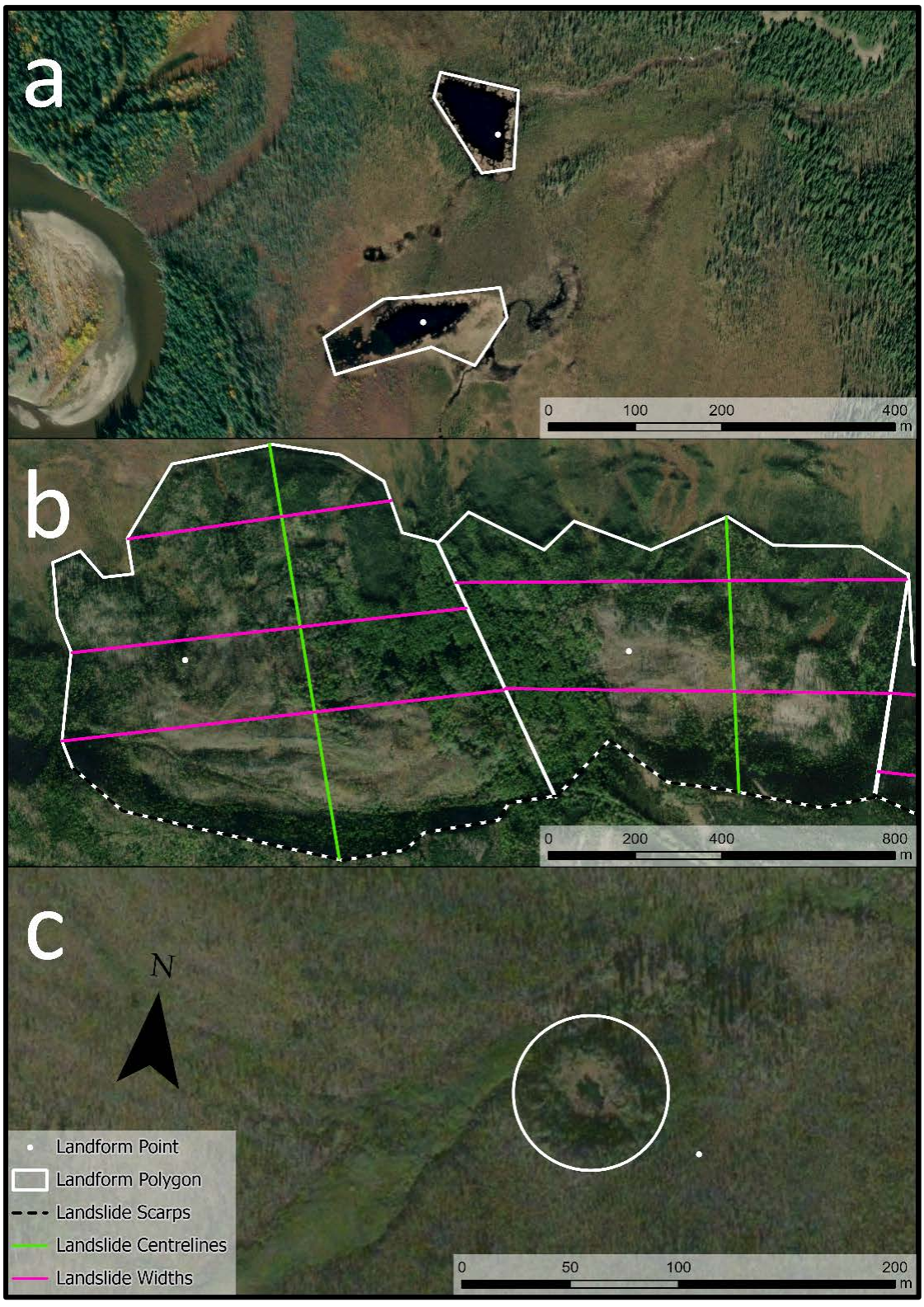

Figure 3.6. Delineation of thermokarst landforms: lakes (a), landslides (b) and pingos (c). Original landform points from the Yukon Geological Survey (2020a) are shown, as well as additional landslide metrics. Base layer ESRI World Imagery.

3.2.2 Thermokarst Landform Morphometry

The selection of metrics for each landform type was informed by studies of similar landforms in other regions (e.g. Niu et al., 2014; Wolfe et al., 2023). For lakes, the area, perimeter, circularity and elongation were measured. Area and perimeter were calculated using the *Calculate Geometry* field calculation function for each polygon feature. The circularity index is a measure of how close to a perfect circle a shape is. It is calculated using the following equation from Morgenstern et al. (2008):

$$Circularity\ Index = 4\pi(a/p^2) \quad (1)$$

where a is area and p is perimeter. Possible values range from 0 to 1 and values closer to 1 are more circular. The *Minimum Bounding Geometry* tool with the *rectangle by width* geometry type parameter was used to find the major and minor axes of lakes. The elongation index is the ratio between major axis length and minor axis length, with values ranging from 1 to ∞ and higher values indicating more elongated lakes. Lake depth is commonly reported in lake morphometry studies (e.g. Morgenstern et al., 2008; Niu et al., 2014), but bathymetry data for the lakes in this study are not available, and therefore it was not reported in this study.

For landslides, the scarps, centrelines and width transects were delineated within the polygon features, and the height, length, width and Fahrböschung were measured. Landslide scarps and scars were only visible in the imagery for 13 of the YGS points in the Dawson City study area. Hence, the following metrics were only recorded for these features. Scarps were traced using snapping along the upslope edge of the landslide, using basemap imagery to verify extent (Figure 3.6b). Centrelines were drawn manually using a straight line from the furthest extent of the terminus to the centre of the crown. Width transects were drawn perpendicular to the centreline at an interval of 200 to 400 m. Individual landslides had between one and four width transects, depending on how

much their width varied. The lengths of these line features were appended to the landform polygon features using the *Spatial Join* tool. Height was calculated as the difference in elevation from the DEM between the top of the crown and the end of the terminus, length as the horizontal distance between the middle of the crown and the end of the terminus, and width as the distance between edges of the landslide body perpendicular to the centreline. Fahrböschung is the ratio between height and length, with higher values indicating a steeper slope angle (e.g. Jiskoot, 2011).

For pingos, height, diameter and average slope were measured. Height was calculated as the difference between the minimum and maximum DEM value in the polygon, and average slope is the mean of all DEM-derived slope values in the polygon. Different ways of reporting pingo slope angle exist (Jones et al., 2012; Wolfe et al., 2023), but the average slope method was chosen over other methods which require slope transects because of the simplicity of its calculation.

3.3 Model Input Data Selection

Permafrost thaw can be affected by a variety of environmental factors. A literature review of other modelling studies was conducted in order to inform the selection of input datasets for this study's thermokarst susceptibility model. Fifteen landslide susceptibility or periglacial modelling studies were reviewed and their explanatory variables are listed in Table 3.2. The results of the literature review indicate that topographic, cryospheric, geologic and environmental variables are included in the susceptibility models. The number of explanatory variables in a single study ranged from two to seven. Slope is the most common explanatory variable, being present in 70 % of landslide susceptibility studies and 67 % of all studies. The topographic variables, elevation, aspect, and topographic wetness index, are also frequently used. Permafrost distribution was infrequently used in these studies, likely due to a lack of data available at appropriate

scales for these local to regional modelling studies. Ground ice distribution, often inferred from sediment type or soil texture, is much more frequently used. Finally, environmental variables such as landcover, NDVI and ecoregion are also used in these studies.

Based on the most common terms extracted from this literature review, the following variables were selected for inclusion in the thermokarst susceptibility analysis presented in this thesis: elevation, slope, aspect, curvature, solar radiation, snow cover, soil/sediment texture, permafrost presence and air temperature. The data sources and role of these variables in Yukon, as well as some additional analysis techniques used to generate them and a justification of the potential role of these variables in thermokarst development are discussed in the following subsections.

Table 3.2. Results of a literature review of periglacial and landslide modelling studies. Listed studies focus on [1]lowland thermokarst (lakes and wetlands), [2]landslides, and [3]other periglacial phenomena (ground ice, permafrost). Independent variables used in each study are indicated with an X, with the count of these indicated in the last row. Independent variables are: elevation, slope, aspect, solar radiation, topographic wetness index, permafrost presence, ground ice content, soil texture, lithology, landcover and climate. Other variables are listed in the last column.

Study \ Independent Variable	Elv	Sl	Asp	SR	TWI	Pf	GI	ST	Lith	LC	Cli	Other Variables
Balser et al. (2009)[1]		X							X	X		
Lara et al. (2016)[1]		X	X		X		X	X		X	X	Fire, land use
Niu et al. (2015)[1]		X	X				X				X	Hydrology
Yin et al. (2021)[2]		X	X	X	X			X			X	Thawing degree days
Behnia and Blais-Stevens (2018)[2]		X	X		X	X		X	X	X		NDVI, curvature
Lewkowicz and Harris (2005)[2]			X				X	X			X	Fire
Nitze et al. (2021)[2]	X	X								X		NDVI
Levy et al. (2013)[2]				X			X					Albedo
Lewkowicz and Way (2019)[2]		X					X				X	Proximity to other landforms, glacial extent
Kokelj et al. (2015b)[2]							X				X	
Lacelle et al. (2015)[2]	X	X	X				X					
Rudy et al. (2016)[2]	X	X		X	X							Distance to water, topographic position
Hjort et al. (2010)[3]	X	X	X		X					X		
O'Neill et al. (2019)[3]						X		X		X		Glacial extent, paleovegetation
Bonnaventure et al. (2012)[3]	X			X		X					X	
Sum	5	10	7	4	5	3	7	5	2	6	7	

3.3.1 Topographic Variables

Topographic variables such as slope and aspect are derived from elevation datasets. Digital elevation models can be either digital terrain models (DTMs), which show the elevation of the land surface, or digital surface models (DSMs), which additionally show the elevation of other environmental features such as vegetation and buildings (Guth et al., 2021). DTMs are more useful than DSMs for geomorphological studies like this one.

Multiple elevation datasets are available in Canada's North, but not all are well-suited to modelling or morphometry analysis. For example, the High Resolution Digital Elevation Model (Natural Resources Canada, 2022) is an elevation dataset derived from optical digital imagery and airborne LiDAR data available at 1 or 2 m resolution, but is not ideal for this study because it only provides a DSM, rather than a DTM in Canada's North, and edge-matching is not done between component datasets, resulting in artifacts. The ArcticDEM is a high-resolution elevation dataset sourced from optical stereo imagery, produced by the Polar Geospatial Centre (Porter, 2018) and is available at between 2 m and 1 km horizontal resolution with a vertical precision of 0.5 m and accuracy of -0.01 ± 0.07 m (Candela et al., 2017). It is not ideal for the susceptibility analysis because it is a DSM product, and it has artifacts and anomalies which could confound the model, as well as voids resulting from cloud cover in the source imagery. Voids in the ArcticDEM cover 12.3 % of the Dawson City study area. The Canadian DEM (CDEM) is a legacy DTM product discontinued in 2011, derived from hypsographic and remotely sensed data. It is available at 0.75' resolution beneath 68° latitude and coarser resolutions above 68° (Natural Resources Canada, 2013). The CDEM's altimetric accuracy within the Dawson City study area is 5–10 m, while in nearby parts of Yukon the altimetric accuracy is 5–70 m, and its reported validity dates range from between 1951–1960 and 1981–1990, while the oldest validity dates in Yukon are from 1946–1950.

For this study, the CDEM was used for the model input data rather than the newer and higher resolution ArcticDEM because its generalized data is more appropriate for modelling purposes, and it lacks artifacts (e.g. data gaps, erroneous values) which can confound a model. CDEM tiles for the study area were mosaicked at 30 m resolution, and multiple topographic variables were derived from this raster in ArcGIS Pro 3.0.0. Slope is the rate of change in elevation over a horizontal distance and can range from 0 to 90°. Slope was derived using the *Slope* tool and the *degree* output measurement parameter. Aspect is the direction that a slope faces and can range between 0 to 360°, where 0° indicates north. Aspect was derived using the *Aspect* tool and the *planar* method parameter. Aspect was reclassified into nine classes: one for each cardinal and intercardinal direction and an additional flat class for terrain with slope < 5°.

Topographic curvature is the rate of change of the land surface's slope. While it can be defined and calculated in many ways (Minár et al., 2020), it generally describes how convex or concave (or, divergent or convergent) a surface is. Curvature can be measured either perpendicular (profile curvature) or parallel (planform or tangent curvature) to a contour line (Wysocki et al., 2000). Additionally, the standard or mean curvature is the mean value of a surface's profile and planform curvatures. Topographic curvature is employed across the earth sciences and has previously been used to, for example, predict landslide (Ohlmacher, 2007) and thermokarst susceptibility (Niu et al., 2015). The *Surface Parameters* tool was used to calculate profile, planform and standard curvature using a 3 x 3 cell kernel. This tool uses the equations for curvature from Zevenbergen and Thorne (1987), and returns positive values for convex surfaces and negative values for concave surfaces (Figure 3.7).

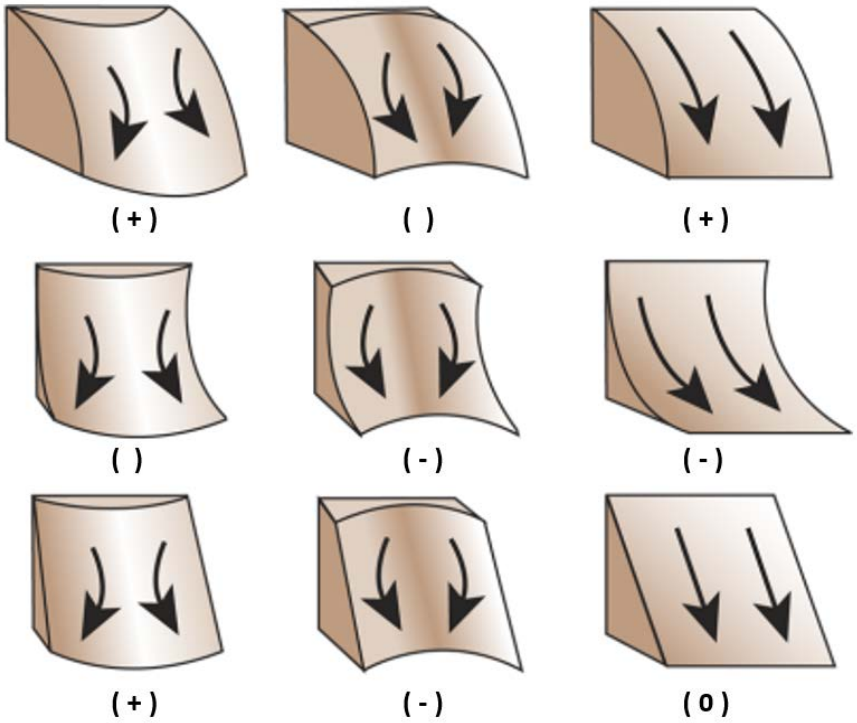

Figure 3.7. The sign of topographic curvature based on Wysocki et al. (2000), after Richter (1962). Convex surfaces have a positive sign and concave surfaces have a negative sign. The top-right and middle-right panels show surfaces with only profile curvature, while the bottom-left and bottom-middle panels show surfaces with only planform curvature. The bottom right panel, showing a uniform slope, has no curvature.

3.3.2 Potential Relative Radiation

The primary source of energy on Earth is the Sun. Solar radiation is mostly in the shortwave wavelengths, and it has a mean intensity, the solar constant, of ~ 1360 W/m^2 at the top of the atmosphere above the subsolar point. The majority of this radiation is transmitted through the atmosphere where it is then either absorbed or reflected by the Earth's surface, with a resultant average irradiance at sea level of 1000 W/m^2 under clear sky conditions. The portion of solar radiation that is absorbed at the Earth surface is re-radiated as thermal energy, or heat. As such, incoming solar radiation is the most important component of the surface energy balance at the Earth's surface. Since permafrost presence and thermokarst development are functions of ground temperature, solar radiation has been shown to affect both permafrost distribution (Hoelzle, 1992),

thaw (Schrott, 1998) and thermokarst development (Kokelj and Jorgenson, 2013; Boike et al., 2015).

There are multiple methods to model solar radiation at the Earth's surface (e.g. Funk and Hoelzle, 1992). The *Area Solar Radiation* tool models incoming solar radiation in WH/m^2 using a terrain model and latitude/longitude coordinates. Potential Relative Radiation (PRR) is an alternative surface radiation model (Pierce et al., 2005). Intended for community vegetation analysis, it has seen applications as a proxy for ground temperature in forestry, agriculture and mammal habitat modelling (e.g. Lookingbill and Urban, 2005; Spencer et al., 2007). The PRR model requires a terrain model and solar altitude and azimuth angles. In the original application of the PRR model, hourly hillshades were generated using the *Hillshade* tool during daylight hours for the day with the closest-to-average solar period for each month of the growing season. This captured the effects of slope, aspect and topographic shading on surface radiation intensity. The results range between 0 and 255 for each individual hillshade and are dimensionless, meaning that its values do not have units. The range of values is inherent to hillshades and is the maximum number of values in an 8-bit colour scale. This means that while the PRR model works well at showing variability in radiation intensity across a study area, it is not applicable as part of an energy balance model. The model does not take into account diffuse radiation, atmospheric transmittance, the projection effect, or topographic shading by large features outside the extent of the input DEM.

The PRR model is ideal for this project because, in thermokarst susceptibility modelling, the absolute value of irradiance at a location is not as important as the relative amount of radiation in one part of the landscape as compared to that in other locations. For this project, an improved version of PRR was developed which 1) corrects for differences in radiative intensity due to the projection effect, and 2) corrects for the

spatiotemporal variability in surface albedo and insulation due to snow cover. Figure 3.8 shows the workflow used to generate the PRR model output used in this study.

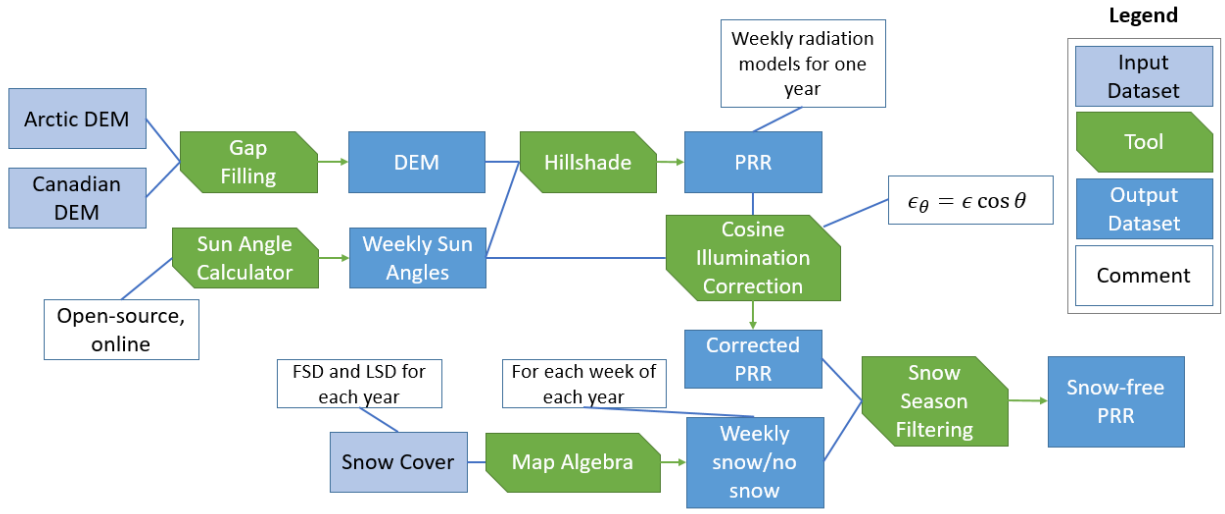

Figure 3.8. Workflow developed in this study for the construction of the Potential Relative Radiation model.

Sun altitude and azimuth angles were obtained using the *Position of the Sun Spreadsheet* (Giesen, 2020) for the central location of the Dawson City study area (64°N, 139°W). For one day at the start of each week of the year 2021, Sun altitude and azimuth values were calculated once every two hours during daytime, starting at sunrise and finishing closest to sunset (at sunset or within two hours prior to sunset). This resulted in a total of 359 sets of sun angles, with the number of calculated sun angles per day ranging from two to 11.

The *Hillshade* tool was used with the DEM as the input raster. All tool parameters were left at their default values, except for the sun altitude and azimuth. One hillshade was produced for each set of sun angles, resulting in 359 hillshades. At this stage, a correction for the projection effect was applied. The projection effect results in illumination intensity decreasing with lower altitude angles, as a constant amount of radiation is spread across a larger surface area (Figure 3.9). Hence, the projection effect is most pronounced in high-latitude regions, and also varies seasonally. To include this

effect in the PRR model, each hillshade was multiplied by the cosine of its sun altitude angle, following:

$$\epsilon_{\emptyset} = \cos \emptyset \, \epsilon \qquad (2)$$

where $\epsilon_{\emptyset}$ is radiation intensity corrected to account for the projection effect, $\emptyset$ is the Sun's altitude angle and ϵ is radiation intensity without the projection effect.

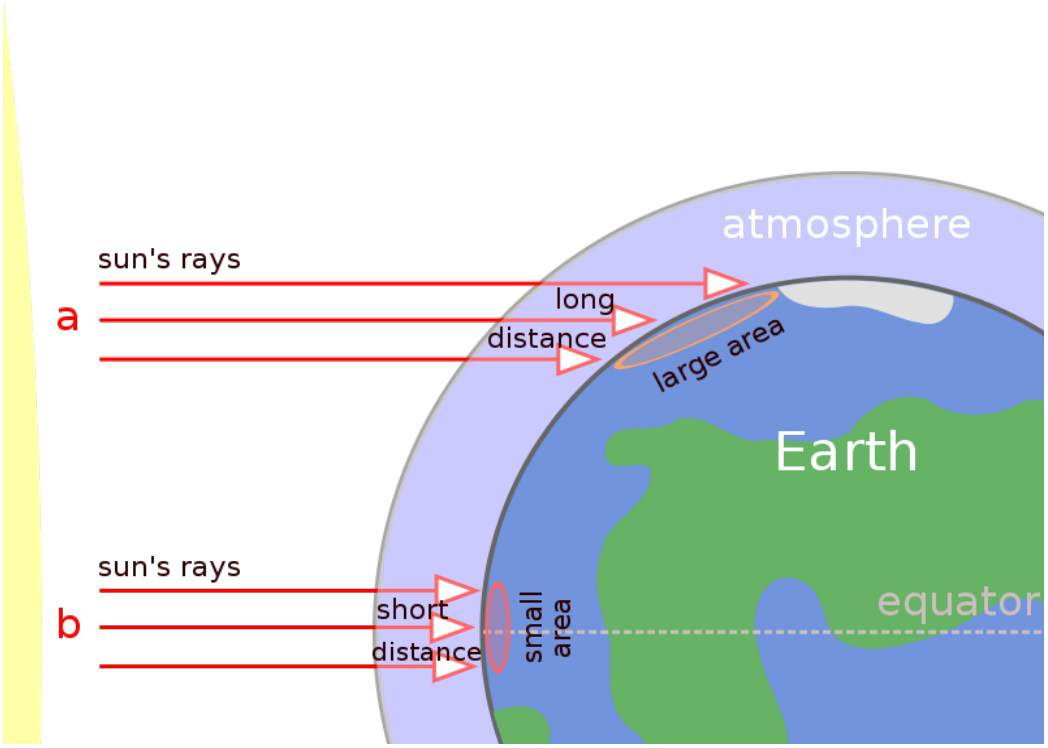

Figure 3.9. Illustrated explanation of the projection effect based on Stiling (2001), by Peter Halasz. This shows that equal amounts of solar radiation in locations (a) and (b) cover different areas at different latitudes. The same effect is seen longitudinally between sunrise, solar noon and sunset. It is important to note that while the atmosphere is depicted here, it plays no role in the projection effect.

The projection effect correction reduced the PRR values by between 35 and 98 %, with early morning, late afternoon, and wintertime hillshades being reduced the most. This means that the PRR model now accounts for daily and seasonal changes in solar radiation intensity due to the projection effect, though it still does not account for diffuse radiation or atmospheric transmission. The corrected hillshades were added together for each individual day to give 52 weekly rasters showing PRR for one day of each week of

the year. These weekly values are representative in any given year because the solar constant and topographic controls on radiation do not vary significantly over the 20-year time period that the snow cover data incorporated into the model are available for.

Even thin snowpacks can block a significant amount of sunlight from reaching the ground surface: 10 cm of snow blocks > 95 % of visible light transmittance and > 99 % of near-infrared transmittance (Perovich, 2007). Late-winter snow depth measurements from the Midnight Dome snow pillow station in Dawson City between 2000 and 2016 indicate an average winter snow depth of 70 cm (Vionnet et al., 2021). Therefore, the implementation of snow cover into the PRR model assumes that any snow cover completely blocks all light from reaching the ground surface (equivalent to 100 % albedo). There can be two definitions of snow season: full snow season (FSS) and continuous snow season (CSS). FSS is measured from the day of the first snowfall in the autumn to the last day with snow on the ground in spring, while CSS is the longest unbroken period of time in winter during which there is snow on the ground. CSS is not affected by unseasonal early snowfall, and is therefore shorter than FSS.

The MODIS-derived Snow Metrics dataset (Lindsay et al., 2015) was used to incorporate the spatiotemporal variability in snow cover into the PRR model. This dataset uses daily snow cover products (Hall et al., 2002) from NASA's Terra satellite's Moderate Resolution Imaging Spectroradiometer (MODIS) sensor and is available for Alaska and parts of Siberia and Canada (including all of Yukon) at 500 m horizontal resolution and a variety of temporal resolutions. Weekly binary snow cover rasters were extracted and multiplied by the PRR hillshades for corresponding weeks. When snow is present in a grid cell, PRR values were multiplied by zero. This process was done once for the FSS data and once for the CSS data. Since the Snow Metrics dataset covers the years 2001–2020, this resulted in 1040 weekly PRR rasters. Finally, these weekly products of PRR and

snow cover were summed and all rasters were normalized to a range between 0 and 1 for ease of interpretation.

3.3.3 Soil and Sediment Texture

Soil and sediment texture were been used as proxies for segregated ground ice content in this study (see Section 2.4.1). Soil texture data for all of Yukon were obtained from SoilGrids 2.0, an observation-based globally interpolated soil property raster dataset available at 250 m horizontal resolution (Poggio et al., 2021). From this dataset the gravimetric silt and clay data from the top 5 cm of soil were extracted and summed to produce a raster of percent fines by weight. The top-most depth interval was chosen because, at the time of this analysis, there was no variation in data values across depth in Yukon in the SoilGrids 2.0 dataset.

Surficial material texture data were extracted from the YGS Digital Surficial Geology dataset (Yukon Geological Survey, 2020a). The surficial material texture attribute adapted from Howes and Kenk (1997) describes up to three of the most prevalent particles by volume in a terrain unit. These data were classified into 4 classes according to the presence of three frost susceptible fines, which are clay, silt or mud (a mixture of silt and clay) (*-c, -z, -m* respectively) according to Table 3.3.

Table 3.3. Texture classes indicating presence of frost susceptible fines in surficial material, derived from Yukon Geological Survey (2020a).

Class	Rule
High	c, z or m most dominant texture
Medium	-c, -z or -m second most dominant texture
Low	-c, -z or -m third most dominant texture
None	-c, -z or -m not present

3.3.4 Permafrost and Air Temperature

Air temperature data at 2 m from the ground for the study area were obtained from the ERA5 global reanalysis dataset (Hersbach et al., 2020). Hourly data at 0.25° resolution from 2000–2021 were averaged to find mean air temperature for that period. At Dawson City's latitude, each cell is approximately 12 x 28 km.

Modelled permafrost presence probability data were obtained from Bonnaventure et al. (2012). This 30 m resolution dataset covers the southern and central Yukon only, including the Dawson City study area, as well as northern-most British Columbia. The model is based on regional basal temperature of snow models and incorporates the effect of air temperature inversions on ground temperature (Bonnaventure et al., 2012).

3.4 Thermokarst Landform Distribution

In order to better understand the spatial distribution of thermokarst landforms within the Dawson City study area, two components of their distribution were analyzed: the position of thermokarst landforms in relation to the rest of the landscape, and their position in relation to one another. For the first part, elevation, aspect, slope and PRR values were extracted to a point file based on the centrepoints of the 30 m CDEM within the Dawson City study area. The values of these topographic variables at points intersecting the landform polygons were compared to the values from the rest of the study area using general statistics and histograms.

For the second part, average nearest neighbour, a spatial clustering analysis, was applied in ArcGIS Pro 3.0.0. Average nearest neighbour is a ratio between the mean observed distance from each landform to its nearest neighbour and the expected distance, if the points were distributed randomly (Getis, 1964; Davis, 2002). Values less than 1 indicate clustering, and values greater than 1 indicate dispersion. Ratios and accompanying statistics were calculated for each landform using the *Average Nearest*

Neighbour tool, using the mapped areas within the Dawson City study area from Table 3.1 for the *area* parameter.

3.5 Generalized Linear Modelling of Thermokarst Susceptibility

Generalized linear models (GLM) are a type of linear regression model which allow for non-linear relationships between a response variable and explanatory variables, and which can accommodate both continuous and categorical explanatory variables (Nelder and Wedderburn, 1972). GLMs using logistically-distributed data are called logistic regressions, and are commonly applied in geology and geomorphology, especially in landslide susceptibility studies (e.g. Atkinson et al., 1998; Bonnaventure and Lewkowicz, 2008; Budimir et al., 2015; Riegel et al., 2020; Yin et al., 2021); glacier surging (Atkinson et al., 1998; Jiskoot et al., 2000) and soil erosion (Avand et al., 2023). Logistic GLM is the most appropriate choice of model for this study because the response variable is binary (thermokarst presence/absence) and several of the explanatory variables are categorical (e.g. aspect and surficial material) or not normally distributed. These constraints mean that multiple linear regression is not appropriate for these data.

In a GLM, generalized linear regressions are performed between the response variable and each explanatory variable. These linear models are then transformed according to the distribution of the response variable using a link function, and their performance is assessed by comparing the modelled deviance to that of a null model containing only an intercept with no explanatory variables. A selection of significant univariate models based on model deviance is incorporated into a multivariate model, $f(x_i)$, through stepwise regression as follows:

$$f(x_i) = a + \sum_{k=1}^{n} \beta_i x_{ik} \quad (3)$$

where a is the intercept (a constant), x_{ik} are the explanatory variables and β_i are their associated coefficients (Atkinson et al., 1998). Ultimately, only the optimal multivariate

model is retained. In the context of this study, the landscape exhibits a binary thermokarst response to environmental variables (i.e. thermokarst is present or absent). Hence, thermokarst susceptibility follows a logistic distribution. Logistic distributions can be modelled in GLM using the logit link function:

$$logit(x) = \ln \frac{P_i}{1-P_i} \quad (4)$$

where P_i is the probability of an event occurring (Nelder and Wedderburn, 1972). To aid in model interpretation, GLM results are presented as log odds:

$$P_i = \frac{e^{f(x_i)}}{1+e^{f(x_i)}} \quad (5)$$

An input dataset for the GLM of thermokarst susceptibility was assembled by creating a pointfile from the centrepoints of a 30 m raster with the same extent as the Dawson City study area. Presence and absence of each thermokarst landform type, as well as the value of each explanatory variable, were extracted to this pointfile's attribute table and imported into *R Statistical Software v4.2.2* (R Core Team, 2022) using the *data.table* package (Dowle and Srinivasan, 2023). Then, null models and univariate models of each landform type were made using the *glm* function in the *stats* package. Models with categorical explanatory variables (e.g. aspect has nine classes) have a single intercept, but unique coefficients for each class. A complication associated with using categorical variables in linear modelling is that one class is used as a reference class and is not given a coefficient. This class needs to be indicated before running the model (this is called releveling), but can be varied, and is usually selected by assuming that this class has the smallest effect on the response variable. Reference class selection requires an understanding of the underlying processes being modelled, but can be straightforward (e.g. lakes do not form on slopes). Therefore, the categorical variables were releveled for each landform to optimize model interpretation (e.g. West aspect was the reference class for lakes, so that a coefficient was generated for flat aspect).

Three statistical values were used to assess model performance and fit optimal models. First, the Akaike Information Criterion (AIC) (Akaike, 1974) is an estimate of a model's goodness-of-fit:

$$AIC = n\ln(\sigma^2) + 2K \quad (6)$$

where n is the sample size, σ^2 is model variance and K is the number of model parameters. Lower AIC values indicate higher quality compared to other models using the same response variable. Second, the p-value is an indication of a model's statistical significance, with lower values indicating higher significance. Finally, the reduction in deviance per degrees of freedom compared to the null model (ΔD/Δdf) is a measure of how much deviance is explained by each explanatory variable. Degrees of freedom (df) is a count of how many parameters a model contains. In models with categorical variables, each class except for the reference class counts as one parameter. ΔD/Δdf is used to select variables for inclusion in an optimal model, and favours parsimonious models.

Optimal models were fitted in a stepwise manner following Atkinson et al. (1998); the statistically significant univariate model with the highest ΔD/Δdf and lowest AIC statistic was selected as the first variable of the optimal models (see Section 4.3). Then, the next best variables were tested in multivariate models. If the addition of a second variable resulted in a ΔD/df greater than that of the univariate model, it was kept as part of the optimum model. The results of the optimal models were converted into a spatial model using the *raster* package and imported into *ArcGIS Pro* for interpretation and mapping. Model results were classified into three susceptibility categories (High, Medium and Low) using the Jenks natural breaks method and mapped in the Dawson City study area.

3.6 Thermokarst Susceptibility Model Validation

The three thermokarst susceptibility models for lakes, landslides and pingos were trained in the Dawson City study area and then applied to the rest of the territory. These results were mapped and visually inspected. The YGS landform points were used as testing datasets to validate the performance of each of the models. The susceptibility classification of the YGS points in each of Yukon's ecoregions was analyzed to determine spatial differences in the performance of the models.

A number of points equal to that of the YGS points for each of the three landform types (see Table 3.1) were randomly distributed across the territory using the *Create Random Points* tool to act as a control against the YGS points. The modelled susceptibility values at these random points and the YGS points were extracted and χ^2 goodness of fit tests were run to verify whether a significant difference existed between their values, thereby showing whether or not the models accurately predicted known instances of thermokarst presence.

Chapter 4. Results

4.1 Snow Cover and Potential Relative Radiation

Descriptive statistics for snow season lengths in the Dawson City study area from 2001–2020 are presented in Table 4.1. Two types of snow season were calculated for the study area for each year from 2001–2020. Continuous snow season (CSS) length is the longest continuous period of time each winter during which there is snow on the ground. Full snow season (FSS) length is slightly longer, measured from the day of the first snowfall in the autumn to the last day with snow on the ground in spring. The FSS, therefore, can include periods without snow. Often this occurs at lower elevations on south-facing slopes, and as a result of unseasonal snowfall events in early autumn or late spring. The minimum and maximum values in Table 4.1 represent the locations that had the 20-year averaged shortest and longest average period of snow cover, while the mean value is the spatially-averaged value for the entire study area.

Table 4.1. Descriptive statistics for the 20-year average continuous and full snow season length in the Dawson City study area between 2001–2020, calculated using data from Lindsay et al. (2015).

	Minimum length (days)	**Maximum length (days)**	**Mean length (days)**
CSS	161	232	189
FSS	178	287	217

The 20-year average length of the continuous and full snow seasons presented in Table 4.1 were subsequently used to adjust the radiation values generated using the PRR model described in Section 3.3.2, where only snow-free days were retained. Descriptive statistics for the continuous (PRR_{CSS}) and full (PRR_{FSS}) snow season PRR models are shown in Table 4.2. PRR values are dimensionless, and do not represent any physical value of

radiation. Since the FSS is longer than the CSS, the PRR_{FSS} model result has slightly lower radiation values than those of the PRR_{CSS} model. The model values have been normalized from 0–1, with one being the maximum value from the PRR_{CSS} model.

Table 4.2. Descriptive statistics for PRR_{FSS} and PRR_{CSS} models in the Dawson City study area.

	Minimum	Maximum	Mean
PRR_{FSS}	0.10	0.94	0.55
PRR_{CSS}	0.13	1.00	0.65

4.2 Thermokarst Landform Distribution in the Dawson City study area

The thermokarst landform inventory extracted from the Yukon Geological Survey's Digital Surficial Geology dataset (Yukon Geological Survey, 2020a) is mapped in Figure 4.1. There are 25 lakes, 27 landslides and 93 pingos in the study area, but these landforms were not mapped across the entire study area (see Figure 3.5).

Thermokarst lake presence in the Dawson City study area is limited to the floodplains of major tributaries of the Yukon River such as the Indian, North Klondike and Sixty Mile Rivers. These are some of the only flat locations in the study area, and the fluvial and glaciofluvial sediments here are thicker and more frost susceptible than upland colluvium. In the rest of Yukon, thermokarst lakes were generally only mapped along highway corridors such as the Alaska and Dempster Highways. Of note, the thermokarst lakes in the Old Crow Flats were are not present in the YGS dataset. Landslides in the Dawson City study area are found predominantly on the terraces and slopes above the Klondike River. In the rest of Yukon, landslides have been mapped in isolated locations (e.g. the McQuesten Highlands and the Peel Plateau, etc.). In the Klondike Plateau, pingos occur at the bottom of low-order streams in unglaciated areas.

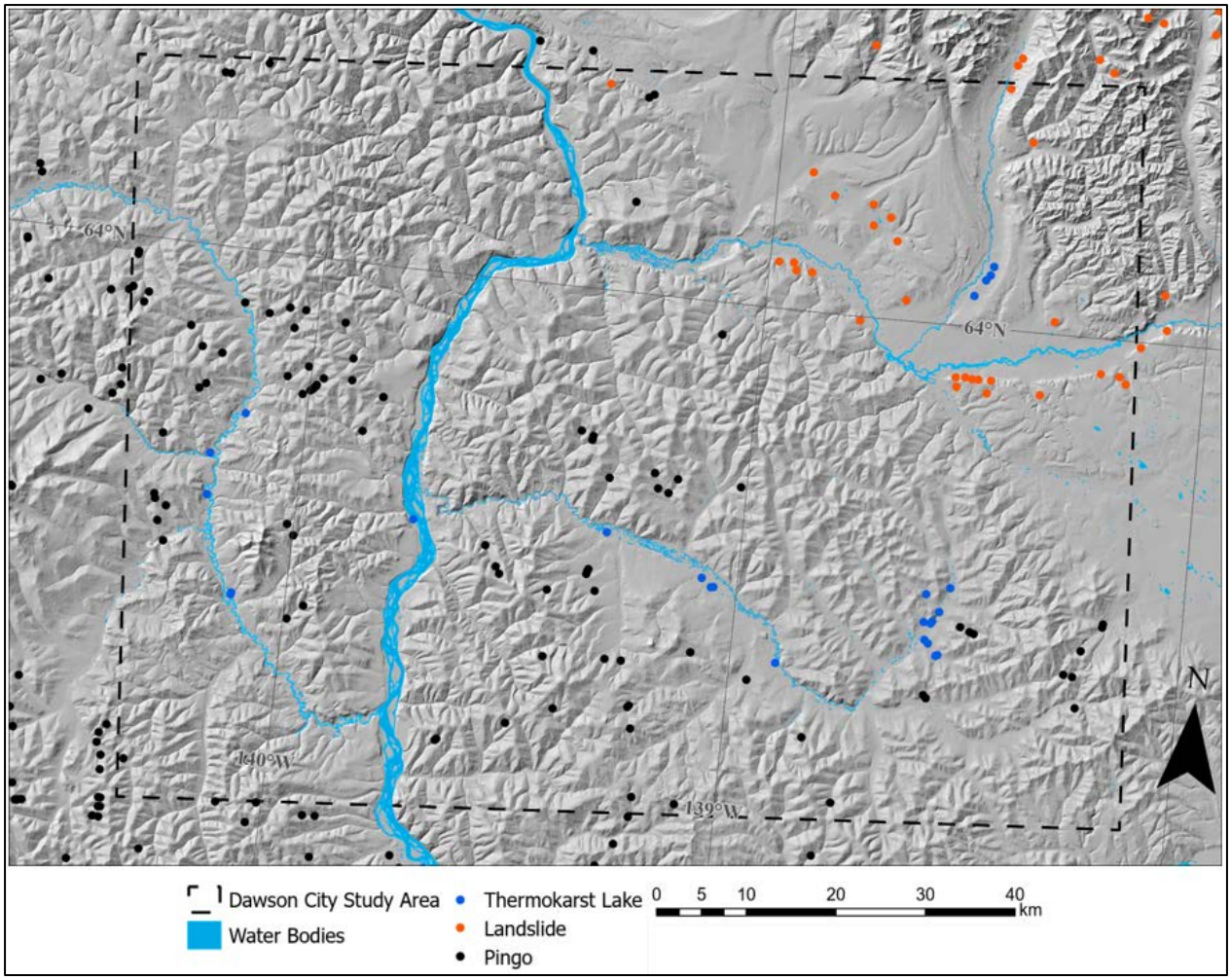

Figure 4.1. Map of thermokarst lakes, landslides and pingos mapped by the Yukon Geological Survey in the Dawson City study area.

Few pingos are found outside of the Klondike Plateau, with exceptions in the Yukon Plateau and the Eagle Plains. While the nearby Tuktoyaktuk Peninsula in Northwest Territories contains approximately 1350 pingos, and pingos have been observed on the Yukon Coastal Plain (Mackay, 1979), none were mapped there by the YGS. The lower prevalence of pingos on the Yukon Coastal Plain compared to in the Tuktoyaktuk Peninsula can likely be attributed to the difference in sediment type.

The Dawson City study area has a large human footprint resulting from placer mining during the Klondike gold rush (Grandmont et al., 2015), concentrated along the Klondike and Indian Rivers and Bonanza Creek. Roadbuilding and the deposition of

tailings likely erased some landforms, and can possibly explain the absence of pingos from the Bonanza Creek watershed. Thermokarst lakes are observed adjacent to many of these tailings, but most of these do not appear in the YGS dataset.

The elevation of each landform type compared to the hypsometry of the study area is shown in Figure 4.2. Here, it can be seen that thermokarst lakes range in elevation from 330 to 600 m, with the largest concentration at around 550 m. Landslides range in elevation from 400 to 715 m, with the highest concentration at 580 m. Pingos range in elevation from 465 to 1000 m, with the highest concentration at 670 m.

The slope of each landform type compared to the slope of the study area is shown in Figure 4.3. Almost all thermokarst lake slope values are equal to zero. The values above zero are most likely in places where the lakeshore recedes seasonally. Landslides have slopes ranging from zero to 20°, with the highest concentration at 10°. This range is due to the fact that the polygons include the entire footprint of the landslide from scarp (highest slope values) to toe (lowest slope values). Pingos have the same range in slope as landslides, though the highest concentration is closer to 4°.

The aspect of each landform type is shown in Figure 4.4. While most lakes are in areas with very low slope, and therefore have no aspect, the remainder are evenly distributed across aspects, with the largest number on west aspects. The majority of landslides (> 50 %) are on north aspects. Pingos are also somewhat evenly distributed across aspects, but with a tendency towards a southern aspect. This is likely due to the normal pattern of pingo collapse, where a pingo's south-facing slope starts to subside and destabilize first due to greater exposure to solar radiation (Babiński, 1982).

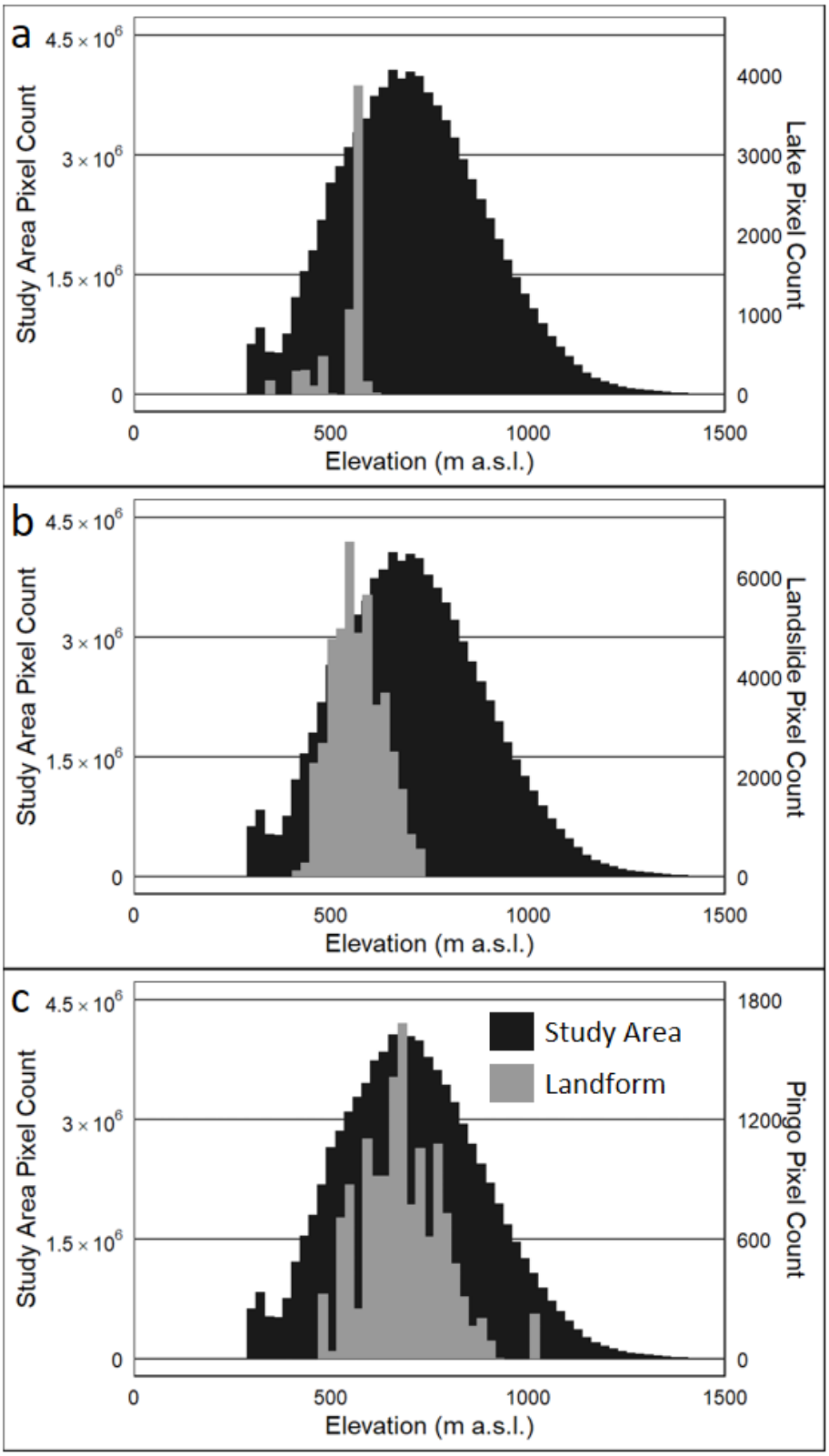

Figure 4.2. Histograms of the elevation of points within (a) thermokarst lake, (b) landslide and (c) pingo polygons compared to the hypsometry of the Dawson City study area.

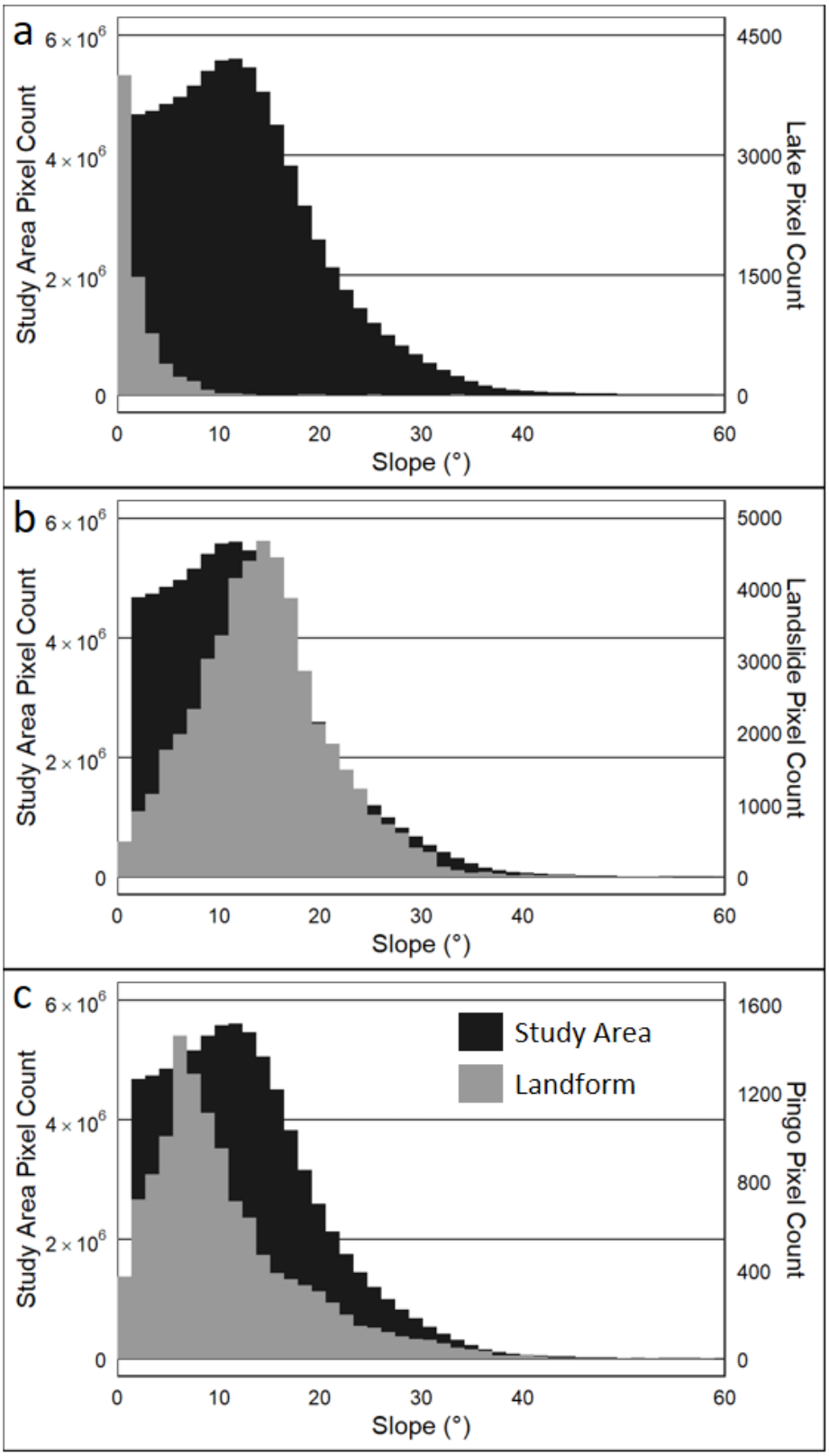

Figure 4.3. Histograms of the slope of points within (a) thermokarst lake, (b) landslide and (c) pingo polygons compared to the slope of the Dawson City study area.

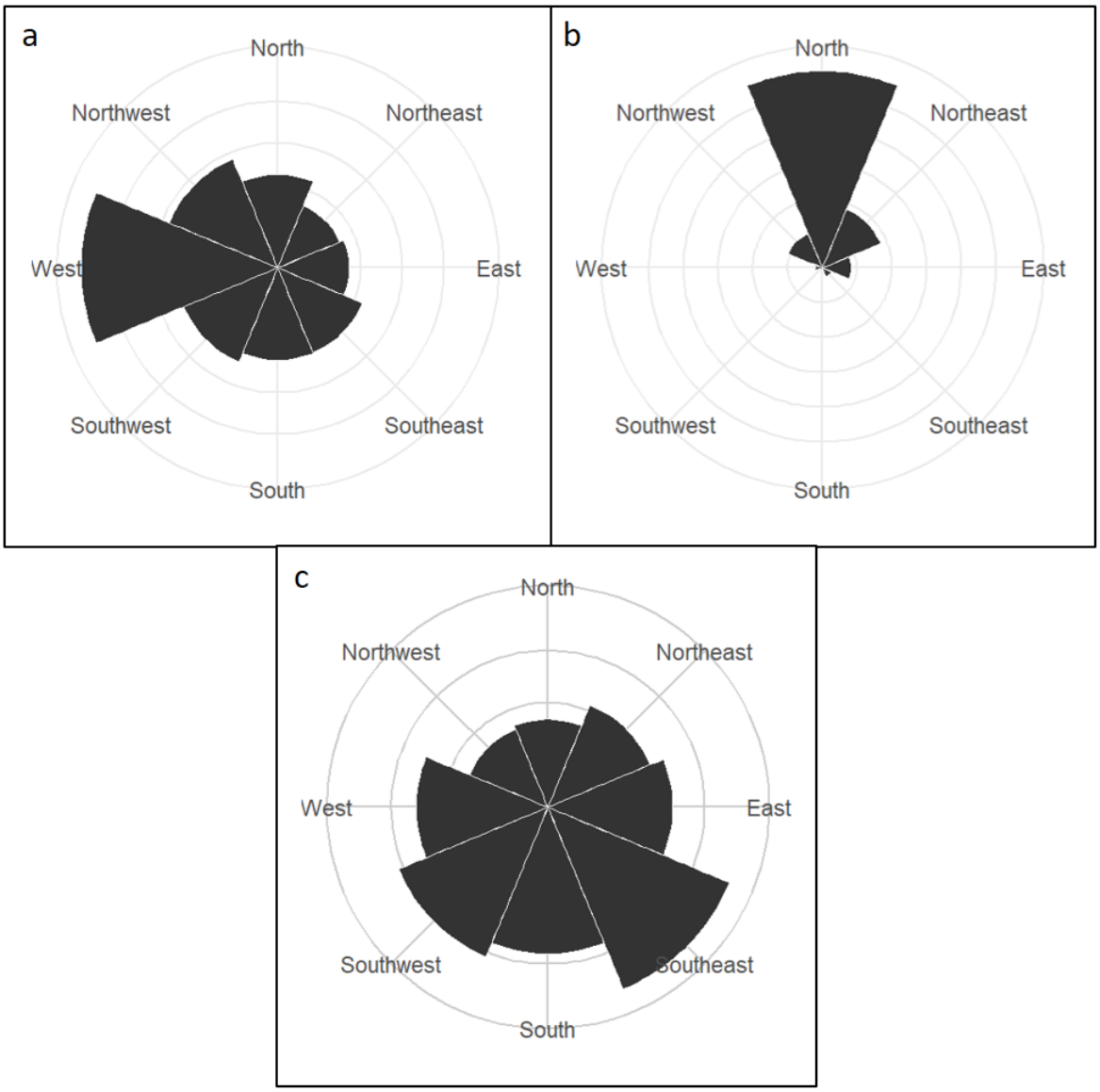

Figure 4.4. Radial plots of the topographic aspect of points within (a) thermokarst lake, (b) landslide and (c) pingo polygons.

Table 4.3 shows the results of an average nearest neighbour analysis on the landform points within the Dawson City study area. Nearest neighbour ratios < 1 indicate spatial clustering. As such, these results indicate that each landform type exhibits some level of spatial clustering. This means that individual landforms are more likely to be found near other landforms of the same type. This corroborates the observation from Holmes et al. (1968) that pingos in the Yukon-Tanana Uplands commonly occur in clusters. Thermokarst lakes are the most strongly clustered, while pingos are the least.

Table 4.3. Results of average nearest neighbour analysis for each landform type within the Dawson City study area.

Landform Type	Observed Mean Distance	Expected Mean Distance	Nearest Neighbour Ratio	z-score	p-value
Thermokarst Lakes	3017.1	8644.1	0.3490	-6.2267	0.0000
Landslides	3500.7	6000.8	0.5834	-4.1415	0.0000
Pingos	2428.9	3697.2	0.6569	-7.9022	0.0000

4.3 Thermokarst Landform Morphometry

4.3.1 Thaw Lakes

The morphometry of the 25 thermokarst lakes mapped by the YGS in the Dawson City study area is presented in Figure 4.5. The area of lakes ranges from 931 to 204 596 m^2, perimeter ranges from 138 to 2092 m, circularity ranges from 0.20 to 0.92, and elongation ranges from 1.04 to 4.65. Lake area is highly positively skewed, showing that small lakes are much more prevalent than large lakes. Perimeter, accordingly, is also positively skewed, as these metrics are positively correlated with one another. Circularity is somewhat negatively skewed and elongation is positively skewed. This shows that, while thermokarst lake shape is diverse in the Dawson City study area, circular lakes tend to be more common than elongated ones.

Niu et al. (2014) report the morphology of 2163 thermokarst lakes on the Qinghai-Tibet Plateau and Morgenstern et al. (2008) report the morphology of 2327 thermokarst lakes in the Lena River delta. Table 4.4 shows a comparison of those lakes to the 25 lakes in this study. There is a large disparity in lake size between the studies: the lakes in the Dawson City study area are, on average, one order of magnitude larger than those on the Qinghai-Tibet Plateau and one order of magnitude smaller than those in the Lena Delta. This is most likely due to differences in surficial material: the Qinghai-Tibet Plateau contains mixed sediments, though the majority is sand, while the Lena Delta contains

higher quantities of ice-rich silts. The lakes in the Dawson City study area are more similar in shape to those in the Qinghai-Tibet Plateau, rather than the less circular, more elongated lakes in the Lena Delta. In the Lena Delta, lakes were found to be more circular in areas with more silt.

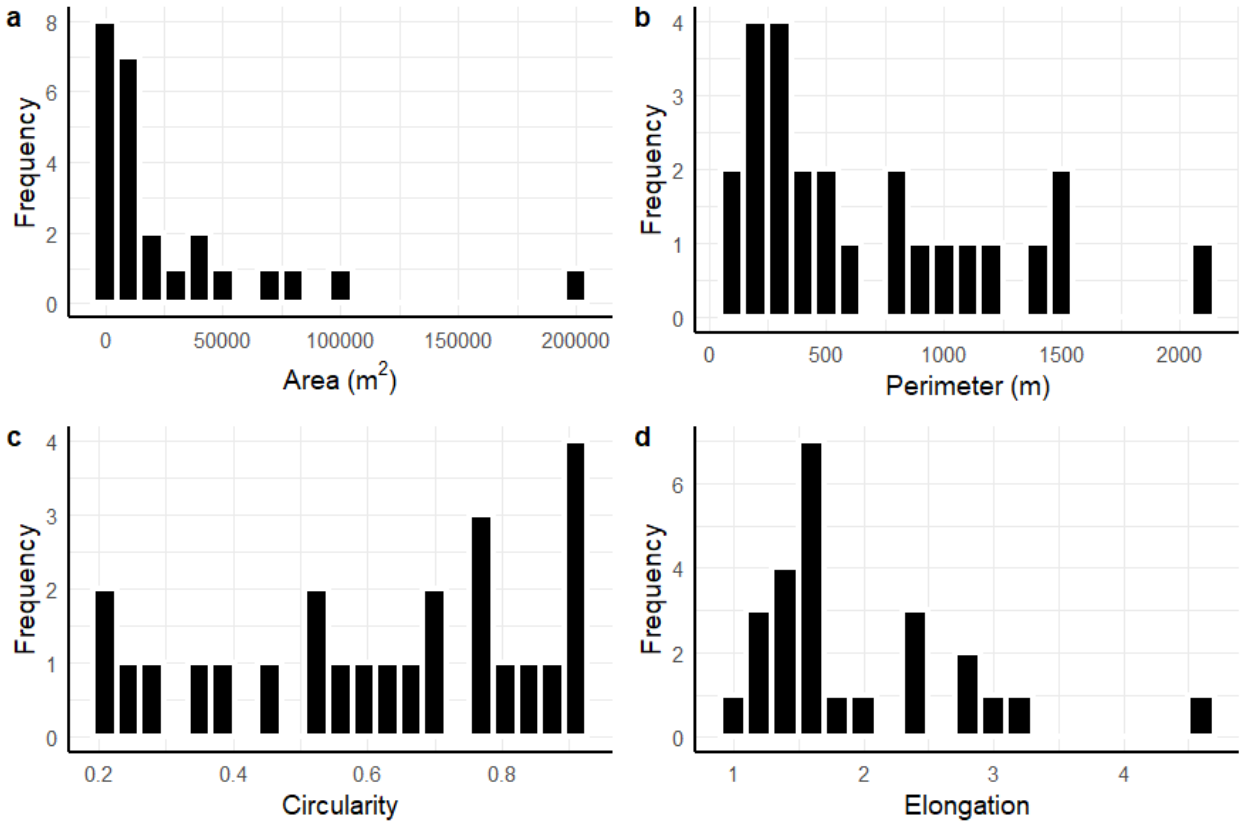

Figure 4.5. Histograms of area (a), perimeter (b), circularity index (c) and elongation index (d) of thermokarst lakes mapped by the YGS in the Dawson City study area.

Table 4.4. Thaw lake metrics from this study and other thermokarst lake morphometry projects in the Qinghai-Tibet engineering corridor (Niu et al., 2014) and the Lena Delta (Morgenstern et al., 2008).

Metric	This study	Qinghai-Tibet	Lena Delta
Number of Lakes	25	2163	2327
Area (m2)	28 644	5039	697 579
Perimeter (m)	685	349	not reported
Circularity Index (0 – 1)	0.62	0.65	0.31
Elongation Index (0 - ∞)	1.96	1.24	2.11

4.3.2 Landslides

The morphometry of the 13 landslides with visible scarps and scars mapped by the YGS in the Dawson City study area is presented in Figure 4.6. The area of landslides in the Dawson City study area ranges from 14 326 to 910 403 m^2, length from 92 to 1089 m, width from 195 to 1248 m, height from 11 to 362 m and Fahrböschung between 0.09 and 0.41. The landslides have a mean area of 400 833 m^2, a mean length of 650 m, a mean width of 693 m, a mean height of 142 m and a mean Fahrböschung of 0.21. All of these metrics have an approximately normal distribution, with slight skewness in area, centreline length and average width. Landslide area is slightly positively skewed, with more small landslides than large ones. This implies that large landslides are uncommon in the area, but this is slightly misleading, since Moosehide Slide, the largest landslide in the Dawson City study area, was not mapped by the YGS and therefore is not represented in these data. Centreline length is negatively skewed, with longer landslides being more common than shorter ones. Average width is slightly positively skewed, with more narrow or constrained landslides than wide, unconstrained ones. It is important to note that one north-facing slope on the edge of a glaciofluvial terrace between the Klondike River and the Klondike Highway has six contiguous landslides mapped on it. While these were individual events, this entire slope could be considered to be one unit, and doing so would significantly alter the distribution of these metrics in favor of large, wide landslides.

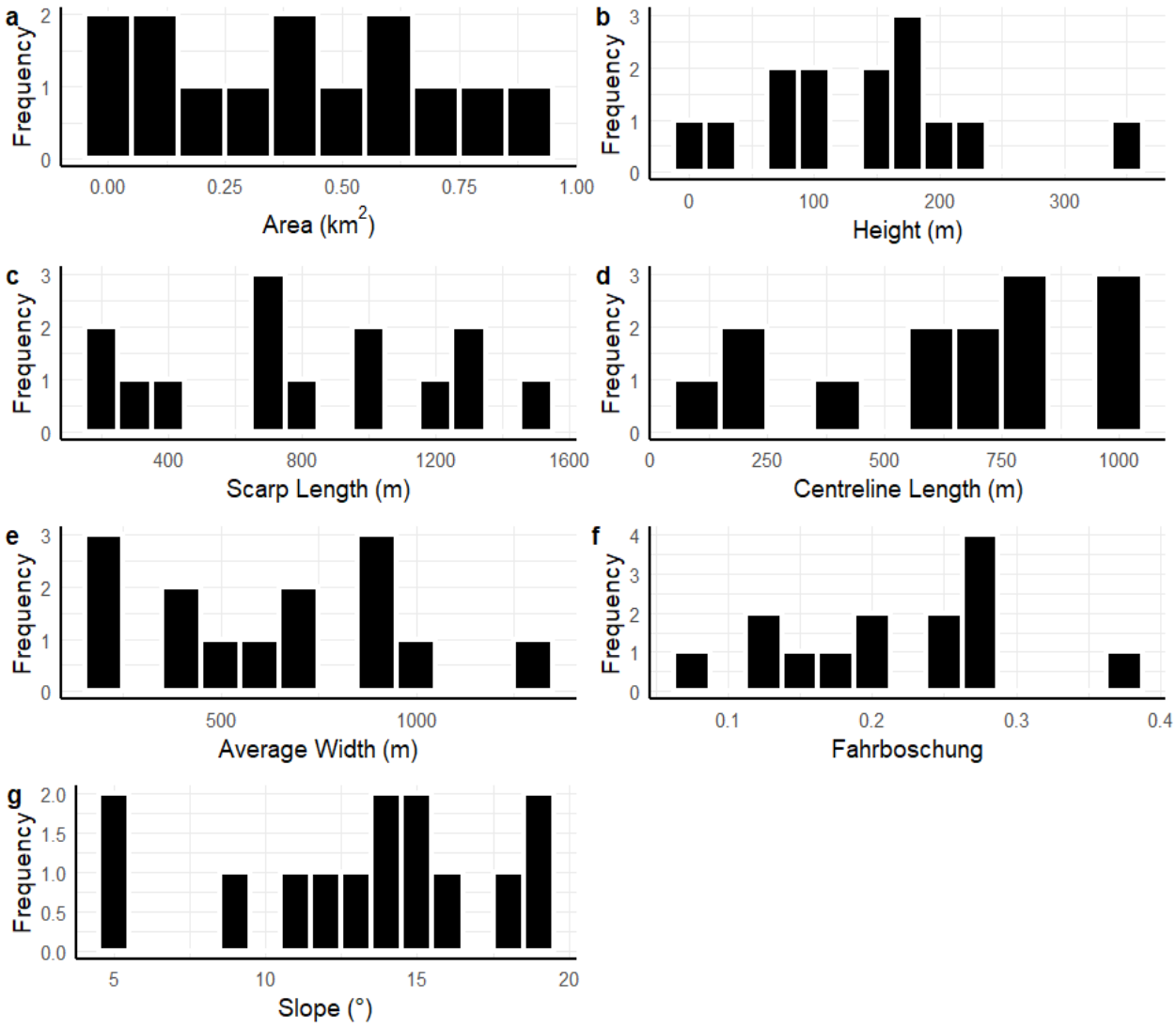

Figure 4.6. Histograms of area (a), height (b), scarp length (c), centreline length (d), average width (e), Fahrböschung (f) and slope (g) of landslides mapped by the YGS in the Dawson City study area.

4.3.3 Pingos

The 93 pingos mapped by the YGS in the Dawson City study area have a mean height of 18.6 m, a mean slope of 9.5°, and a mean diameter of 131 m. Heights range between 3 and 49 m, diameters between 57 and 256 m and average slopes between 2 and 20°. Histograms of these metrics are presented in Figure 4.7.

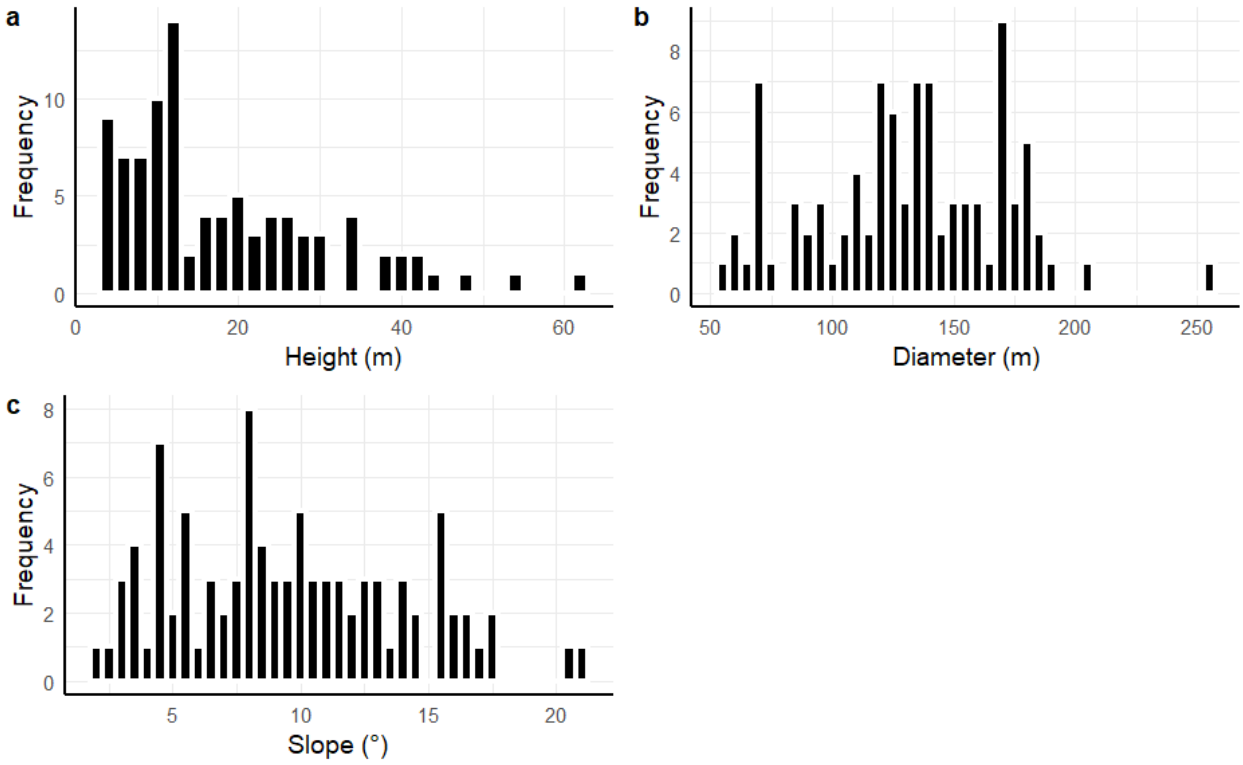

Figure 4.7. Histograms of height (a), diameter (b) and average slope (c) of pingos mapped by the YGS in the Dawson City study area.

Classification of their morphometry according to Jones et al. (2012) is presented in Table 4.5, as well as comparison to values from two other pingo morphometry studies. The majority of pingos in the Dawson City study area are tall, medium in diameter and have gentle slopes. This differs from the pingos in the other studies, which are on average short, small in diameter and have gentle slopes. In contrast to other regions, there is a higher proportion of tall pingos in the Dawson City study area, and there is a higher proportion of medium rather than small diameter pingos. There is also a higher proportion of pingos with moderate slopes in this study than in the other studies, though the proportion of steep slopes is the same.

Table 4.5. Pingo metrics from this and other studies in the Alaskan western Arctic (Jones et al., 2012) and Western Canadian Arctic (Wolfe et al., 2023), adapted from Wolfe et al. (2023), using classifications from Jones et al. (2012). Radii reported in Wolfe et al. (2023) were converted to diameters.

Metric	Classification and frequency (%)			Study Region
Height (m)	**2–5 (short)**	**5–10 (medium)**	**> 10 (tall)**	
	862 (69 %)	328 (26 %)	57 (5 %)	Alaskan western Arctic
	760 (50 %)	501 (33 %)	272 (18 %)	Western Canadian Arctic
	7 (10 %)	15 (21 %)	49 (69 %)	This study
Diameter (m)	**< 100 (small)**	**100–200 (medium)**	**> 200 (large)**	
	760 (61 %)	445 (36 %)	42 (3 %)	Alaskan western Arctic
	814 (53 %)	661 (43 %)	58 (4 %)	Western Canadian Arctic
	18 (25 %)	51 (72 %)	2 (3 %)	This study
Slope (°)	**< 15 (gentle)**	**15–30 (moderate)**	**> 30 (steep)**	
	1246 (99.9 %)	1 (0.1 %)	0 (0 %)	Alaskan western Arctic
	1499 (98 %)	33 (2 %)	1 (0.07 %)	Western Canadian Arctic
	62 (87 %)	9 (13 %)	0 (0 %)	This study

4.4 GLMs of Thermokarst Susceptibility

The results of the null, univariate and multivariate GLMs of thermokarst lake, landslide and pingo susceptibility are shown in the following subsections. The application of the optimal models to Yukon and their validation is described in Section 4.4.

4.4.1 Lakes

The results of the null and univariate GLMs of thermokarst lake susceptibility are shown in Table 4.6. Slope is the strongest predictor, as shown by the low AIC value (2837.2) and high $\Delta D/\Delta df$ (733.8). With a coefficient of -0.88, the relationship is inverse, meaning that lakes are more likely to be found in areas with low slopes. The next best predictors are elevation, aspect, PRR_{FSS} and permafrost presence. Elevation has an inverse relationship to lake presence, but it is not ideal as a predictor variable for this modelling study, as elevation ranges cannot be compared to one another between regions and the model is only optimized for the elevation range of the Dawson City study area. Only the Flat and West aspect classes were significant at any confidence level, both with direct relationships, and multicollinearity exists between slope and the flat aspect class. PRR_{FSS}

and permafrost presence both have direct relationships, meaning that lakes are more likely to be found in places that receive more solar radiation and that have more permafrost. PRR and permafrost presence were combined with slope in multivariate models, and the results are presented in Table 4.7. Permafrost presence is not statistically significant when combined with slope presence, and its relationship to thermokarst lake presence changed from direct to inverse. Both of these models have roughly half the ΔD/Δdf of the univariate slope model. Hence, the univariate model using slope was retained as the optimal model of thermokarst lake susceptibility.

Table 4.6. Statistical results for null and univariate GLM of thermokarst lake susceptibility. Subsequent levels of categorical variables are indented after the first level. Significance at the 95, 99 and 99.9 % confidence intervals is indicated by the symbols '*', '**' and '***' respectively.

Variable	Significance	Coefficient	Intercept	AIC	p-value	df	ΔD/Δdf
Null Model	***		-8.91	3569.0	≤ 0.001	1	3567
Elevation	***	-0.02	0.7	3163.5	≤ 0.001	1	407.5
Slope	***	**-0.88**	**-5.45**	**2837.2**	**≤ 0.001**	**1**	**733.8**
$Aspect_{Flat}$	***	4.41	-10.87	3056.3	≤ 0.001	8	66.1
$Aspect_{Northeast}$		-0.18			0.825		
$Aspect_{East}$		-0.39			0.671		
$Aspect_{Southeast}$	*	1.37			0.037		
$Aspect_{South}$		0.98			0.154		
$Aspect_{Southwest}$		-0.05			0.953		
$Aspect_{West}$	***	2.24			≤ 0.001		
$Aspect_{Northwest}$		-0.41			0.656		
$Curvature_{Profile}$		-131.54	-8.92	3568.3	0.093	1	2.7
$Curvature_{Planform}$		-117.33	-8.91	3568.7	0.118	1	2.3
$Curvature_{Mean}$		-180.87	-8.92	3567.4	0.052	1	3.6
PRR_{CSS}	***	0.05	-12.21	3542.5	≤ 0.001	1	28.5
PRR_{FSS}	***	5.99	-12.79	3522.4	≤ 0.001	1	48.6
Fines	*	0.01	-14.23	3566.8	0.043	1	4.2
Soil $Texture_1$		13.92	-22.57	3567.0	0.96	3	2.7
Soil $Texture_2$		13.66			0.96		
Soil $Texture_3$		-0.00			1		
Permafrost	***	11.18	-17.18	3524.2	≤ 0.001	1	46.8
Air Temperature	***	3.38	3.38	3517.0	≤ 0.001	1	54
Segregated Ice		-13.68	-8.88	3562.3	0.96	1	8.7

Table 4.7. Statistical results for multivariate GLMs of thermokarst lake susceptibility. Additional predictor variables are indented after the first. Significance at the 95, 99 and 99.9 % confidence intervals is indicated by the symbols '*', '**' and '***' respectively.

Variable	Significance	Coefficient	Intercept	AIC	p-value	df	ΔD/Δdf
Slope	***	-0.83	-10.94	2817.7	≤ 0.001	2	377.7
PRR_{FSS}	***	8.17			≤ 0.001		
Slope	***	-0.90	-3.75	2837.9	≤ 0.001	2	367.5
Permafrost		-2.22			0.25		

The optimal model of thermokarst lake susceptibility is shown mapped in the Dawson City study area in Figure 4.8. The upper limits of the Low, Medium and High classes are absolute susceptibilities of 0.001, 0.003 and 0.004 respectively. The majority of the study area is within the Low susceptibility class (yellow), while the Medium (orange) and High (red) classes are restricted to the floodplains of the Yukon, Klondike, Sixty mile and Indian Rivers, as well as in glaciofluvial terraces in the east, all of which are areas with low topographic slopes.

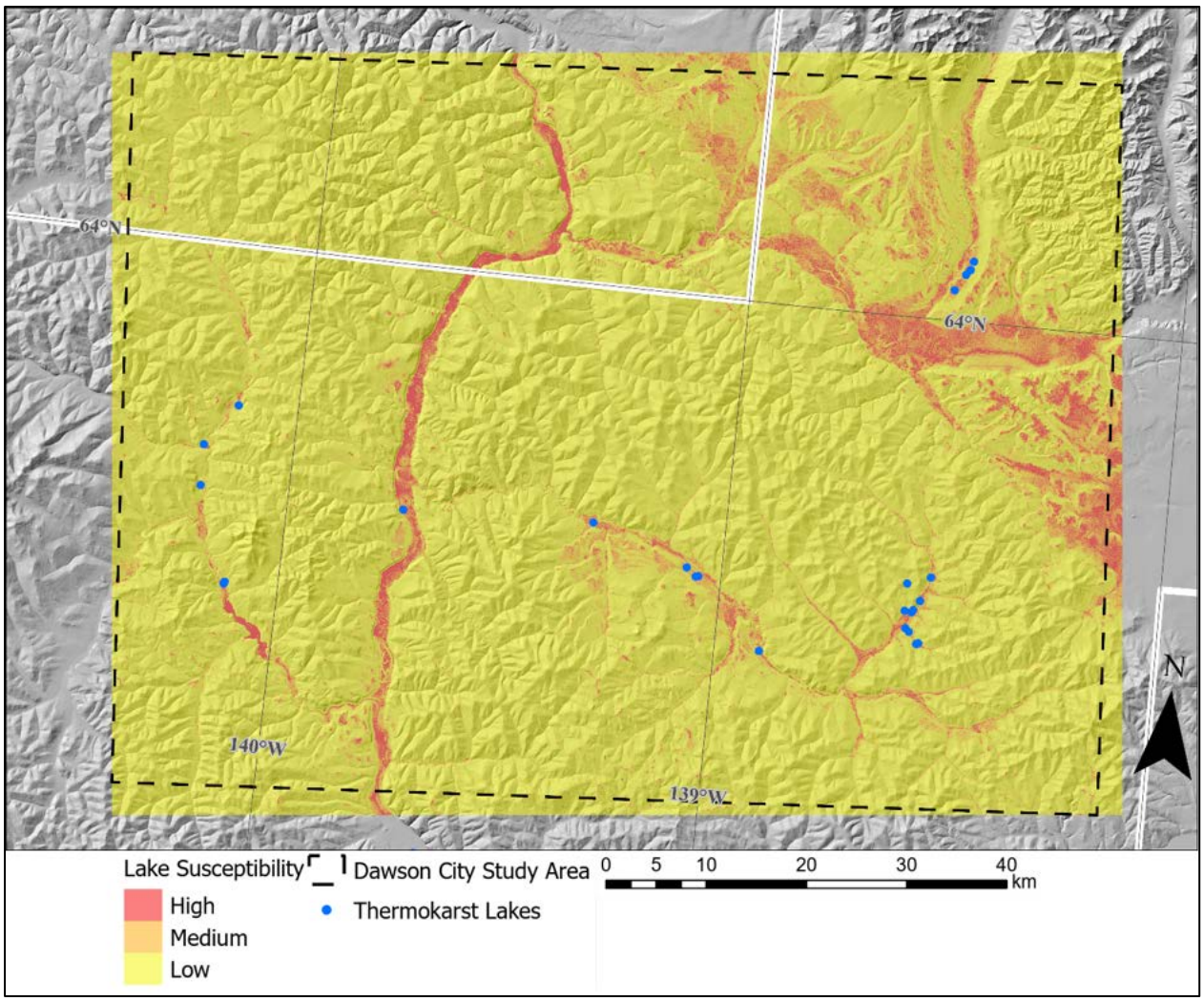

Figure 4.8. Thermokarst lake susceptibility in the Dawson City study area, where High, Medium and Low are classified using the Jenks natural breaks method. Thermokarst lakes mapped by the YGS are shown in blue, and the unmapped area is delineated in white.

4.4.2 Landslides

The results of the null and univariate GLMs of landslide susceptibility are shown in Table 4.8. As for lakes, slope is the strongest predictor, with an AIC value of 32 699 and a $\Delta D/\Delta df$ of 14 686. With a coefficient of 0.25, there is a direct relationship between slope and landslide susceptibility. The next best predictors are PRR_{CSS}, soil texture, elevation and air temperature. Solar radiation has an inverse relationship to landslide susceptibility, a relationship also seen by the positive coefficients of the north and northwest aspect

classes. Soil texture has a direct relationship with landslide susceptibility, meaning that landslides are more likely to occur in locations with frost susceptible sediments.

PRR_{CSS} and soil texture were combined additively with slope in multivariate models and are presented in Table 4.9. Elevation was excluded as a predictor variable for the same reason as described in Subsection 4.3.1, and air temperature was excluded because the ERA5 data (Hersbach et al., 2020) has too low a spatial resolution to be practical for these modelling purposes. There are only 35 ERA5 raster cells within the Dawson City study area, hence a maximum of 35 temperature values in the model.

Table 4.9 shows that both PRR_{CSS} and soil texture were significant when combined with slope, but both multivariate models had a $\Delta D/\Delta df$ roughly half that of slope alone. Hence, the univariate model using slope was retained as the optimal model of landslide susceptibility.

Table 4.8. Statistical results for null and univariate GLM models of landslide susceptibility. Subsequent levels of categorical variables are indented after the first level. Significance at the 95, 99 and 99.9 % confidence intervals is indicated by the symbols '*', '**' and '***' respectively.

Variable	Significance	Coefficient	Intercept	AIC	p-value	df	ΔD/Δdf
Null Model	***		-1.05	47383	< 0.001	1	47381
Elevation	***	0.01	-5.45	42984	< 0.001	1	4401
Slope	***	**0.25**	**-2.61**	**32699**	**< 0.001**	**1**	**14686**
$Aspect_{North}$	***	0.76	-3.32	36054	< 0.001	8	742
$Aspect_{Northeast}$	***	-0.13			< 0.001		
$Aspect_{East}$	***	-0.57			< 0.001		
$Aspect_{Southeast}$	***	-0.50			< 0.001		
$Aspect_{South}$	***	-0.09			< 0.001		
$Aspect_{Southwest}$	***	0.23			< 0.001		
$Aspect_{West}$	*	0.05			0.012		
$Aspect_{Northwest}$	***	0.44			< 0.001		
$Curvature_{Profile}$		-29.73	-1.05	47381	0.052	1	4
$Curvature_{Planform}$	***	-17.10	-1.05	47276	< 0.001	1	109
$Curvature_{Mean}$	***	-25.19	-1.06	47179	< 0.001	1	206
PRR_{CSS}	***	-0.14	8.61	40148	< 0.001	1	7237
PRR_{FSS}	***	-11.01	5.83	42861	< 0.001	1	4524
Fines	***	0.00	-4.48	39384	< 0.001	1	345
Soil $Texture_{1}$	***	1.33	-4.50	40053	< 0.001	2	4573
Soil $Texture_{2}$	***	1.81			< 0.001		
Permafrost	***	7.05	-6.33	46930	< 0.001	1	455
Air Temperature	***	16.33	53.82	43049	< 0.001	1	4336
Segregated Ice	***	0.97	-1.24	46191	< 0.001	1	1194

Table 4.9. Statistical results for multivariate GLMs of landslide susceptibility. Additional predictor variables are indented after the first. Significance at the 95, 99 and 99.9 % confidence intervals is indicated by the symbols '*', '**' and '***' respectively.

Variable	Significance	Coefficient	Intercept	AIC	p-value	df	ΔD/Δdf
Slope	***	0.23	3.62	31219	< 0.001	2	8084
PRR_{CSS}	***	-0.09			< 0.001		
Slope	***	0.27	-5.13	28235	< 0.001	3	6384.7
Soil Texture1	***	2.85			< 0.001		
Soil Texture2	***	3.37			< 0.001		

The mapped result of the optimal model of landslide susceptibility is shown in Figure 4.9 for the Dawson City study area. The upper limits of the Low, Medium and High classes are absolute susceptibility values of 0.527, 0.586 and 0.621 respectively. While the relationship between the predictor (slope) and response variables (susceptibility) is inverse, Figure 4.9 is not simply the inverse of the map of lake susceptibility (Figure 4.8), where the relationship is direct. Both the differences in the absolute and relative values of the estimate and the intercept, as well as the differences in the landscape distribution of high and low slopes, and the natural breaks separating the susceptibility classes, result in a different spatial distribution of high and low susceptibility. High susceptibility areas are limited to the slopes of the mountains and at the edge of the floodplains of the major rivers. Notably, the Ogilvie Mountains in the northwest of the study area are steeper than those of the Klondike Plateau, resulting in more High susceptibility areas there.

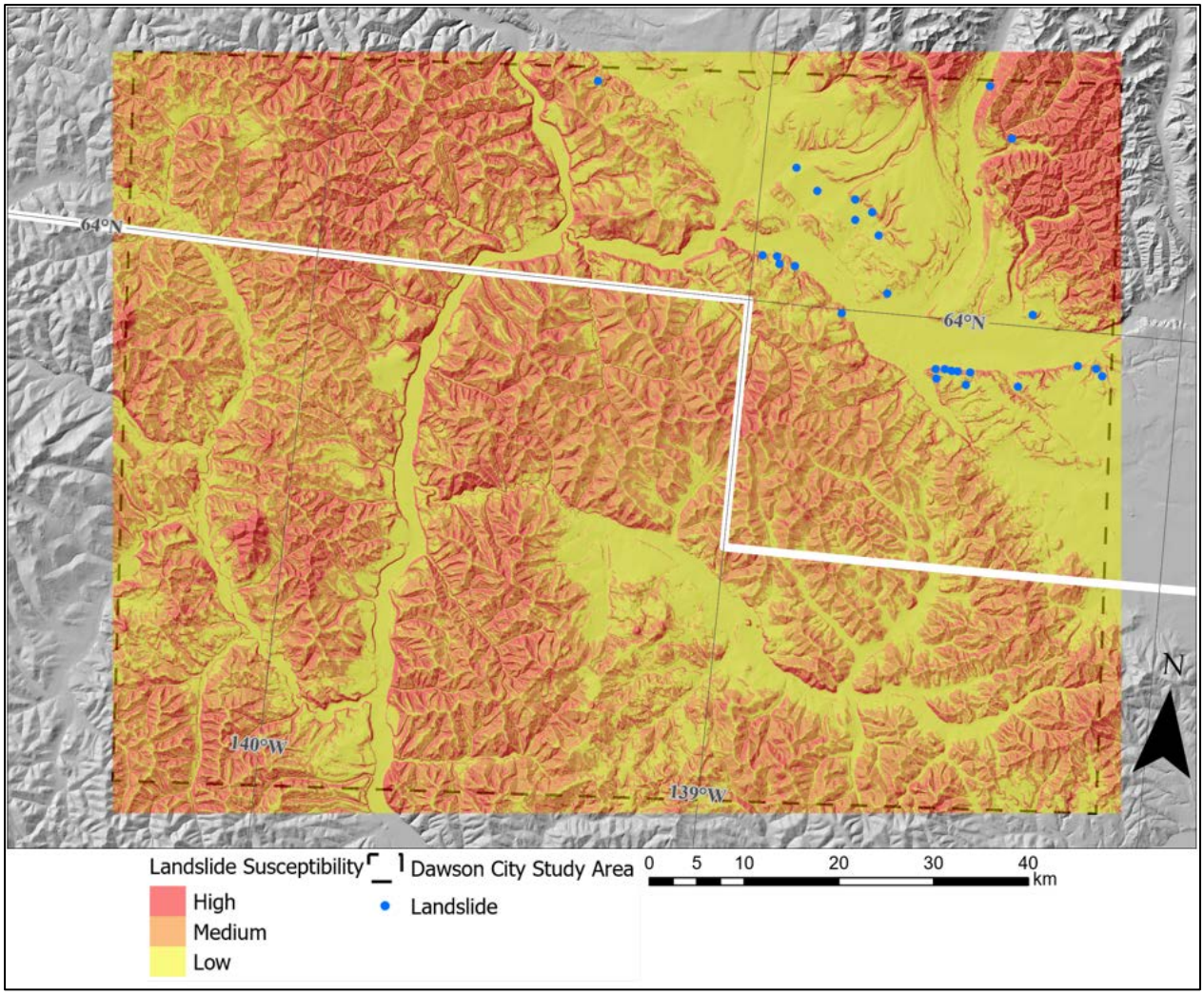

Figure 4.9. Landslide susceptibility in the Dawson City study area, where High, Medium and Low are classified using the Jenks natural breaks method. Landslides mapped by the YGS are shown in blue, and the unmapped area is delineated in white.

4.4.3 Pingos

Both Holmes et al. (1968) and Hughes (1969) observed that the open-system pingos of the unglaciated Yukon-Tanana Uplands and Klondike Plateau occurred predominantly on south and east aspects, and at the "break-in-slope" between valley walls and floors. The results of the null and univariate pingo susceptibility models are shown in Table 4.10, and agree with both of these observations. Profile curvature is the strongest predictor, as shown by the low AIC value (4848.9) and high $\Delta D/\Delta df$ (64.6). With a coefficient of -290.83, the relationship is inverse, meaning that pingos are more likely to form at points in the

landscape where topographic curvature perpendicular to the contour lines is concave (the breaks-in-slope mentioned above). The next best predictor is PRR_{CSS}, which has a direct relationship to pingo presence. While soil texture also has a relatively high $\Delta D/\Delta df$ (19.4), none of the classes of this variable are significant at any confidence level. While the east, south and southwest aspect classes have positive coefficients, agreeing with the observations of Holmes et al. (1968) and Hughes (1969), aspect has a relatively low $\Delta D/\Delta df$ (8.0). These aspects classes are multicollinear with PRR.

Profile curvature and PRR_{CSS} were combined in a multivariate model, and the results are presented in Table 4.11. The coefficients in the multivariate model are very similar to the coefficients of the same variables in the univariate models, but the $\Delta D/\Delta df$ of this model is less than that of the best univariate model. Hence, profile curvature was retained as the only predictor variable in the optimal model of pingo susceptibility.

The optimal model of pingo susceptibility is shown mapped in the Dawson City study area in Figure 4.10. The upper limits of the Low, Medium and High classes are absolute susceptibilities of 0.0003, 0.001 and 0.04 respectively. The majority of the study area is within the Low susceptibility class (yellow), while the Medium (orange) and High (red) classes are restricted to incised valley bottoms and the edges of floodplains.

Table 4.10. Statistical results for null and univariate GLM models of pingo susceptibility. Subsequent levels of categorical variables are indented after the first level. Significance at the 95, 99 and 99.9 % confidence intervals is indicated by the symbols '*', '**' and '***' respectively.

Variable	Significance	Coefficient	Intercept	AIC	p-value	df	ΔD/Δdf
Null Model	***		-8.55	4911.5	< 0.001	1	
Elevation	*	-0.00	-8.01	4908.2	0.02	1	5.3
Slope		-0.00	-8.49	4913.2	0.57	1	0.3
$Aspect_{Flat}$	*	0.73	-9.15	4863.5	0.05	8	8.0
$Aspect_{North}$		0.23			0.48		
$Aspect_{Northeast}$		0.38			0.23		
$Aspect_{East}$	**	0.74			0.01		
$Aspect_{Southeast}$		0.37			0.25		
$Aspect_{South}$	***	1.36			< 0.001		
$Aspect_{Southwest}$	***	0.90			< 0.001		
$Aspect_{West}$		-0.40			0.32		
$Curvature_{Profile}$	*******	**-290.83**	**-8.67**	**4848.9**	**< 0.001**	**1**	**64.6**
$Curvature_{Planform}$	***	-169.99	-8.57	4898.6	< 0.001	1	14.9
$Curvature_{Mean}$	***	-236.22	-8.61	4881.2	< 0.001	1	32.3
PRR_{CSS}	***	0.03	-10.32	4872.3	< 0.001	1	41.2
PRR_{FSS}	***	2.71	-10.21	4873.1	< 0.001	1	40.4
Fines	*	0.00	-10.02	4905.0	0.02	1	8.5
Soil $Texture_1$		-0.00	-23.57	4878.7	0.97	2	19.4
Soil $Texture_2$		15.09			1.00		
Soil $Texture_3$		-0.00			0.98		
Permafrost		1.15	-9.46	4911.3	0.15	1	2.2
Air Temperature		-0.26	-9.61	4913.2	0.56	1	0.3
Segregated Ice		0.36	-8.57	4911.7	0.16	1	1.8

Table 4.11. Statistical results of multivariate GLM of pingo susceptibility.

Variable	Significance	Coefficient	Intercept	AIC	p-value	df	ΔD/Δdf
$Curvature_{Profile}$	***	-302.62	-10.46	4809	< 0.001	2	53.2
PRR_{CSS}	***	0.03			< 0.001		

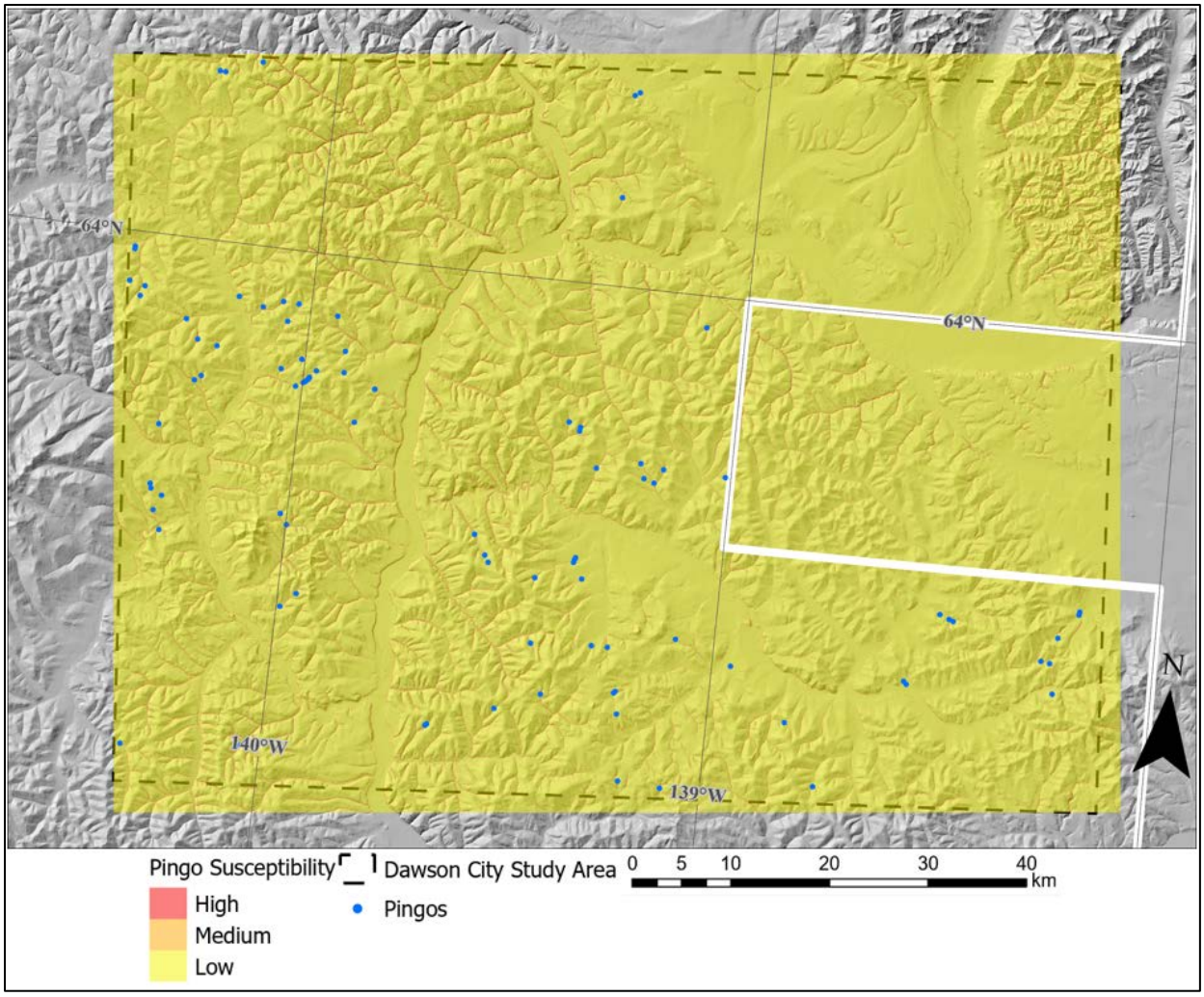

Figure 4.10. Pingo susceptibility in Dawson City study area, where High, Medium and Low are classified using the Jenks natural breaks method. Pingos mapped by the YGS are shown in blue, and the unmapped area is delineated in white.

4.5 GLM Validation

Landform susceptibility models from the Dawson City study area were applied to the entirety of Yukon, and their ability to predict YGS landform points was evaluated. The distribution of susceptibility values at these points, as well as at equal numbers of randomly distributed points that were generated for each of the three thermokarst landform types is presented in the following subsections. The susceptibility classification

of points within Yukon's distinct ecoregions (Yukon Ecoregions Working Group, 2004a) was assessed to better understand the spatial variability in the model performance.

4.5.1 Lakes

Thermokarst lake susceptibility in Yukon is shown in Figure 4.11. Due to Yukon's generally rugged terrain, areas of high thermokarst lake susceptibility are mainly confined to valley bottoms. Other areas of high susceptibility include the Tintina Trench and the Old Crow Flats in the north of the territory. Approximately 86 % of the territory is in the Low susceptibility class, 11 % is in the Medium class, and 3 % is in the High class. Figure 4.12 shows four locations in more detail. Tombstone Territorial Park and the confluence of the Blackstone River and its tributary, the East Blackstone River, are shown in panel (a). In this area, while some lakes are in medium susceptibility areas, many are within low susceptibility areas. These lakes are at low elevations in the landscape and are adjacent to slight slopes. The Pelly Mountains, with Little Salmon and Drury Lakes visible as the elongated medium and high susceptibility areas are shown in panel (b). The model performs the worst here, as most of the lakes are very small, isolated, and in upland valleys. The St. Elias Mountains, with the Alaska Highway running diagonally through the map frame and the Donjek River runs from North to South is shown in panel (c). The model performs very well here, with multiple clusters of lakes in high susceptibility areas. An artifact from the CDEM is visible across the top of this map as a line following the 68°N parallel. It is assumed that the data source used by the CDEM differs here. The Selwyn Mountains, east of the community of Ross River, are shown in panel (d). This is a relatively low-relief area, with lakes being less clustered here than in more mountainous areas. The model performs relatively well here, with most lakes being in medium susceptibility areas.

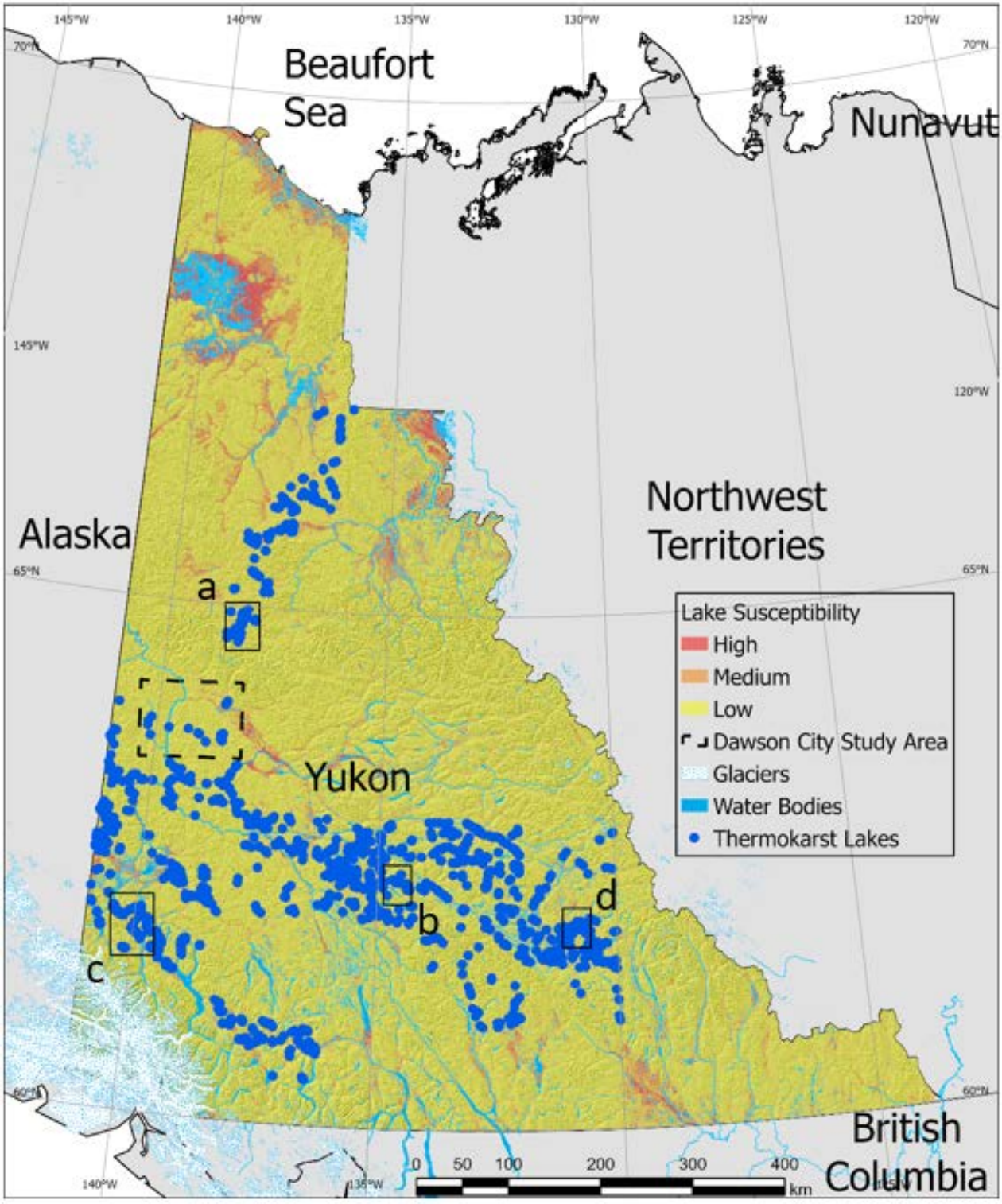

Figure 4.11. Thermokarst lake susceptibility in Yukon. High, medium and low susceptibility classes are shown. Insets a, b, c and d are shown in Figure 4.12.

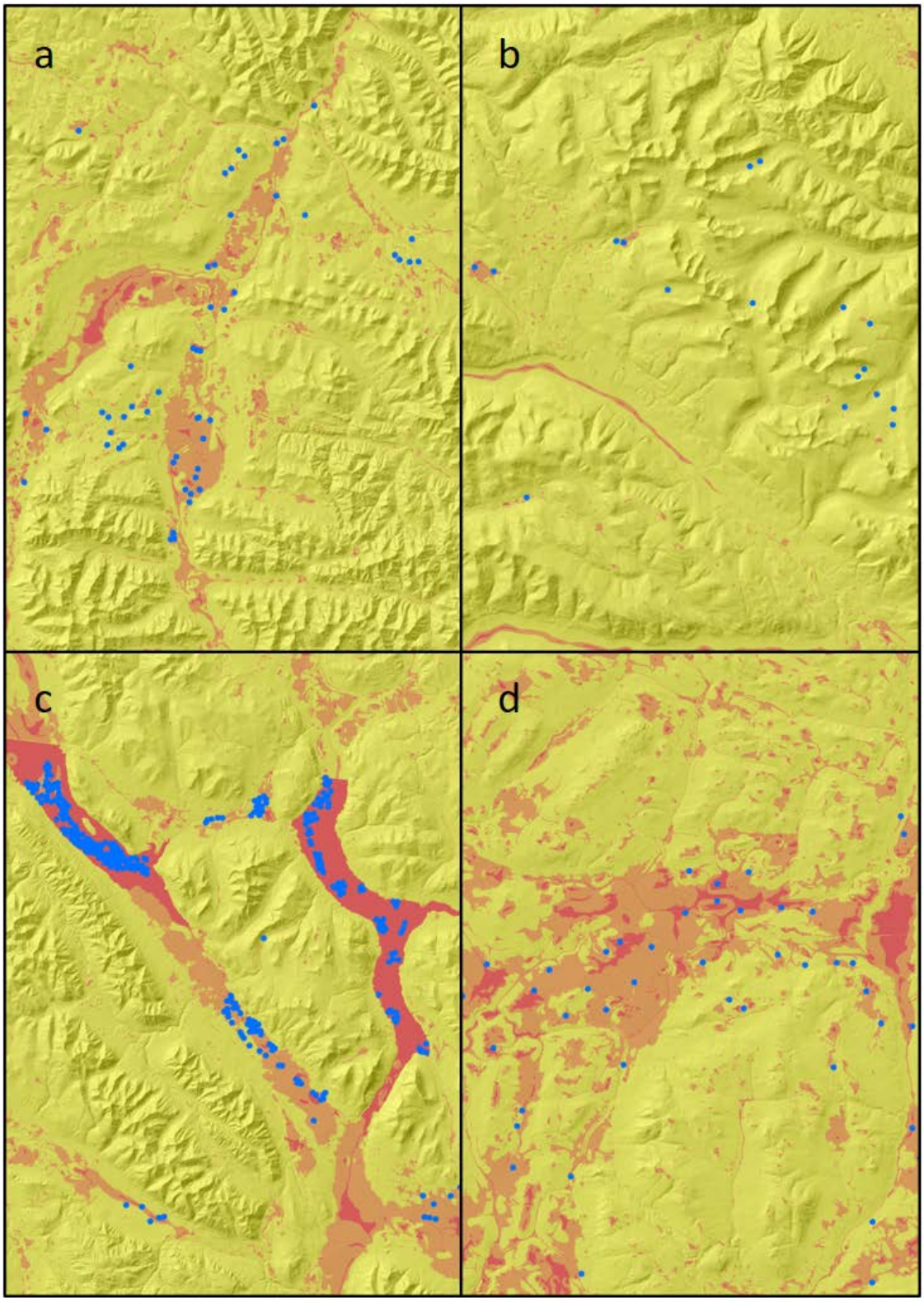

Figure 4.12. Thermokarst susceptibility and location of thermokarst lakes for insets from Figure 4.11. General regions: a) Tombstone Territorial Park and North Ogilvie Mountains; b) Pelly Mountains; c) Rub-Nisling Ranges and St. Elias Mountains; d) Yukon Plateau-North.

The distribution of modelled susceptibility values at the thermokarst lake points mapped by the YGS is shown in Figure 4.13. This, as well as the descriptive statistics shown in Table 4.12, imply that the model performs somewhat better outside of the Dawson City study area than in it. The magnitude of the susceptibility values is very low, implying that thermokarst lakes are a rare occurrence in the Dawson City study area.

Table 4.12. Descriptive statistics of modelled thermokarst lake susceptibility values.

	Minimum	**Maximum**	**Mean**	**S.D.**
Dawson	< 0.0001	0.0035	0.0012	0.0008
Yukon	< 0.0001	0.0043	0.0016	0.0013
Random A	< 0.0001	0.0043	0.0004	0.0009
Random B	< 0.0001	0.0043	0.0004	0.0008

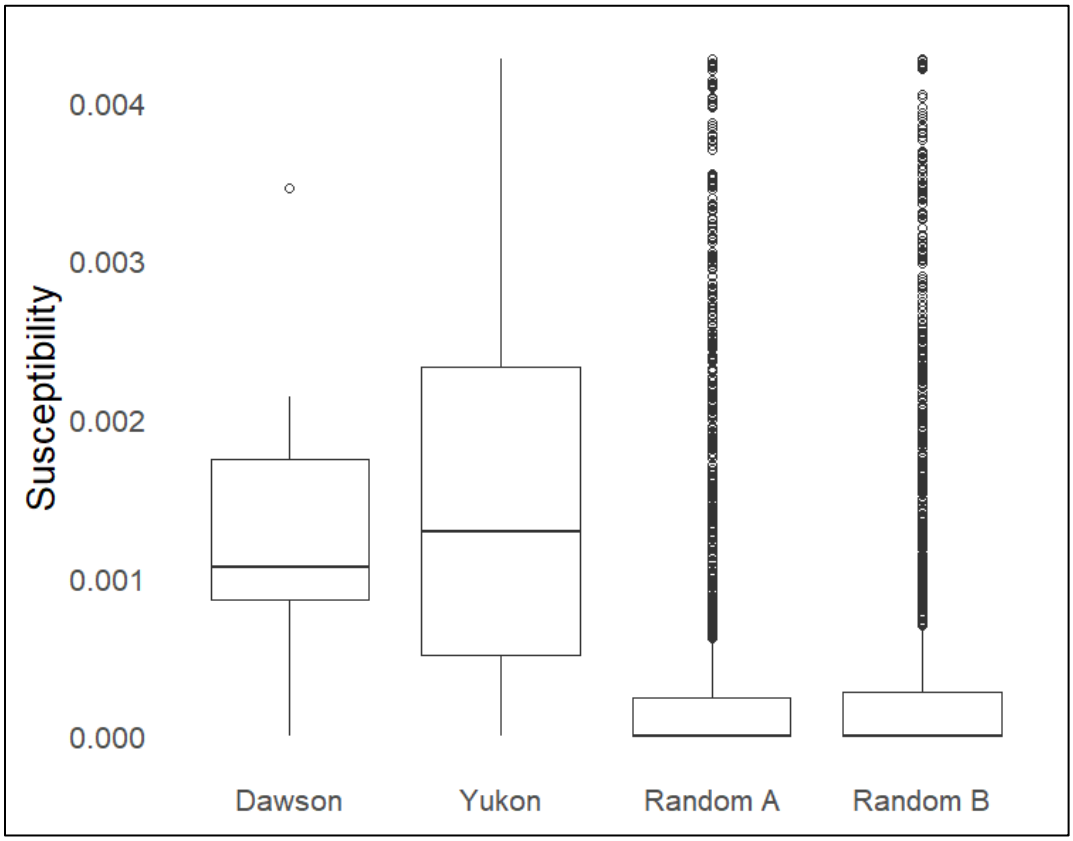

Figure 4.13. Box plot of thermokarst lake susceptibility of YGS points within the Dawson City study area (25), within Yukon (2201) and two sets of randomly generated points in Yukon (2201).

The count and percentage of the thermokarst lake points within each susceptibility class is shown in Table 4.13. A χ^2 goodness of fit test was applied to the YGS points and each of the random sets of points to determine whether or not the susceptibility values at the YGS points were significantly higher than the values at the randomly distributed points. These strongly indicate that there is a significant difference in the modelled susceptibility values of the YGS points and the random points (random points A: χ^2 value = 4514.7, p-value < 0.0001; random points B: χ^2 value = 4450.3, p-value < 0.0001), showing that the model of thermokarst lake susceptibility does a good job of predicting areas where thermokarst lakes have developed.

Table 4.13. Thermokarst lake susceptibility classification of YGS lake points within the Dawson City study area (25), within Yukon (2201) and randomly generated points in Yukon (2201).

Susceptibility Class / Sample	High	Medium	Low
YGS Dawson	2 (8 %)	18 (72 %)	5 (20 %)
YGS Yukon	629 (28.6 %)	1089 (49.5 %)	483 (21.9 %)
Random Points A	152 (6.9 %)	298 (13.5 %)	1751 (79.6 %)
Random Points B	145 (6.6 %)	313 (14.2 %)	1743 (79.2 %)

Thermokarst lakes were mapped in 13 of the 26 Yukon ecoregions. The modelled susceptibility values of the lakes within each of these is presented in Table 4.14. The majority of lakes are in the high or medium susceptibility classifications in all ecoregions except for the Pelly Mountains and Selwyn Mountains Ecoregions in southeastern Yukon. The model may perform poorly in these regions because they are climatologically or topographically distinct from the Dawson City study area. The number of points mapped per ecoregions is not necessarily indicative of the true number of lakes in an area: the mapped locations in some of the ecoregions are biased by the existence of infrastructure.

Table 4.14. Thermokarst lake susceptibility classifications of points mapped by the YGS within Yukon ecoregions.

Ecoregion \ Susceptibility Class	High	Medium	Low	Total
Klondike Plateau	113 (22.1%)	304 (59.4%)	95 (18.6%)	512
Ruby-Nisling Ranges	273 (53.4%)	135 (26.4%)	103 (20.2%)	511
Yukon Plateau-North	79 (20.8%)	224 (59.1%)	76 (20.1%)	379
Yukon Plateau-Central	26 (10.6%)	138 (56.1%)	82 (33.3%)	246
Yukon Southern Lakes	42 (27.3%)	91 (59.1%)	21 (13.6%)	154
North Ogilvie Mountains	45 (33.1%)	74 (54.4%)	17 (12.5%)	136
Eagle Plains	23 (27.1%)	30 (35.3%)	32 (37.6%)	85
Pelly Mountains	6 (7.8%)	32 (41.6%)	39 (50.6%)	77
Wellesley Lake	19 (31.1%)	38 (62.3%)	4 (6.6%)	61
St. Elias Mountains	3 (15.8%)	11 (57.9%)	5 (26.3%)	19
Selwyn Mountains	(0%)	7 (46.7%)	8 (53.3%)	15
McQuesten Highlands	(0%)	4 (100%)	(0%)	4
British-Richardson Mountains	(0%)	1 (50%)	1 (50%)	2

4.5.2 Landslides

Landslide susceptibility across Yukon is shown in Figure 4.14. All of Yukon's mountains are classified as Medium or High susceptibility. The distribution of landslides mapped by the YGS is more limited than that of thermokarst lakes. Approximately 46 % of Yukon is in the Low susceptibility class, approximately 20 % is in the Medium susceptibility class, and 34 % is in the High susceptibility class. Hence, only two locations are shown in more detail in Figure 4.15. Location (a) is in Tombstone Territorial Park in the McQuesten Highlands, very close to the Dawson City study area. The landslides here occur on steep mountain slopes, and are most likely rockslides. All of these landslides are in high

susceptibility areas, indicating that the model performs relatively well here. Location (b) is in the Pelly Mountains in south-central Yukon. The landslides here are similar to those from location (a) in their location in the landscape and their susceptibility class. Location (c) is in the Peel River Plateau in the northeast of Yukon. The topography here is distinct from the other locations; the plateau, on which lie multiple thermokarst lakes, is incised here by the Trail River. Landslide here occur on the steep slopes between the plateau and the river's floodplain, and are all retrogressive thaw slumps. Some of these thaw slumps initiated in the upper reaches of tributary streams, in areas of relatively low slope. These landslides are in low susceptibility areas, while landslides closer to the Trail River or its larger tributaries are generally in high susceptibility areas.

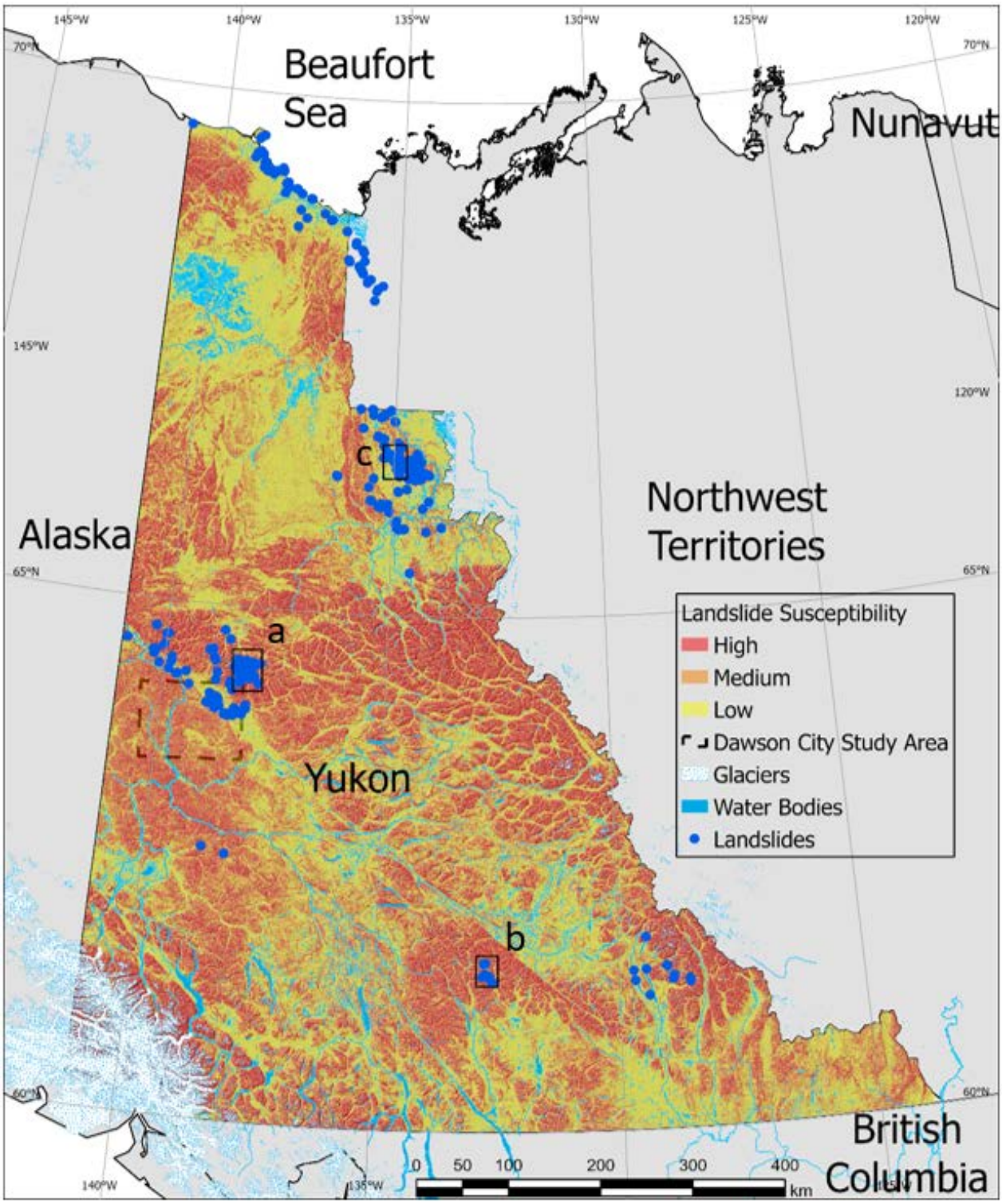

Figure 4.14. Landslide susceptibility in Yukon. High, medium and low susceptibility classes are shown. Insets a, band c are shown in Figure 4.15.

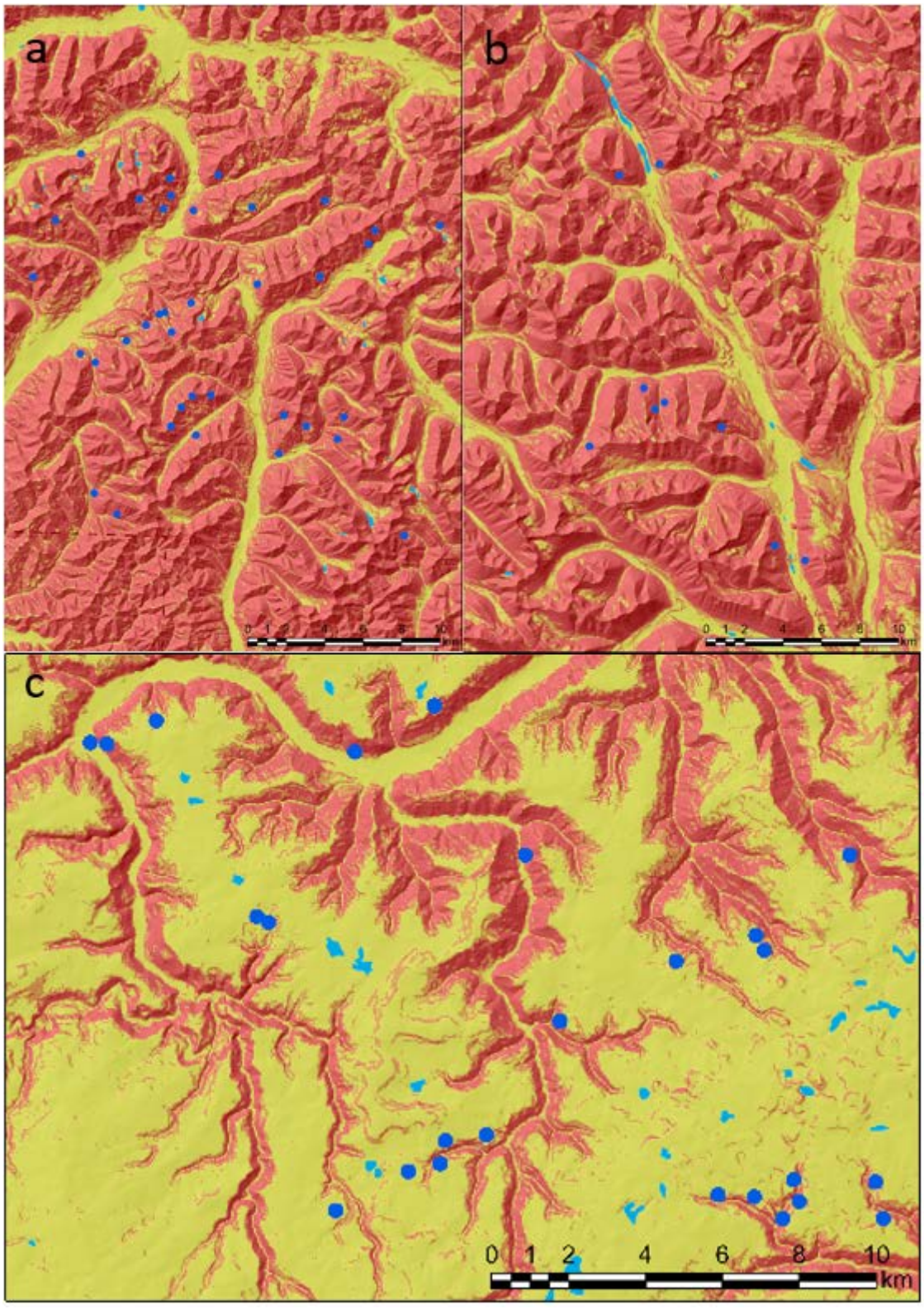

Figure 4.15. Landslide susceptibility and location of landslides for insets from Figure 4.14. General regions: a) McQuesten Highlands; b) Pelly Mountains; c) Peel River Plateau.

The distribution of modelled susceptibility values at the landslide points mapped by the YGS and at two sets of points distributed randomly across Yukon is shown in Figure 4.16. The difference between these distributions is less obvious than it is for lakes, implying that the landslide model does not perform quite as well. The descriptive statistics in Table 4.15 also show that the landslide susceptibility values are higher than the susceptibility values for lakes. This implies that landslides are a more common occurrence than thermokarst lakes in the Dawson City study area. This arises from the fact that the landform polygons used as inputs to the model are larger in size than the lake polygons. The Moosehide Slide, a large landslide on the north end of Dawson City, can also be used to assess the model's performance. The entirety of the slide is in a high susceptibility area.

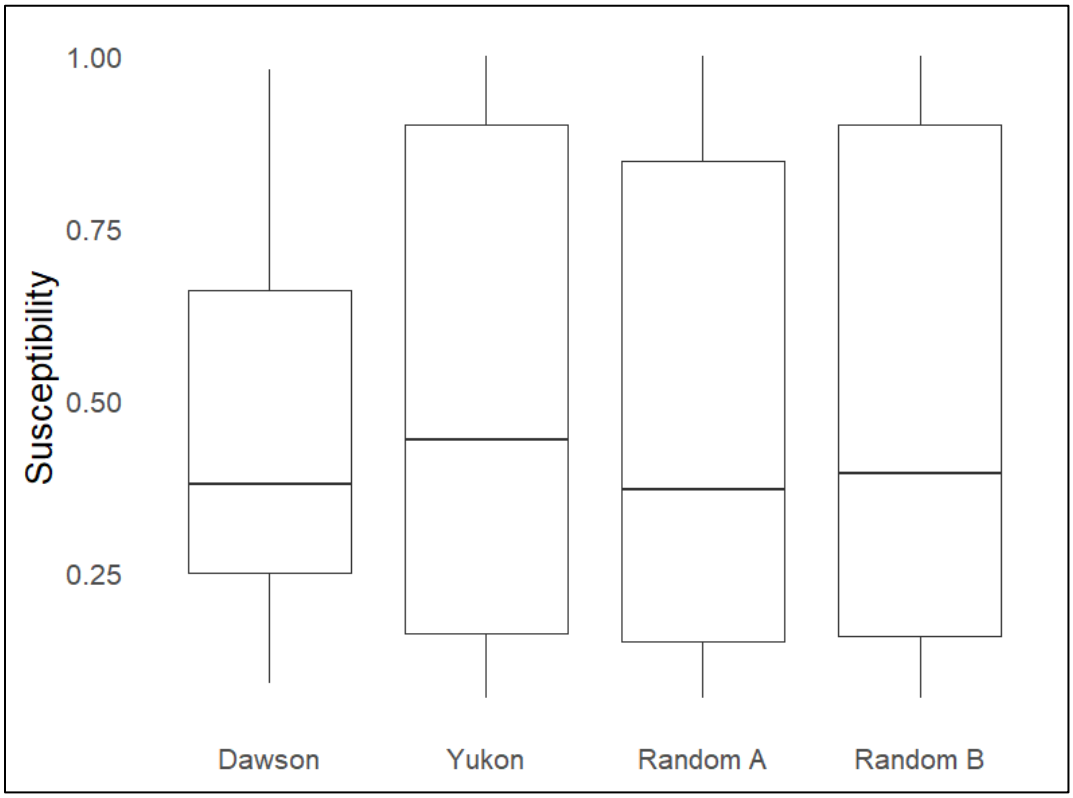

Figure 4.16. Box plots of landslide susceptibility of YGS points within the Dawson City study area (27), within Yukon (397) and two sets of randomly generated points in Yukon (397).

Table 4.15. Descriptive statistics of modelled landslide susceptibility values.

	Minimum	Maximum	Mean	S.D.
Dawson	0.092	0.979	0.462	0.280
Yukon	0.068	1.000	0.509	0.349
Random A	0.068	1.000	0.478	0.341
Random B	0.068	1.000	0.496	0.355

The count and percentage of the landslide points within each susceptibility class is shown in Table 4.16. Two χ^2 goodness of fit tests were applied to the YGS points and each of the random sets of points to determine whether or not the susceptibility values at the YGS points were significantly higher than the values at the randomly distributed points. These strongly indicate that there is no significant difference in the modelled susceptibility values of the YGS points and the random points (random points A: χ^2 value = 0.023, p-value = 0.988; random points B: χ^2 value = 0.027, p-value = 0.987), showing that the model of landslide susceptibility does not do a good job of predicting areas where landslides have developed.

Table 4.16. Thermokarst landslide susceptibility classification of YGS landslide points within the Dawson City study area (27), within Yukon (397) and two sets of points randomly distributed across Yukon (397).

Susceptibility Class / Sample	High	Medium	Low
YGS Dawson	6 (22.2%)	13 (48.1%)	8 (29.6%)
YGS Yukon	150 (37.8%)	98 (24.7%)	149 (37.5%)
Random Points A	133 (33.5%)	103 (25.9%)	161 (40.6%)
Random Points B	145 (36.5%)	88 (22.2%)	164 (41.3%)

Landslides were mapped in 11 of the 26 Yukon ecoregions. The modelled susceptibility values of the landslides within each of these is presented in Table 4.17. The majority of landslides are in the low susceptibility classification in all ecoregions except for the Peel River Plateau, Yukon Coastal Plain, British-Richardson Mountains and the Klondike Plateau ecoregions. The first three of these are in the north of the territory, where permafrost is more continuous, ground ice is more abundant, and sediment layers are both thicker and more likely to be of glacial origin. The landslides in these regions are also more likely to be retrogressive thaw slumps or active layer detachments, rather than rock- or landslides.

Table 4.17. Landslide susceptibility classifications of points mapped by the YGS within Yukon ecoregions.

Susceptibility Class / Ecoregion	High	Medium	Low	Total
Peel River Plateau	68 (38.6%)	54 (30.7%)	54 (30.7%)	176
McQuesten Highlands	8 (9.8%)	21 (25.6%)	53 (64.6%)	82
Yukon Coastal Plain	33 (82.5%)	2 (5%)	5 (12.5%)	40
British-Richardson Mountains	18 (58.1%)	11 (35.5%)	2 (6.5%)	31
Klondike Plateau	3 (25%)	4 (33.3%)	5 (41.7%)	12
Mackenzie Mountains	1 (10%)	(0%)	9 (90%)	10
Selwyn Mountains	(0%)	(0%)	9 (100%)	9
Pelly Mountains	(0%)	(0%)	9 (100%)	9
Yukon Plateau-North	3 (75%)	1 (25%)	(0%)	4
Fort MacPherson Plain	2 (50%)	(0%)	2 (50%)	4
Eagle Plains	(0%)	(0%)	2 (100%)	2

4.5.3 Pingos

Figure 4.17 shows pingo susceptibility in Yukon. At this scale, the entire territory appears to be at Low susceptibility. The concave locations in valley bottoms at beneath terraces to which High and Medium susceptibilities are constrained are so small as to appear invisible. In fact, approximately 93 % of Yukon is in the Low susceptibility class, approximately 7 % is in the Medium susceptibility class, and 0.1 % is in the High susceptibility class. Location (a) shows a high concentration of pingos in the Klondike Plateau immediately south of the Dawson City study area. These pingos seem to occupy a similar part of the landscape as the Dawson City pingos, and are likely all open-system (Hughes, 1969). The model seems to perform as well here as it does in the Dawson City study area, with most pingos in Medium or High susceptibility areas. Location (b) shows 11 pingos in the Northern Yukon Plateau, east of the community of Ross River. The landscape here is defined by low hills and little relief. While the pingos are not clustered as densely as in the Klondike Plateau, small, tight cluster of 2 to 3 pingos do occur here. All pingos are in the Low susceptibility class. The concave areas of Medium and High susceptibility are rare here. Location (c) shows a group of pingos in the Central Yukon Plateau, northeast of Carmacks and southeast of Pelly Crossing. These are not clustered as densely as the pingos in the Klondike Plateau. Tatlmain, Tadru and Ess Lakes are visible here, as well as several smaller thermokarst lakes. The landscape here is similar to that of Location (b). The pingos here are found on open slopes, often above lowlands, and are all in Low susceptibility areas.

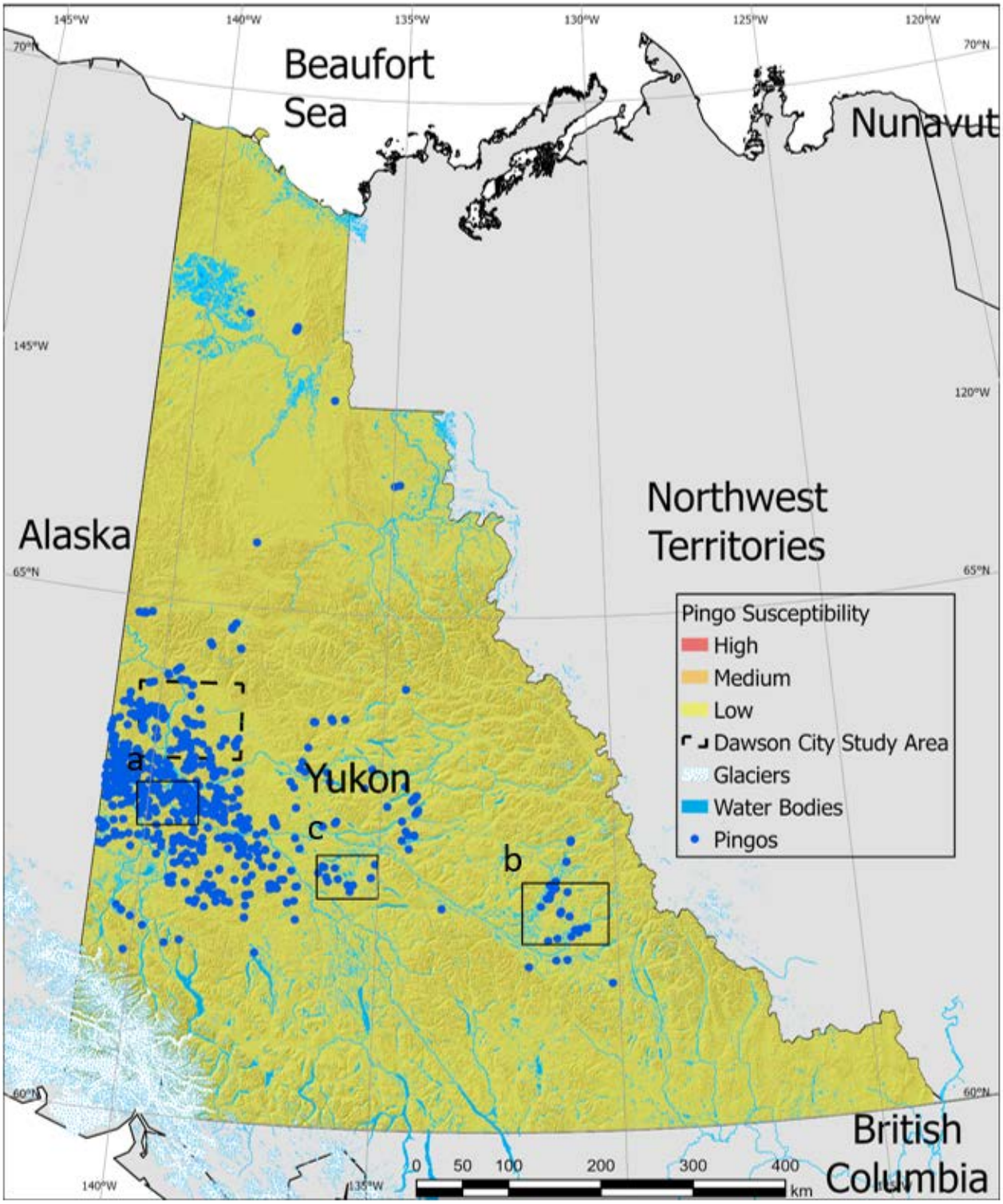

Figure 4.17. Pingo susceptibility in Yukon. High, medium and low susceptibility classes are shown. Insets a, b and c are shown in Figure 4.18.

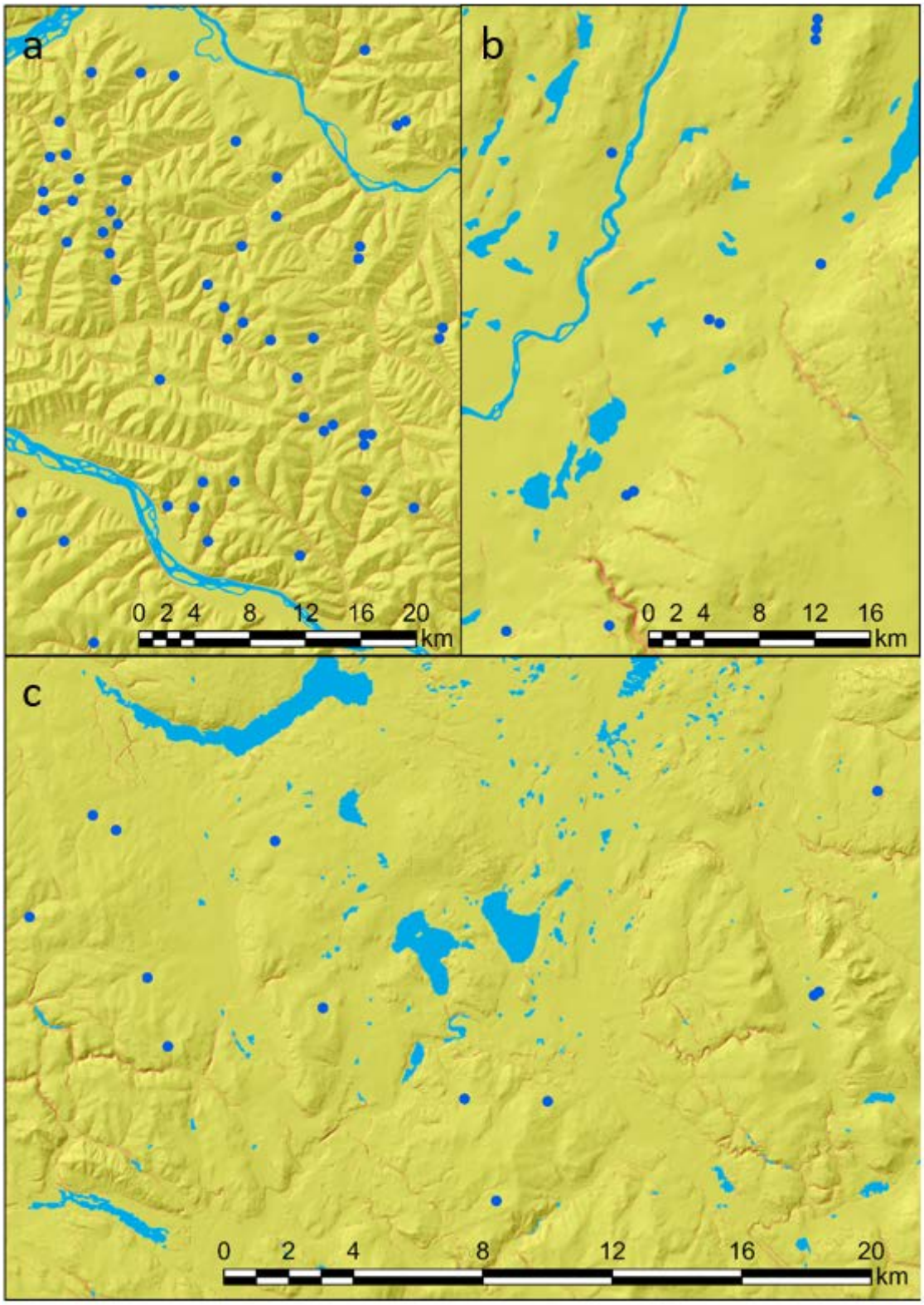

Figure 4.18. Pingo susceptibility and location of pingos mapped by the YGS for insets from Figure 4.17. General regions: a) Klondike Plateau; b) Central Yukon Plateau; c) Northern Yukon Plateau.

The distribution of modelled susceptibility values at the pingo points mapped by the YGS and at one set of points distributed randomly across Yukon is shown in Figure 4.19. This, as well as the descriptive statistics shown in Table 4.18, show that pingo susceptibility values across Yukon are exceptionally low. While the minimum and mean values in Table 4.18 are nearly equal, the maximum susceptibility value in the randomly distributed points is significantly larger than that of the YGS points. This can be interpreted as a type I error, and indicates that the model does not do a good job of predicting pingo susceptibility.

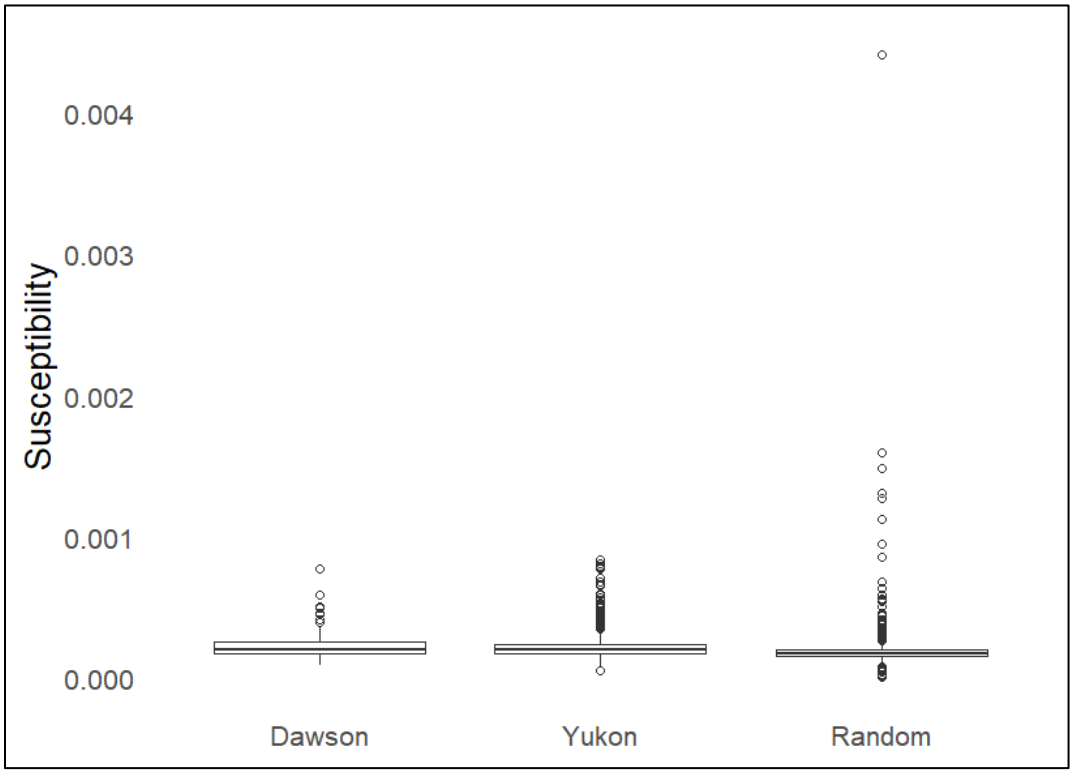

Figure 4.19. Box plots of pingo susceptibility of YGS points within the Dawson City study area (93), within Yukon (778) and two sets of randomly generated points in Yukon (778).

Table 4.18. Descriptive statistics of modelled pingo susceptibility values.

	Minimum	**Maximum**	**Mean**	**S.D.**
Dawson	0.0001	0.0008	0.0002	0.0001
Yukon	0.0001	0.0008	0.0002	0.0001
Random	< 0.0001	0.0044	0.0002	0.0002

The count and percentage of the pingo points within each susceptibility class is shown in Table 4.19. A χ^2 goodness of fit test was applied to the YGS points and the set of random points to determine whether or not the susceptibility values at the YGS points were significantly higher than the values at the randomly distributed points. This strongly indicates that there is no significant difference in the modelled susceptibility values of the YGS points and the random points (χ^2 value = 0.090, *p*-value = 0.956), showing that the model of pingo susceptibility does not do a good job of predicting areas where pingos have developed.

Table 4.19. Pingo susceptibility classification of YGS pingo points within the Dawson City study area (93), within Yukon (778) and randomly generated points in Yukon (778), for the univariate model using curvature.

Susceptibility Class / Sample Region	High	Medium	Low
YGS Yukon	0 (0%)	118 (15.2%)	660 (84.8%)
YGS Dawson	0 (0%)	18 (19.4%)	75 (80.6%)
Random Points	5 (0.6%)	54 (6.9%)	719 (92.4%)

A multivariate GLM using profile curvature and PRR_{CSS} was also assembled, and 93 points were randomly distributed throughout the Dawson City study area to assess its performance. The results of this multivariate model are shown in Table 4.20. Although the multivariate model performs better than the univariate model (more pingos classified as Medium susceptibility), it is not possible to apply to the rest of the territory, as the PRR model is prohibitively complex to assemble for such a large area.

Table 4.20. Pingo susceptibility classification of YGS pingo points within the Dawson City study area (93) and randomly generated points (93), from the multivariate GLM using curvature and PRR.

Susceptibility Class / Sample Region	High	Medium	Low
Dawson	0 (0%)	42 (45.2%)	44 (47.3%)
Random	1 (1.1%)	19 (20.4%)	66 (71%)

Pingos were mapped in 14 of the 26 Yukon ecoregions, though only six of those contain more than 10 pingos. The modelled susceptibility values from the univariate model of the pingos within each of these is presented in Table 4.21. The majority (> 80 %) of pingos are in the Low susceptibility class in all six of these ecoregions. The model performs best in the Klondike Plateau, where 18.6 % of pingos are in the Medium susceptibility classification. This is the only ecoregion where more than one pingo was classified above Low susceptibility.

Table 4.21. Pingo susceptibility classifications of points mapped by the YGS within Yukon ecoregions.

Ecoregion \ Susceptibility Class	High	Medium	Low	Total
Klondike Plateau	0 (0%)	114 (18.6%)	499 (81.4%)	613
Yukon Plateau-North	0 (0%)	1 (1.6%)	63 (98.4%)	64
Yukon Plateau-Central	0 (0%)	0 (0%)	36 (100%)	36
McQuesten Highlands	0 (0%)	0 (0%)	17 (100%)	17
Ruby-Nisling Ranges	0 (0%)	1 (6.7%)	14 (93.3%)	15
North Ogilvie Mountains	0 (0%)	1 (8.3%)	11 (91.7%)	12
Old Crow Basin	0 (0%)	0 (0%)	4 (100%)	4
Selwyn Mountains	0 (0%)	1 (25%)	3 (75%)	4
Peel River Plateau	0 (0%)	0 (0%)	4 (100%)	4
Mackenzie Mountains	0 (0%)	0 (0%)	2 (100%)	2
Wellesley Lake	0 (0%)	0 (0%)	2 (100%)	2
Eagle Plains	0 (0%)	0 (0%)	2 (100%)	2
Pelly Mountains	0 (0%)	0 (0%)	2 (100%)	2
St. Elias Mountains	0 (0%)	0 (0%)	1 (100%)	1

Chapter 5. Discussion

5.1 Thermokarst Landform Inventory

An inventory of thermokarst lakes, landslides and pingos was extracted as points from the Yukon Geological Survey's Digital Surficial Geology dataset (Yukon Geological Survey, 2020a). These landforms were then manually delineated in the Dawson City study area, and various metrics of their morphologies were recorded and compared to similar landforms in other regions found in the literature. These results revealed the thermokarst lakes and pingos in this region to be somewhat distinct from similar landforms elsewhere.

Specifically, thermokarst lakes in the Dawson City study area are, on average, smaller than lakes in the Lena Delta (Morgenstern et al., 2008) and larger than lakes in the Qinghai-Tibet Plateau (Niu et al., 2014). Thermokarst lakes are relatively rare in the Dawson City study area, while other parts of Yukon, such as the Old Crow Basin and the Yukon Plateau have much higher limnicity. Therefore, these two diverse ecoregions would be best for further study into thermokarst lake susceptibility in Yukon.

Landslides are also relatively uncommon in the Dawson City study area, compared to regions like the Peel Plateau, where retrogressive thaw slumps are numerous (Lacelle et al., 2015). One issue with the landslides in this study, and in general is that they are always mapped after they have occurred. Landslides can dramatically alter the topography of a location, and slope characteristics before the landslides occurred are not necessarily known besides the fact that they were steeper than after. Hence, it is difficult to predict areas where landslides may occur in the future. The landslides in the Dawson City study area are predominantly rockslides, rather than active layer detachments or retrogressive thaw slumps, both of which are sensitive to climatic and environmental change such as warming temperatures, unseasonal precipitation or melt and wildfire

(Lipovsky et al., 2005; Farquharson et al., 2019; Lewkowicz and Way, 2019). As such, landslide of the type mapped by the YGS may not increase in frequency as a result of climate change.

The montane pingos in the Dawson City study area are, on average, taller, wider and have steeper sides than pingos in the Western Canadian Arctic (Wolfe et al., 2023) and the Alaskan Western Arctic (Jones et al., 2012). The open-system pingos of the Klondike Plateau and neighbouring central Alaska were surveyed in the 1960s (Holmes et al., 1968; Hughes, 1969), but have not been the subject of new research since then. Given the polycyclic nature of pingos, their distribution in these regions has likely changed since then as old pingos collapse and, potentially, new pingos develop. During the landform delineation, it was observed that all pingos in the Dawson City study area appeared to have collapsed in the Maxar Vivid imagery from 2011 and 2017. This is likely due to climate change, and could corroborate the prediction of loss of environmental space for pingos in this region from Karjalainen et al. (2020). Further investigation into these montane pingos is justified, and a comparison between Holmes et al. (1968), Hughes (1969) and their present distribution, found from satellite imagery interpretation, would be a relatively simple undertaking.

Even though the YGS Digital Surficial Geology dataset is being continually updated (Yukon Geological Survey, 2020a), it is not ideal for modelling projects like this one because landforms were not mapped with this purpose in mind. Future mapping is not likely to be exhaustive for the entire territory, since different areas have varying requirements for surficial geology mapping (i.e. areas with active or prospective mining, or population centres will be the subject of more detailed mapping, while areas with less human presence will be mapped only at a large scale. This issue highlights the value of projects like the Northwest Territories Thermokarst Mapping Collective (Kokelj et al., 2023). Projects with the goal to map specific landforms in their entirety over large areas

using a rigorous, standardized satellite imagery interpretation procedure and an associated estimate of error are key to future susceptibility modelling efforts since models depend on the quality of their input data.

5.2 Thermokarst Susceptibility Models

Generalized linear models of thermokarst lake, landslide and pingo susceptibility were constructed using topographic, geologic and environmental variables. While these models were classified into High, Medium and Low susceptibility classes, the actual susceptibility values varied greatly. The maximum thermokarst lake, landslide and pingo susceptibility values in Yukon were 0.0043, 1.0 and 0.0044 respectively. Since the models are only trained on the data from the Dawson City study area, these values are not truly representative of the rest of the territory. In reality, much of Yukon has higher limnicity and landslide occurrence than Dawson, though the Klondike Plateau has by far the highest concentration of pingos in the territory. However, these values are comparable to those from Yin et al. (2021), who developed a machine learning model of thermokarst lake susceptibility, which classified 1.4 % of the Qinghai-Tibet Plateau as being highly susceptible.

The thermokarst lake susceptibility model in this thesis performed best, effectively classifying the majority of mapped thermokarst lakes in Yukon as either medium or high susceptibility. This shows that relatively simple models have potential in thermokarst susceptibility modelling, with the advantage of computational and data requirements and easier interpretation. The landslide and pingo models did not perform as well, failing to classify a significant portion of mapped landforms in Yukon as medium or high susceptibility. While the pingos in the rest of Yukon, especially the Yukon Plateau, seem to be distinct from those in the Klondike Plateau, those in Alaska (Holmes et al. 1969) may

be more similar. Therefore, the pingo susceptibility model could potentially perform better in adjacent Central Alaska than it does in the rest of Yukon.

Landslide susceptibility has been modelling using a number of different methods. A generalized linear model applied to landslides in a 65 km^2 area in northern Italy, used topographic and geologic predictor variables (Atkinson et al., 1998). Rock type, slope, strike angle, vegetation cover and concavity were the most significant variables. This implies that including more geologic predictor variables could improve landslide model performance. Slope, wetness index and planform curvature were the most important variables in a random forest model of landslides mapped by air and satellite photo interpretation in the Alaska Highway Corridor in Yukon (Behnia and Blais-Stevens, 2018). Two climatological variables, annual precipitation and thawing degree days were the most important variables in a random forest model of thermokarst landslides on the Qinghai-Tibet Plateau (Yin et al., 2021).

The only predictor variables used in the optimal models in this thesis were slope and profile curvature, both topographic variables. Of the ten predictor variables included in the models, four are topographic, three are climatic and three are geologic. While all variables were significant at the 95% confidence interval in the landslide univariate models, only three topographic and three climatic variables were significant in the lake univariate models, and two topographic and one climatic variable were significant in the pingo univariate models. While the lack of statistically significant univariate models using geologic variables could be a result of poor data quality, it is more likely the case that there is higher overall variability in topography and climate in this area, and that statistical models therefore return these variables as the main controls of the specific landform processes. This is comparable to the results of Wang et al. (2023), where the three most important variables in a machine learning model of thermokarst lake susceptibility in the Northern Hemisphere were topographic variables (slope, elevation

and height above nearest drainage), followed by three climatic variables (rainfall, mean annual ground temperature and normalized difference vegetation index). Conversely, the thermokarst lake susceptibility model developed by Niu et al. (2015) for the Qinghai-Tibet engineering corridor ranked the ice content of permafrost above two climatic variables (mean annual ground temperature and vegetation cover), surficial material type and surface curvature.

In order to further investigate the influence of variability in and types of independent variables and to better control for multicollinearity of primary (e.g. slope and aspect) and secondary (e.g. solar radiation) DEM-derived variables, one could exclude specific areas (mask) based on knowledge of geomorphological processes indicating likelihood or implausibility of thermokarst landform occurrence in certain terrain. For example, all areas with slopes steeper than 2° could be removed from the lake susceptibility model input data, as these areas are scientifically implausible locations for lake development. Another example would be to mask areas with regolith (bedrock) from the landslide susceptibility model input data, as, while these areas may be prone to rockslides, landslides can only occur in unconsolidated materials. By essentially removing extraneous variability in the input data, relationships between predictor and response variables could potentially become more informative. Specific areas could even be excluded from all models: for example, the anthropogenic surficial material class from the YGS dataset, or the Canada Human Footprint dataset (Hirsh-Pearson et al., 2022), could be used to remove the Klondike goldfields from the model input data.

Based on the results in this thesis, and recent publications, additions to the set of model predictor variables could include the following. Since the montane pingos in the Klondike Plateau seem to occur adjacent to upland streams, and are rarely found near the larger rivers (Hughes, 1969), a Strahler stream order could be calculated per catchment and applied as a predictor variable with a hypothesized inverse relationship.

The NWT Thermokarst Mapping Collective (Kokelj et al., 2023) found that the distribution of thaw lakes and retrogressive thaw slumps closely follows paleo-ice margins, due to the abundance of relict ice deposited in those locations during glacial recession. Based on the univariate model results presented in this thesis, using soil or sediment texture as a proxy for ground ice content was not sufficient. Better ground ice data, at a higher spatial resolution than O'Neill et al. (2019), could help to fill this data gap. The SOC-ICE-v1.0 model (Saito et al., 2020) has some potential for this, but its 1° spatial resolution is likely too coarse for it to be effective as a predictor of thermokarst susceptibility at scales useable by communities or territories. The 1 km spatial resolution ground ice content model for the northern Hemisphere from Karjalainen et al. (2022) has great potential for inclusion in future thermokarst susceptibility modelling projects. Finally, a soil environmental model such as the WATEREGO model (Lacelle et al., 2022) could be employed to gain more accurate estimates of ground ice content in the region.

Models of potential changes in climatological niches for pingos, ice wedge polygons and rock glaciers from Karjalainen et al. (2020) offer a different approach to thermokarst modelling. Since thermokarst development ultimately results from permafrost thaw, a climatic phenomenon, climate change is a key dimension to consider. However, the greatest predicted changes to climatological niches for these landforms in Canada all occur in the high Arctic, far from this study's location. However, projections of permafrost extent place most of southern Yukon free of permafrost by 2041–2060 following RCP4.5 (Hjort et al., 2018) which means that thermokarst will rapidly develop in this sub-Arctic region as well over the coming decades.

Chapter 6. Summary and Conclusions

This thesis project had the objectives of (1) describing thermokarst landforms in the Dawson City study area, (2) developing thermokarst susceptibility models using those landforms and (3) validate the models in the rest of Yukon using other thermokarst landforms. All thesis objectives were achieved.

In Section 3.2 a thermokarst landform inventory of 3376 thermokarst lakes, landslides and pingos was extracted from the Yukon Geological Survey's Digital Surficial Geology dataset (Yukon Geological Survey, 2020a). The 149 points in the Dawson City study area were manually delineated, and morphologic metrics were extracted. In Section 3.3 a literature review of thermokarst and periglacial modelling studies was conducted, and 10 of the most prevalent and suitable input variables were selected to be applied in the current study. These input variables were subsequently extracted directly from existing databases or derived or combined from other datasets. In Section 3.4 the distribution of the thermokarst landforms in the Dawson City study area was analysed using histograms and average nearest neighbour, a metric of spatial clustering. In Section 3.5 generalized linear models were developed for thermokarst lake, landslide and pingo susceptibility using the landform polygons from Section 3.2 and the input variables from Section 3.3. In Section 3.6 these models were validated using the remaining landform points outside of the Dawson City study area and sets of randomly distributed points.

In Sections 4.1 and 4.2 the distribution and morphology of the thermokarst landforms was presented. In doing so, the unique morphology of montane pingos in the Klondike Plateau was detailed and compared to Arctic pingos, while the thermokarst lakes in the study area were compared to thermokarst lakes in an arctic and an alpine region. This highlighted the variability that exists in thermokarst landforms across the northern Hemisphere's permafrost zones. In Section 4.3 the results of the susceptibility

models were presented and mapped in the Dawson City study area. In Section 4.4 the models were mapped in all of Yukon and validated using the other landform points and the randomly distributed points. The thermokarst lake susceptibility model succeeded in predicting thermokarst lake presence using this method, while the landslide and pingo models did not perform that satisfactorily. This showed that relatively simple generalized linear models have the ability to perform quite well, and that interpretation of results of both good and poorer models can be informative, but it was not tested whether more complex, modern machine learning techniques would outperform these simple probability models.

Permafrost thaw and thermokarst development are accelerating rapidly as the global climate warms. As such, it is crucial for land users and managers to know the probable changes that different landscapes will undergo. The results of this study underline both the importance of landform inventory projects, and the disparity in the amount of permafrost research conducted in mountainous regions compared to that in the High Arctic lowlands. In order for thermokarst susceptibility models to be effective, regardless of which type of model is used, high-quality contemporary input data are required. The YGS surficial geology dataset, the only available source for this study, was not ideal, as pingos labelled as intact were all observed in more recent satellite imagery to have collapsed, and many more thermokarst features were observed in recent imagery than are mapped in the YGS dataset. Projects like the NWT Thermokarst Mapping Collective (Kokelj et al., 2023) need to be widely adopted by research institutes and governments if susceptibility mapping or hazard mapping are a goal. Experts in geomorphological processes and landform identification are key to the success of this type of project.

6.1 Suggestions for Further Research

The following points are promising continuations of this study:

- Assembly of a comprehensive thermokarst landform inventory using rigorous mapping methods for Yukon, similar to the work of Kokelj et al. (2023) and Lindgren et al. (2021).
- Expansion of landform polygonization for all of Yukon to gain further knowledge about landform distribution and morphology across the territory, and potentially to aid in future modelling projects.
- Expansion of the snow metrics dataset from Lindsay et al. (2015) to other regions using data from Hall et al. (2002), and its further implementation into radiation models.
- The use of masks in the modelling analysis, for example removing all steep areas from the lake susceptibility model input data.
- The addition of more predictor variables in susceptibility models such as topographic position index, as this could potentially outperform topographic curvature in predicting pingo distribution. Ground ice content, as modelled by Lacelle et al. (2022), and mean annual ground temperature and its rate of change are key indicators of permafrost thaw susceptibility, and have been included in similar thermokarst susceptibility models such as Niu et al. (2015).
- Integration of the role of wildfire into the susceptibility models. For example, the age of forestry stands could be incorporated, with older stands presumed to be likelier to experience wildfire than younger stands.
- Analyzing the modelled susceptibility values of infrastructure (roads, dwellings, etc.) in Yukon, as per Hjort et al. (2018).
- Addition of the three susceptibility models into one thermokarst susceptibility map, highlighting the overlap in areas of high susceptibility.

References

Abolt, C.J. and Young, M.H., 2020. High-resolution mapping of spatial heterogeneity in ice wedge polygon geomorphology near Prudhoe Bay, Alaska. Scientific Data, 7(1): 87.

Ahrens, R.J., Bockheim, J.G. and Ping, C.L., 2004. The Gelisol Order in Soil Taxonomy. In: J.M. Kimble (Editor), Cryosols: Permafrost-Affected Soils. Springer Berlin Heidelberg, Berlin, Heidelberg, pp. 627-635.

Akaike, H., 1974. A new look at the statistical model identification. IEEE Transactions on Automatic Control, 19(6): 716-723.

Anisimov, O.A., Shiklomanov, N.I. and Nelson, F.E., 1997. Global warming and active-layer thickness: results from transient general circulation models. Global and Planetary Change, 15(3): 61-77.

Arenson, L.U., Kääb, A. and O'Sullivan, A., 2016. Detection and Analysis of Ground Deformation in Permafrost Environments. Permafrost and Periglacial Processes, 27(4): 339-351.

Armstrong McKay, D.I., Staal, A., Abrams, J.F., Winkelmann, R., Sakschewski, B., Loriani, S., Fetzer, I., Cornell, S.E., Rockström, J. and Lenton, T.M., 2022. Exceeding 1.5°C global warming could trigger multiple climate tipping points. Science, 377(6611): eabn7950.

Arp, C.D., Whitman, M.S., Jones, B.M., Grosse, G., Gaglioti, B.V. and Heim, K.C., 2015. Distribution and biophysical processes of beaded streams in Arctic permafrost landscapes. Biogeosciences, 12(1): 29-47.

Atkinson, P., Jiskoot, H., Massari, R. and Murray, T., 1998. Generalized linear modelling in geomorphology. Earth Surface Processes and Landforms, 23(13): 1185-1195.

Avand, M., Mohammadi, M., Mirchooli, F., Kavian, A. and Tiefenbacher, J.P., 2023. A New Approach for Smart Soil Erosion Modeling: Integration of Empirical and Machine-Learning Models. Environmental Modeling & Assessment, 28(1): 145-160.

Babiński, Z., 1982. Pingo degradation in the Bayan-Nuurin-Khotnor Basin, Khangai Mountains, Mongolia. Boreas, 11: 291-298.

Ballinger, T.J., Overland, J.E., Wang, M., Walsh, J.E., Brettschneider, B., Thoman, R.L., Bhatt, U.S., Hanna, E., Hanssen-Bauer, I. and Kim, S.-J., 2022. Surface Air Temperature. In: M.L. Druckenmiller, R.L. Thoman and T.A. Moon (Editors), Arctic Report Card 2022.

Balser, A.W., Gooseff, M.N., Jones, J.B. and Bowden, W.B., 2009. Thermokarst distribution and relationships to landscape characteristics in the Feniak Lake region, Noatak National Preserve, Alaska, Arctic Network, National Park Service, Fairbanks, AK.

Balser, A.W., Jones, J.B. and Gens, R., 2014. Timing of retrogressive thaw slump initiation in the Noatak Basin, northwest Alaska, USA. Journal of Geophysical Research: Earth Surface, 119(5): 1106-1120.

Baltzer, J.L., Veness, T., Chasmer, L.E., Sniderhan, A.E. and Quinton, W.L., 2014. Forests on thawing permafrost: fragmentation, edge effects, and net forest loss. Global Change Biology, 20(3): 824-834.

Banin, A. and Anderson, D.M., 1974. Effects of salt concentration changes during freezing on the unfrozen water content of porous materials. Water Resources Research, 10(1): 124-128.

Bartsch, A., Strozzi, T. and Nitze, I., 2023. Permafrost Monitoring from Space. Surveys in Geophysics.

Beck, H.E., McVicar, T.R., Vergopolan, N., Berg, A., Lutsko, N.J., Dufour, A., Zeng, Z., Jiang, X., van Dijk, A.I.J.M. and Miralles, D.G., 2023. High-resolution (1 km) Köppen-Geiger maps for 1901–2099 based on constrained CMIP6 projections. Scientific Data, 10(1): 724.

Behnia, P. and Blais-Stevens, A., 2018. Landslide susceptibility modelling using the quantitative random forest method along the northern portion of the Yukon Alaska Highway Corridor, Canada. Natural Hazards, 90(3): 1407-1426.

Beilman, D.W., Vitt, D.H. and Halsey, L.A., 2001. Localized Permafrost Peatlands in Western Canada: Definition, Distributions, and Degradation. Arctic, Antarctic, and Alpine Research, 33(1): 70-77.

Belshe, E.F., Schuur, E.A.G. and Grosse, G., 2013. Quantification of upland thermokarst features with high resolution remote sensing. Environmental Research Letters, 8(3): 035016.

Benkert, B., Fortier, D., Lipovsky, P.S., Lewkowicz, A.G., de Grandpré, I., Grandmont, K., Turner, D.G., Laxton, S., Moote, K. and Roy, L.-P., 2015a. Ross River Landscape Hazards: Geoscience mapping for climate change adaptation planning, Northern Climate ExChange, Yukon Research Centre, Yukon College, Whitehorse, Yukon.

Benkert, B., Kennedy, K., Fortier, D., Lewkowicz, A.G., Roy, L.-P., de Grandpré, I., Grandmont, K., Drukis, S., Colpron, M. and Light, E., 2016. Old Crow Landscape Hazards: Geoscience mapping for climate change adaptation planning, Northern Climate ExChange, Yukon Research Centre, Yukon College, Whitehorse, Yukon.

Benkert, B., Kennedy, K., Fortier, D., Lewkowicz, A.G., Roy, L.-P., Grandmont, K., de Grandpré, I., McKenna, K.M. and Moote, K., 2015b. Dawson City Landscape Hazards: Geoscience mapping for climate change adaptation planning, Northern Climate ExChange, Yukon Research Centre, Yukon College, Whitehorse, Yukon.

Berry, H.B., Whalen, D. and Lim, M., 2021. Long-term ice-rich permafrost coast sensitivity to air temperatures and storm influence: lessons from Pullen Island, Northwest Territories, Canada. Arctic Science, 7(4): 723-745.

Biskaborn, B.K., Smith, S.L., Noetzli, J., Matthes, H., Vieira, G., Streletskiy, D.A., Schoeneich, P., Romanovsky, V.E., Lewkowicz, A.G., Abramov, A., Allard, M., Boike, J., Cable, W.L., Christiansen, H.H., Delaloye, R., Diekmann, B., Drozdov, D., Etzelmüller, B., Grosse, G., Guglielmin, M., Ingeman-Nielsen, T., Isaksen, K., Ishikawa, M., Johansson, M., Johannsson, H., Joo, A., Kaverin, D., Kholodov, A., Konstantinov, P., Kröger, T., Lambiel, C., Lanckman, J.-P., Luo, D., Malkova, G., Meiklejohn, I., Moskalenko, N., Oliva, M., Phillips, M., Ramos, M., Sannel, A.B.K., Sergeev, D., Seybold, C., Skryabin, P., Vasiliev, A., Wu, Q., Yoshikawa, K., Zheleznyak, M. and Lantuit, H., 2019. Permafrost is warming at a global scale. Nature Communications, 10(1): 264.

Black, R.F. and Barksdale, W.L., 1949. Oriented Lakes of Northern Alaska. The Journal of Geology, 57(2): 105-118.

Boike, J., Georgi, C., Kirilin, G., Muster, S., Abramova, K., Fedorova, I., Chetverova, A., Grigoriev, M., Bornemann, N. and Langer, M., 2015. Thermal processes of thermokarst lakes in the continuous permafrost zone of northern Siberia – observations and modeling (Lena River Delta, Siberia). Biogeosciences, 12(20): 5941-5965.

Bond, J.D., 2003. Late Wisconsinan McConnell glaciation of the Whitehorse map area (105D), Yukon. In: D.S. Emond and L.L. Lewis (Editors), Yukon Exploration and Geology 2003. Yukon Geological Survey, Whitehorse, YT, pp. 73-88.

Bonnaventure, P.P. and Lamoureux, S.F., 2013. The active layer: A conceptual review of monitoring, modelling techniques and changes in a warming climate. Progress in Physical Geography: Earth and Environment, 37(3): 352-376.

Bonnaventure, P.P. and Lewkowicz, A.G., 2008. Mountain permafrost probability mapping using the BTS method in two climatically dissimilar locations, northwest Canada. Canadian Journal of Earth Sciences, 45(4): 443-455.

Bonnaventure, P.P., Lewkowicz, A.G., Kremer, M. and Sawada, M.C., 2012. A Permafrost Probability Model for the Southern Yukon and Northern British Columbia, Canada. Permafrost and Periglacial Processes, 23(1): 52-68.

Bowden, W.B., 2010. Climate Change in the Arctic – Permafrost, Thermokarst, and Why They Matter to the Non-Arctic World. Geography Compass, 4(10): 1553-1566.

Bowden, W.B., Gooseff, M.N., Balser, A., Green, A., Peterson, B.J. and Bradford, J., 2008. Sediment and nutrient delivery from thermokarst features in the foothills of the North Slope, Alaska: Potential impacts on headwater stream ecosystems. Journal of Geophysical Research: Biogeosciences, 113(G2).

Brabets, T.P., Wang, B. and Meade, R.H., 2000. Environmental and hydrologic overview of the Yukon River Basin, Alaska and Canada, U.S. Department of the Interior, U.S. Geological Survey, Anchorage, AK.

Brideau, M.-A., Stead, D., Stevens, V., Roots, C., Lipovsky, P. and VonGaza, P., 2006. The Dawson City landslide (Dawson map area, NTS 116B/3), central Yukon. In: D.S. Emond, L.L. Lewis and L.H. Weston (Editors), Yukon Exploration and Geology 2006. Yukon Geological Survey, Whitehorse, YT, pp. 123-138.

Brooker, A., Fraser, R.H., Olthof, I., Kokelj, S.V. and Lacelle, D., 2014. Mapping the Activity and Evolution of Retrogressive Thaw Slumps by Tasselled Cap Trend Analysis of a Landsat Satellite Image Stack. Permafrost and Periglacial Processes, 25(4): 243-256.

Brown, R.J.E., 1963. Influence of Vegetation on Permafrost, Permafrost International Conference, Lafayette, IN, pp. 20-25.

Budimir, M.E.A., Atkinson, P.M. and Lewis, H.G., 2015. A systematic review of landslide probability mapping using logistic regression. Landslides, 12(3): 419-436.

Burn, C.R. and Lewkowicz, A.G., 1990. Canadian Landform Examples - 17 Retrogressive Thaw Slumps. Canadian Geographies / Géographies canadiennes, 34(3): 273-276.

Burn, C.R., Moore, J.L., O'Neill, B.H., Hayley, D.W., Trimble, J.R., Calmels, F., Orban, S.N. and Idrees, M., 2015. Permafrost characterization of the Dempster Highway, Yukon and Northwest Territories, GeoQuebec 2015, 68th Canadian Geotechnical Conference and 7th Canadian Permafrost Conference, Quebec, QC.

Burt, T.P. and Williams, P.J., 1976. Hydraulic conductivity in frozen soils. Earth Surface Processes, 1(4): 349-360.

Calmels, F., Roy, L.-P., Grandmont, K. and Pugh, R., 2018. Summary of climate- and geohazard-related vulnerabilities for the Dempster Highway corridor. Northern Climate ExChange, Yukon Research Centre, Whitehorse, YT.

Calmels, F., Roy, L.-P., Laurent, C., Pelletier, M., Kinnear, L., Benkert, B., Horton, B. and Pumple, J., 2015. Vulnerability of the North Alaska Highway to Permafrost Thaw: a Field Guide and Data Synthesis. Northern Climate ExChange, Yukon Research Centre, Whitehorse, YT.

Cameron, E.A., Lantz, T.C. and Kokelj, S.V., 2023. Impacts of shrub removal on snow and near-surface thermal conditions in permafrost terrain adjacent to the Dempster Highway, NT, Canada. Arctic Science, e-First.

Candela, S.G., Howat, I., Noh, M.-J., Porter, C.C. and Morin, P.J., 2017. ArcticDEM validation and accuracy assessment, 2017 AGU Fall Meeting, New Orleans, LA, pp. C51A-0332.

Cannone, N., Lewkowicz, A.G. and Guglielmin, M., 2010. Vegetation colonization of permafrost-related landslides, Ellesmere Island, Canadian High Arctic. Journal of Geophysical Research: Biogeosciences, 115(G4).

Carpino, O., Haynes, K., Connon, R., Craig, J., Devoie, É. and Quinton, W., 2021. Long-term climate-influenced land cover change in discontinuous permafrost peatland complexes. Hydrol. Earth Syst. Sci., 25(6): 3301-3317.

Chasmer, L. and Hopkinson, C., 2017. Threshold loss of discontinuous permafrost and landscape evolution. Global Change Biology, 23(7): 2672-2686.

Chasmer, L., Hopkinson, C. and Quinton, W., 2010. Quantifying errors in discontinuous permafrost plateau change from optical data, Northwest Territories, Canada: 1947–2008. Canadian Journal of Remote Sensing, 36(sup2): S211-S223.

Connon, R., Devoie, É., Hayashi, M., Veness, T. and Quinton, W., 2018. The Influence of Shallow Taliks on Permafrost Thaw and Active Layer Dynamics in Subarctic Canada. Journal of Geophysical Research: Earth Surface, 123(2): 281-297.

Côté, M.M. and Burn, C.R., 2002. The oriented lakes of Tuktoyaktuk Peninsula, Western Arctic Coast, Canada: a GIS-based analysis. Permafrost and Periglacial Processes, 13(1): 61-70.

Coultish, T. and Lewkowicz, A., 2003. Palsa dynamics in a subarctic mountainous environment, Wolf Creek, Yukon Territory, Canada. In: W. Haeberli and D. Brandova (Editors), Eighth International Conference on Permafrost. Glaciology and Geomorphodynamics Group, Geography Department, University of Zurich, Switzerland, Zurich, Switzerland, pp. 163-168.

Couture, N.J. and Pollard, W.H., 2017. A Model for Quantifying Ground-Ice Volume, Yukon Coast, Western Arctic Canada. Permafrost and Periglacial Processes, 28(3): 534-542.

Crate, S.A., 2022. Sakha and Alaas: Place Attachment and Cultural Identity in a Time of Climate Change. Anthropology and Humanism, 47(1): 20-38.

Daily, W., Ramirez, A., Binley, A. and LeBrecque, D., 2004. Electrical resistance tomography. The Leading Edge, 23(5): 438-442.

Daly, S.V., Bonnaventure, P.P. and Kochtitzky, W., 2022. Influence of ecosystem and disturbance on near-surface permafrost distribution, Whatì, Northwest Territories, Canada. Permafrost and Periglacial Processes, 33(4): 339-352.

Davis, J., Heginbottom, J., Annan, A., Daniels, R., Berdal, B., Bergan, T., Duncan, K., Lewin, P., Oxford, J., Roberts, N., Skehel, J. and Smith, C., 2000. Ground Penetrating Radar Surveys to Locate 1918 Spanish Flu Victims in Permafrost. Journal of Forensic Sciences, 45(1): 68-76.

Davis, J.C., 2002. Statistics and data analysis in geology, 3rd ed. Wiley, 656 pp.

De Pascale, G.P., Pollard, W.H. and Williams, K.K., 2008. Geophysical mapping of ground ice using a combination of capacitive coupled resistivity and ground-penetrating radar, Northwest Territories, Canada. Journal of Geophysical Research: Earth Surface, 113(F2).

Demidov, V., Demidov, N., Verkulich, S. and Wetterich, S., 2022. Distribution of pingos on Svalbard. Geomorphology, 412: 108326.

Devoie, É., Connon, R.F., Beddoe, R., Goordial, J., Quinton, W.L. and Craig, J.R., 2024. Disconnected active layers and unfrozen permafrost: A discussion of permafrost-related terms and definitions. Science of The Total Environment, 912: 169017.

Devoie, É.G., Craig, J.R., Connon, R.F. and Quinton, W.L., 2019. Taliks: A Tipping Point in Discontinuous Permafrost Degradation in Peatlands. Water Resources Research, 55(11): 9838-9857.

Dowle, M. and Srinivasan, A., 2023. data.table: Extension of 'data.frame'. R package version 1.14.8.

Duk-Rodkin, A., 1999. Glacial limits map of Yukon Territory. Geological Survey of Canada, Open File 3694, Indian and Northern Affairs Canada, Geoscience Map 1999-2.

Duk-Rodkin, A. and Barendregt, R.W., 2011. Chapter 49 - Stratigraphical Record of Glacials/Interglacials in Northwest Canada. In: J. Ehlers, P.L. Gibbard and P.D. Hughes (Editors), Developments in Quaternary Sciences. Elsevier, pp. 661-698.

Duk-Rodkin, A. and Barendregt, R.W., 2023. Glacial history and limits of Cordilleran and Laurentide ice sheets in the Mackenzie Mountains, foothills, and plains, Northwest Territories: a brief overview. In: I. McMartin (Editor), Surficial geology of northern Canada: a summary of Geo-mapping for Energy and Minerals program contributions. Geological Survey of Canada, pp. 113-143.

Duk-Rodkin, A., Barendregt, R.W. and White, J.M., 2010. An extensive late Cenozoic terrestrial record of multiple glaciations preserved in the Tintina Trench of west-central Yukon: stratigraphy, paleomagnetism, paleosols, and pollen. Canadian Journal of Earth Sciences, 47(7): 1003-1028.

Environment and Climate Change Canada, 2023. Canadian Climate Normals 1981-2010 Station Data: Dawson City, Yukon.

Etzelmüller, B., 2013. Recent Advances in Mountain Permafrost Research. Permafrost and Periglacial Processes, 24(2): 99-107.

Etzelmüller, B., Hoelzle, M., Flo Heggem, E.S., Isaksen, K., Mittaz, C., Mühll, D.V., Ødegård, R.S., Haeberli, W. and Sollid, J.L., 2001. Mapping and modelling the occurrence and distribution of mountain permafrost. Norsk Geografisk Tidsskrift-Norwegian Journal of Geography, 55(4): 186-194.

Fan, X.-w., Lin, Z.-j., Gao, Z.-y., Meng, X.-l., Niu, F.-j., Luo, J., Yin, G.-a., Zhou, F.-j. and Lan, A.-y., 2021. Cryostructures and ground ice content in ice-rich permafrost area of the Qinghai-Tibet Plateau with Computed Tomography Scanning. Journal of Mountain Science, 18(5): 1208-1221.

Farquharson, L.M., Mann, D.H., Grosse, G., Jones, B.M. and Romanovsky, V.E., 2016. Spatial distribution of thermokarst terrain in Arctic Alaska. Geomorphology, 273: 116-133.

Farquharson, L.M., Romanovsky, V.E., Cable, W.L., Walker, D.A., Kokelj, S.V. and Nicolsky, D., 2019. Climate Change Drives Widespread and Rapid Thermokarst Development in Very Cold Permafrost in the Canadian High Arctic. Geophysical Research Letters, 46(12): 6681-6689.

Fewster, R.E., Morris, P.J., Ivanovic, R.F., Swindles, G.T., Peregon, A.M. and Smith, C.J., 2022. Imminent loss of climate space for permafrost peatlands in Europe and Western Siberia. Nature Climate Change, 12(4): 373-379.

Fewster, R.E., Morris, P.J., Swindles, G.T., Ivanovic, R.F., Treat, C.C. and Jones, M.C., 2023. Holocene vegetation dynamics of circum-Arctic permafrost peatlands. Quaternary Science Reviews, 307: 108055.

Flemal, R.C., 1976. Pingos and Pingo Scars: Their Characteristics, Distribution, and Utility in Reconstructing Former Permafrost Environments. Quaternary Research, 6(1): 37-53.

Fortier, D., Allard, M. and Shur, Y., 2007. Observation of rapid drainage system development by thermal erosion of ice wedges on Bylot Island, Canadian Arctic Archipelago. Permafrost and Periglacial Processes, 18(3): 229-243.

Fortier, D., Strauss, J., Sliger, M., Calmels, F., Froese, D. and Shur, Y., 2018. Late Pleistocene yedoma in south-western Yukon (Canada): a remnant of Eastern Beringia? Laboratoire EDYTEM-Université Savoie Mont Blanc.

Frappier, R. and Lacelle, D., 2021. Distribution, morphometry, and ice content of ice-wedge polygons in Tombstone Territorial Park, central Yukon, Canada. Permafrost and Periglacial Processes, 32(4): 587-600.

French, H. and Shur, Y., 2010. The principles of cryostratigraphy. Earth-Science Reviews, 101(3): 190-206.

French, H.M., 2018. The Periglacial Environment: Fourth Edition. John Wiley & Sons Ltd, Hoboken, NJ.

Fritz, M., Vonk, J.E. and Lantuit, H., 2017. Collapsing Arctic coastlines. Nature Climate Change, 7(1): 6-7.

Froese, D.G., Zazula, G.D., Westgate, J.A., Preece, S.J., Sanborn, P.T., Reyes, A.V. and Pearce, N.J., 2009. The Klondike goldfields and Pleistocene environments of Beringia. GSA Today, 19(8): 4-10.

Frohn, R.C., Hinkel, K.M. and Eisner, W.R., 2005. Satellite remote sensing classification of thaw lakes and drained thaw lake basins on the North Slope of Alaska. Remote Sensing of Environment, 97(1): 116-126.

Fu, Z., Wu, Q., Zhang, W., He, H. and Wang, L., 2022. Water Migration and Segregated Ice Formation in Frozen Ground: Current Advances and Future Perspectives. Frontiers in Earth Science, 10.

Funk, M. and Hoelzle, M., 1992. A model of potential direct solar radiation for investigating occurrences of mountain permafrost. Permafrost and Periglacial Processes, 3(2): 139-142.

Getis, A., 1964. Temporal land-use pattern analysis with the use of nearest neighbor and quadrat methods. Annals of the Association of American Geographers, 54(3): 391-399.

Gibson, C., Morse, P.D., Kelly, J.M., Turetsky, M.R., Baltzer, J.L., Gingras-Hill, T. and Kokelj, S.V., 2020. Thermokarst Mapping Collective: Protocol for organic permafrost terrain and preliminary inventory from the Taiga Plains test area, Northwest Territories, Northwest Territories Geological Survey, Yellowknife, NT.

Gibson, C.M., Chasmer, L.E., Thompson, D.K., Quinton, W.L., Flannigan, M.D. and Olefeldt, D., 2018. Wildfire as a major driver of recent permafrost thaw in boreal peatlands. Nature Communications, 9(1): 3041.

Giesen, J., 2020. Position of the Sun by Spreadsheet for a day, http://www.geoastro.de/sunpos/day.html.

Godin, E. and Fortier, D., 2012. Geomorphology of a thermo-erosion gully, Bylot Island, Nunavut, Canada. Canadian Journal of Earth Sciences, 49(8): 979-986.

Government of Canada, 2024. First Nations Profiles, Crown-Indigenous Relations and Northern Affairs Canada.

Grandmont, K., Roy, L.-P., de Grandpré, I., Fortier, D., Benkert, B. and Lewkowicz, A., 2015. Impact of land cover disturbance on permafrost landscapes: Case Studies from Yukon communities. QB: GeoQuebec.

Greller, A.M., Goldstein, M. and Marcus, L., 1974. Snowmobile Impact on Three Alpine Tundra Plant Communities. Environmental Conservation, 1(2): 101-110.

Grosse, G., Romanovsky, V., Jorgenson, T., Anthony, K.W., Brown, J. and Overduin, P.P., 2011. Vulnerability and Feedbacks of Permafrost to Climate Change. Eos, Transactions American Geophysical Union, 92(9): 73-74.

Grosse, G., Romanovsky, V., Walter, K., Morgenstern, A., Lantuit, H. and Zimov, S., 2008. Distribution of thermokarst lakes and ponds at three yedoma sites in Siberia. In: D.L. Kane and K.M. Hinkel (Editors), Ninth International Conference on Permafrost. Institute of Northern Engineering, University of Alaska Fairbanks, Fairbanks, AK.

Guglielmin, M., Evans, C.J.E. and Cannone, N., 2008. Active layer thermal regime under different vegetation conditions in permafrost areas. A case study at Signy Island (Maritime Antarctica). Geoderma, 144(1-2): 73-85.

Gulev, S.K., Thorne, P.W., Ahn, J., Dentener, F.J., Domingues, C.M., Gerland, S., Gong, D., Kaufman, D.S., Nnamchi, H.C., Quaas, J., Rivera, J.A., Sathyendranath, S., Smith, S.L., Trewin, B., von Schuckmann, K. and Vose, R.S., 2021. Changing State of the Climate System. In: V. Masson-Delmotte, P. Zhai, A. Pirani, S.L. Connors, C. Péan, S. Berger, N. Caud, Y. Chen, L. Goldfarb, M.I. Gomis, M. Huang, K. Leitzell, E. Lonnoy, J.B.R. Matthews, T.K. Maycock, T. Waterfield, O. Yelekçi, R. Yu and B. Zhou (Editors), Climate Change 2021: The Physical Science Basis. Contribution of Working Group I to the Sixth Assessment Report of the Intergovernmental Panel on Climate Change. Cambridge University Press, Cambridge, United Kingdom and New York, NY, USA, pp. 287–422.

Gurney, S.D., 1998. Aspects of the genesis and geomorphology of pingos: perennial permafrost mounds. Progress in Physical Geography, 22(3): 307-324.

Guth, P.L., Van Niekerk, A., Grohmann, C.H., Muller, J.-P., Hawker, L., Florinsky, I.V., Gesch, D., Reuter, H.I., Herrera-Cruz, V., Riazanoff, S., López-Vázquez, C., Carabajal, C.C., Albinet, C. and Strobl, P., 2021. Digital Elevation Models: Terminology and Definitions. Remote Sensing, 13(18): 3581.

Hall, D.K., Riggs, G.A., Salomonson, V.V., DiGirolamo, N.E. and Bayr, K.J., 2002. MODIS snow-cover products. Remote Sensing of Environment, 83(1): 181-194.

Hallet, B., 1990. Self-organization in freezing soils: from microscopic ice lenses to patterned ground. Canadian Journal of Physics, 68(9): 842-852.

Harlan, M.E., Gleason, C.J., Flores, J.A., Langhorst, T.M. and Roy, S., 2023. Mapping and characterizing Arctic beaded streams through high resolution satellite imagery. Remote Sensing of Environment, 285: 113378.

Harris, C., 2005. Climate Change, Mountain Permafrost Degradation and Geotechnical Hazard. In: U.M. Huber, H.K.M. Bugmann and M.A. Reasoner (Editors), Global Change and Mountain Regions: An Overview of Current Knowledge. Springer Netherlands, Dordrecht, pp. 215-224.

Harris, C. and Lewkowicz, A.G., 1993. Form and internal structure of active-layer detachment slides, Fosheim Peninsula, Ellesmere Island, Northwest Territories, Canada. Canadian Journal of Earth Sciences, 30(8): 1708-1714.

Harris, S.A. and Brown, R.J.E., 1978. Plateau Mountain: A case study of alpine permafrost in the Canadian Rocky Mountains. In: R.J.E. Brown (Editor), 3rd International Conference on Permafrost. National Research Council of Canada, Edmonton, AB, pp. 385-391.

Harris, S.A., French, H.M., Heginbottom, J.A., Johnston, G.H., Ladanyi, B., Sego, D.C. and van Everdingen, R.O., 1988. Glossary of Permafrost and Related Ground-Ice Terms, National Research Council Canada.

Harry, D.G. and Gozdzik, J.S., 1988. Ice wedges: Growth, thaw transformation, and palaeoenvironmental significance. Journal of Quaternary Science, 3(1): 39-55.

Heginbottom, J.A., 2002. Permafrost mapping: a review. Progress in Physical Geography: Earth and Environment, 26(4): 623-642.

Heginbottom, J.A., Brown, J., Melnikov, E.S. and Ferrians Jr., O.J., 1993. Circumarctic Map of Permafrost and Ground Ice Conditions. In: A.W. Lewkowicz (Editor), Permafrost: Sixth International Conference. South China University Press, Beijing, pp. 1132-1136.

Heginbottom, J.A., Dubreuil, M.A. and Harker, P.A., 1995. Canada-Permafrost, National Atlas of Canada , Plate 2.1, Geomatics Canada, National Atlas Information Service and Geological Survey of Canada, MCR.

Herring, T. and Lewkowicz, A.G., 2022. A systematic evaluation of electrical resistivity tomography for permafrost interface detection using forward modeling. Permafrost and Periglacial Processes, 33(2): 134-146.

Hersbach, H., Bell, B., Berrisford, P., Hirahara, S., Horányi, A., Muñoz-Sabater, J., Nicolas, J., Peubey, C., Radu, R., Schepers, D., Simmons, A., Soci, C., Abdalla, S., Abellan, X., Balsamo, G., Bechtold, P., Biavati, G., Bidlot, J., Bonavita, M., De Chiara, G., Dahlgren, P., Dee, D., Diamantakis, M., Dragani, R., Flemming, J., Forbes, R., Fuentes, M., Geer, A., Haimberger, L., Healy, S., Hogan, R.J., Hólm, E., Janisková, M., Keeley, S., Laloyaux, P., Lopez, P., Lupu, C., Radnoti, G., de Rosnay, P., Rozum, I., Vamborg, F., Villaume, S. and Thépaut, J.-N., 2020. The ERA5 global reanalysis. Quarterly Journal of the Royal Meteorological Society, 146(730): 1999-2049.

Hilbich, C., Marescot, L., Huauck, C., Loke, M.H. and Mäusbacher, R., 2009. Applicability of electrical resistivity tomography monitoring to coarse blocky and ice-rich permafrost landforms. Permafrost and Periglacial Processes, 20(3): 269-284.

Hillig, W.B., 1997. Measurement of interfacial free energy for ice/water system. Journal of Crystal Growth, 183(3): 463-468.

Hinkel, K.M., Doolittle, J.A., Bockheim, J.G., Nelson, F.E., Paetzold, R., Kimble, J.M. and Travis, R., 2001. Detection of subsurface permafrost features with ground-penetrating radar, Barrow, Alaska. Permafrost and Periglacial Processes, 12(2): 179-190.

Hinkel, K.M., Frohn, R.C., Nelson, F.E., Eisner, W.R. and Beck, R.A., 2005. Morphometric and spatial analysis of thaw lakes and drained thaw lake basins in the western Arctic Coastal Plain, Alaska. Permafrost and Periglacial Processes, 16(4): 327-341.

Hirsh-Pearson, K., Johnson, C.J., Schuster, R., Wheate, R.D. and Venter, O., 2022. Canada's human footprint reveals large intact areas juxtaposed against areas under immense anthropogenic pressure. FACETS, 7: 398-419.

Hjort, J., Etzelmüller, B. and Tolgensbakk, J., 2010. Effects of scale and data source in periglacial distribution modelling in a high arctic environment, western Svalbard. Permafrost and Periglacial Processes, 21(4): 345-354.

Hjort, J., Karjalainen, O., Aalto, J., Westermann, S., Romanovsky, V.E., Nelson, F.E., Etzelmüller, B. and Luoto, M., 2018. Degrading permafrost puts Arctic infrastructure at risk by mid-century. Nature Communications, 9(1).

Hoelzle, M., 1992. Permafrost occurrence from BTS measurements and climatic parameters in the eastern Swiss Alps. Permafrost and Periglacial Processes, 3(2): 143-147.

Holloway, J.E., Lewkowicz, A.G., Douglas, T.A., Li, X., Turetsky, M.R., Baltzer, J.L. and Jin, H., 2020. Impact of wildfire on permafrost landscapes: A review of recent advances and future prospects. Permafrost and Periglacial Processes, 31(3): 371-382.

Holmes, G.W., Hopkins, D.M. and Foster, H.L., 1968. Pingos in Central Alaska. In: U.S.D.o.t. Interior (Editor). Contributions to General Geology. US Government Printing Office Washington, DC, Washington, DC.

Hoque, M.A. and Pollard, W.H., 2016. Stability of permafrost dominated coastal cliffs in the Arctic. Polar Science, 10(1): 79-88.

Howes, D. and Kenk, E., 1997. Terrain classification system for British Columbia (version 2). Ministry of Environment, Ministry of Crown Lands, Victoria, BC, Canada.

Huang, S.L. and Aughenbaugh, N.B., 1987. Sublimation of Pore ice in Frozen Silt. Journal of Cold Regions Engineering, 1(4): 171-181.

Hughes, O.L., 1969. Distribution of open-system pingos in central Yukon Territory with respect to glacial limits. In: M.a.R. Department of Energy (Editor). Geological Survey of Canada, Ottawa, ON.

Huscroft, C.A., Elliot, B.T. and Lipovsky, P.S., 2020. Yukon Landform Atlas. Yukon Geological Survey, Whitehorse, YT.

Huscroft, C.A., Lipovsky, P.S. and Bond, J.D., 2003. Permafrost and landslide activity: Case studies from southwestern Yukon Territory. In: D.S. Emond and L.L. Lewis (Editors), Yukon Exploration and Geology 2003. Yukon Geological Survey, Whitehorse, YT, pp. 107-119.

Huscroft, C.A., Ward, B.C., Barendregt, R.W., Jr., L.E.J. and Opdyke, N.D., 2004. Pleistocene volcanic damming of Yukon River and the maximum age of the Reid Glaciation, west-central Yukon. Canadian Journal of Earth Sciences, 41(2): 151-164.

Jafarov, E.E., Romanovsky, V.E., Genet, H., McGuire, A.D. and Marchenko, S.S., 2013. The effects of fire on the thermal stability of permafrost in lowland and upland black spruce forests of interior Alaska in a changing climate. Environmental Research letters, 8(3).

Jiskoot, H., 2011. Long-runout rockslide on glacier at Tsar Mountain, Canadian Rocky Mountains: potential triggers, seismic and glaciological implications. Earth Surface Processes and Landforms, 36(2): 203-216.

Jiskoot, H., Murray, T. and Boyle, P., 2000. Controls on the distribution of surge-type glaciers in Svalbard. Journal of Glaciology, 46(154): 412-422.

Jones, B.M., Farquharson, L.M., Baughman, C.A., Buzard, R.M., Arp, C.D., Grosse, G., Bull, D.L., Günther, F., Nitze, I., Urban, F., Kasper, J.L., Frederick, J.M., Thomas, M., Jones, C., Mota, A., Dallimore, S., Tweedie, C., Maio, C., Mann, D.H., Richmond, B., Gibbs, A., Xiao, M., Sachs, T., Iwahana, G., Kanevskiy, M. and Romanovsky, V.E., 2018. A decade of remotely sensed observations highlight complex processes linked to coastal permafrost bluff erosion in the Arctic. Environmental Research Letters, 13(11): 115001.

Jones, B.M., Grosse, G., Farquharson, L.M., Roy-Léveillée, P., Veremeeva, A., Kanevskiy, M.Z., Gaglioti, B.V., Breen, A.L., Parsekian, A.D., Ulrich, M. and Hinkel, K.M., 2022. Lake and drained lake basin systems in lowland permafrost regions. Nature Reviews Earth & Environment, 3(1): 85-98.

Jones, B.M., Grosse, G., Hinkel, K.M., Arp, C.D., Walker, S., Beck, R.A. and Galloway, J.P., 2012. Assessment of pingo distribution and morphometry using an IfSAR derived digital surface model, western Arctic Coastal Plain, Northern Alaska. Geomorphology, 138(1): 1-14.

Jorgenson, M.T., 2013. 8.20 Thermokarst Terrains. In: J.F. Shroder (Editor), Treatise on Geomorphology. Academic Press, San Diego, pp. 313-324.

Jorgenson, M.T. and Shur, Y., 2007. Evolution of lakes and basins in northern Alaska and discussion of the thaw lake cycle. Journal of Geophysical Research: Earth Surface, 112(F2).

Jorgenson, M.T., Y.L. Shur and T.E. Osterkamp, 2008. Thermokarst in Alaska. In: D.L. Kane and K.M. Hinkel (Editors), Ninth International Conference on Permafrost. Institute of Northern Engineering, University of Alaska Fairbanks, Fairbanks, Alaska, pp. 869-876.

Kääb, A., 2008. Remote sensing of permafrost-related problems and hazards. Permafrost and Periglacial Processes, 19(2): 107-136.

Kachurin, S.P., 1964. Crygenic physico-geological phenomena in permafrost regions. National Research Council of Canada, Ottawa, Canada. Translated by C. de Leuchtenberg.

Karjalainen, O., Aalto, J., Kanevskiy, M.Z., Luoto, M. and Hjort, J., 2022. High-resolution predictions of ground ice content for the Northern Hemisphere permafrost region. Earth Syst. Sci. Data Discuss., 2022: 1-40.

Karjalainen, O., Aalto, J., Luoto, M., Westermann, S., Romanovsky, V.E., Nelson, F.E., Etzelmüller, B. and Hjort, J., 2019. Circumpolar permafrost maps and geohazard indices for near-future infrastructure risk assessments. Scientific Data, 6(1): 1-16.

Karjalainen, O., Luoto, M., Aalto, J., Etzelmüller, B., Grosse, G., Jones, B.M., Lilleøren, K.S. and Hjort, J., 2020. High potential for loss of permafrost landforms in a changing climate. Environmental Research Letters, 15(10): 104065.

Kennedy, K., Kinnear, L., Benkert, B., Hennessey, R., Trimbel, R. and Fresco, N., 2011a. Northern Climate ExChange, 2011. Pelly Crossing Landscape Hazards: Geological mapping for climate change adaptation planning, Yukon Research Centre, Yukon College, Whitehorse, Yukon.

Kennedy, K., Kinnear, L., Calmels, F., Bonnaventure, P., Lewkowicz, A.G., Benkert, B., Hennessey, R., Trimbel, R. and Fresco, N., 2011b. Northern Climate ExChange, 2011. Mayo Landscape Hazards: Geological mapping for climate change adaptation planning, Yukon Research Centre, Yukon College, Whitehorse, Yukon.

Kershaw, G.P. and Gill, D., 1979. Growth and decay of palsas and peat plateaus in the Macmillan Pass–Tsichu River area, Northwest Territories, Canada. Canadian Journal of Earth Sciences, 16(7): 1362-1374.

Kneisel, C., Hauck, C., Fortier, R. and Moorman, B., 2008. Advances in geophysical methods for permafrost investigations. Permafrost and Periglacial Processes, 19(2): 157-178.

Kokelj, S., Tunnicliffe, J., Lacelle, D., Lantz, T.C. and Fraser, R.H., 2015a. Retrogressive thaw slumps: From slope process to the landscape sensitivity of northwestern Canada, Proceedings of the 68th Canadian geotechnical conference, GeoQuébec.

Kokelj, S.V. and Burn, C.R., 2005. Near-surface ground ice in sediments of the Mackenzie Delta, Northwest Territories, Canada. Permafrost and Periglacial Processes, 16(3): 291-303.

Kokelj, S.V., Gingras-Hill, T., Daly, S.V., Morse, P., Wolfe, S., Rudy, A.C.A., Sluijs, J.v.d., Weiss, N., O'Neill, B., Baltzer, J., Lantz, T.C., Gibson, C., Cazon, D., Fraser, R.H., Froese, D.G., Giff, G., Klengenberg, C., Lamoureux, S.F., Quinton, W., Turetsky, M.R., Chiasson, A., Ferguson, C., Newton, M., Pope, M., Paul, J.A., Wilson, A. and Young, J., 2023. The Northwest Territories Thermokarst Mapping Collective: A northern-driven mapping collaborative toward understanding the effects of permafrost thaw. Arctic Science, 9(4): 886-918.

Kokelj, S.V. and Jorgenson, M.T., 2013. Advances in Thermokarst Research. Permafrost and Periglacial Processes, 24(2): 108-119.

Kokelj, S.V., Kokoszka, J., van der Sluijs, J., Rudy, A.C.A., Tunnicliffe, J., Shakil, S., Tank, S.E. and Zolkos, S., 2021. Thaw-driven mass wasting couples slopes with downstream systems, and effects propagate through Arctic drainage networks. The Cryosphere, 15(7): 3059-3081.

Kokelj, S.V., Lantz, T.C., Kanigan, J., Smith, S.L. and Coutts, R., 2009. Origin and polycyclic behaviour of tundra thaw slumps, Mackenzie Delta region, Northwest Territories, Canada. Permafrost and Periglacial Processes, 20(2): 173-184.

Kokelj, S.V., Tunnicliffe, J., Lacelle, D., Lantz, T.C., Chin, K.S. and Fraser, R., 2015b. Increased precipitation drives mega slump development and destabilization of ice-rich permafrost terrain, northwestern Canada. Global and Planetary Change, 129: 56-68.

Könönen, O.H., Karjalainen, O., Aalto, J., Luoto, M. and Hjort, J., 2022. Environmental spaces for palsas and peat plateaus are disappearing at a circumpolar scale. The Cryosphere Discuss., 2022: 1-37.

Kotler, E. and Burn, C.R., 2000. Cryostratigraphy of the Klondike "muck" deposits, west-central Yukon Territory. Canadian Journal of Earth Sciences, 37(6): 849-861.

Labrecque, S., Lacelle, D., Duguay, C.R., Lauriol, B. and Hawkings, J., 2009. Contemporary (1951 - 2001) Evolution of Lakes in the Old Crow Basin, Northern Yukon, Canada: Remote Sensing, Numerical Modeling, and Stable Isotope Analysis. Arctic, 62(2): 225-238.

Lacelle, D., Bjornson, J. and Lauriol, B., 2010. Climatic and geomorphic factors affecting contemporary (1950–2004) activity of retrogressive thaw slumps on the Aklavik Plateau, Richardson Mountains, NWT, Canada. Permafrost and Periglacial Processes, 21(1): 1-15.

Lacelle, D., Brooker, A., Fraser, R.H. and Kokelj, S.V., 2015. Distribution and growth of thaw slumps in the Richardson Mountains–Peel Plateau region, northwestern Canada. Geomorphology, 235: 40-51.

Lacelle, D., Fisher, D.A., Verret, M. and Pollard, W., 2022. Improved prediction of the vertical distribution of ground ice in Arctic-Antarctic permafrost sediments. Communications Earth & Environment, 3(1): 31.

Lamoureux, S.F. and Lafrenière, M.J., 2009. Fluvial impact of extensive active layer detachments, Cape Bounty, Melville Island, Canada. Arctic, Antarctic, and Alpine Research, 41(1): 59-68.

Lantuit, H., Overduin, P.P. and Wetterich, S., 2013. Recent Progress Regarding Permafrost Coasts. Permafrost and Periglacial Processes, 24(2): 120-130.

Lantuit, H. and Pollard, W.H., 2008. Fifty years of coastal erosion and retrogressive thaw slump activity on Herschel Island, southern Beaufort Sea, Yukon Territory, Canada. Geomorphology, 95(1): 84-102.

Lantz, T.C. and Kokelj, S.V., 2008. Increasing rates of retrogressive thaw slump activity in the Mackenzie Delta region, N.W.T., Canada. Geophysical Research Letters, 35(6).

Lara, M.J., Genet, H., McGuire, A.D., Euskirchen, E.S., Zhang, Y., Brown, D.R.N., Jorgenson, M.T., Romanovsky, V., Breen, A. and Bolton, W.R., 2016. Thermokarst rates intensify due to climate change and forest fragmentation in an Alaskan boreal forest lowland. Global Change Biology, 22(2): 816-829.

Laxton, S. and Coates, J., 2010. Geophysical and borehole investigations of permafrost conditions associated with compromised infrastructure in Dawson and Ross River, Yukon. In: K.E. MacFarlane, L.H. Weston and C. Relf (Editors), Yukon Exploration and Geology 2010. Yukon Geological Survey, Whitehorse, YT, pp. 135-148.

Legendre, M., Lartigue, A., Bertaux, L., Jeudy, S., Bartoli, J., Lescot, M., Alempic, J.-M., Ramus, C., Bruley, C., Labadie, K., Shmakova, L., Rivkina, E., Couté, Y., Abergel, C. and Claverie, J.-M., 2015. In-depth study of *Mollivirus sibericum*, a new 30,000-y-old giant virus infecting *Acanthamoeba*. Proceedings of the National Academy of Sciences, 112(38).

Lenton, T.M., 2012. Arctic Climate Tipping Points. AMBIO, 41(1): 10-22.

Levy, J.S., Fountain, A.G., Dickson, J.L., Head, J.W., Okal, M., Marchant, D.R. and Watters, J., 2013. Accelerated thermokarst formation in the McMurdo Dry Valleys, Antarctica. Scientific Reports, 3(1): 2269.

Lewkowicz, A.G., 2007. Dynamics of active-layer detachment failures, Fosheim Peninsula, Ellesmere Island, Nunavut, Canada. Permafrost and Periglacial Processes, 18(1): 89-103.

Lewkowicz, A.G. and Bonnaventure, P.P., 2011. Equivalent Elevation: A New Method to Incorporate Variable Surface Lapse Rates into Mountain Permafrost Modelling. Permafrost and Periglacial Processes, 22(2): 153-162.

Lewkowicz, A.G., Etzelmüller, B. and Smith, S.L., 2011. Characteristics of Discontinuous Permafrost based on Ground Temperature Measurements and Electrical Resistivity Tomography, Southern Yukon, Canada. Permafrost and Periglacial Processes, 22(4): 320-342.

Lewkowicz, A.G. and Harris, C., 2005. Frequency and magnitude of active-layer detachment failures in discontinuous and continuous permafrost, northern Canada. Permafrost and Periglacial Processes, 16(1): 115-130.

Lewkowicz, A.G. and Way, R.G., 2019. Extremes of summer climate trigger thousands of thermokarst landslides in a High Arctic environment. Nature Communications, 10(1): 1329.

Lewkowicz, A.G., Way, R.G., Hermanutz, L., Trant, A., Siegwart Collier, L. and Whitaker, D., 2017. Interactions between shrubs and permafrost in the Torngat Mountains, Northern Labrador, Canada. AGUFM 2017.

Li, C., Wei, Y., Liu, Y., Li, L., Peng, L., Chen, J., Liu, L., Dou, T. and Wu, X., 2022a. Active Layer Thickness in the Northern Hemisphere: Changes From 2000 to 2018 and Future Simulations. Journal of Geophysical Research: Atmospheres, 127(12): e2022JD036785.

Li, G., Zhang, M., Pei, W., Melnikov, A., Khristoforov, I., Li, R. and Yu, F., 2022b. Changes in permafrost extent and active layer thickness in the Northern Hemisphere from 1969 to 2018. Science of The Total Environment, 804: 150182.

Liestøl, O., 1996. Open-system pingos in Spitsbergen. Norsk Geografisk Tidsskrift - Norwegian Journal of Geography, 50(1): 81-84.

Lindgren, P.R., Farquharson, L.M., Romanovsky, V.E. and Grosse, G., 2021. Landsat-based lake distribution and changes in western Alaska permafrost regions between the 1970s and 2010s. Environmental Research Letters, 16(2): 025006.

Lindsay, C., Zhu, J., Miller, A.E., Kirchner, P. and Wilson, T.L., 2015. Deriving Snow Cover Metrics for Alaska from MODIS. Remote Sensing, 7(10): 12961-12985.

Lipovsky, P.S., Coates, J., Lewkowicz, A.G. and Trochim, E., 2005. Active-layer detachments following the summer 2004 forest fires near Dawson City, Yukon. In: D.S. Emond, G.D. Bradshaw, L.L. Lewis and L.H. Weston (Editors), Yukon Exploration and Geology 2005. Yukon Geological Survey, Whitehorse, YT, pp. 175-194.

Loch, J.P.G., 1978. Thermodynamic equilibrium between ice and water in porous media. Soil Science, 126(2): 77-80.

Lookingbill, T.R. and Urban, D.L., 2005. Gradient analysis, the next generation: towards more plant-relevant explanatory variables. Canadian Journal of Forest Research, 35(7): 1744-1753.

Lousada, M., Pina, P., Vieira, G., Bandeira, L. and Mora, C., 2018. Evaluation of the use of very high resolution aerial imagery for accurate ice-wedge polygon mapping (Adventdalen, Svalbard). Science of The Total Environment, 615: 1574-1583.

Lundqvist, J., 1969. Earth and ice mounds: a terminological discussion. The periglacial environment: 203-215.

Luo, J., Niu, F., Lin, Z., Liu, M., Yin, G. and Gao, Z., 2022. Inventory and Frequency of Retrogressive Thaw Slumps in Permafrost Region of the Qinghai–Tibet Plateau. Geophysical Research Letters, 49(23): e2022GL099829.

Mackay, J.R., 1972. The world of underground ice. Annals of the Association of American Geographers, 62(1): 1-22.

Mackay, J.R., 1974. Reticulate ice veins in permafrost, Northern Canada. Canadian Geotechnical Journal, 11(2): 230-237.

Mackay, J.R., 1979. Pingos of the Tuktoyaktuk Peninsula Area, Northwest Territories. Géographie physique et Quaternaire, 33(1): 3-61.

Mackay, J.R., 1990. Some observations on the growth and deformation of epigenetic, syngenetic and anti-syngenetic ice wedges. Permafrost and Periglacial Processes, 1(1): 15-29.

Mackay, J.R., 1998. Pingo Growth and collapse, Tuktoyaktuk Peninsula Area, Western Arctic Coast, Canada: a long-term field study. Géographie physique et Quaternaire, 52(3): 271-323.

MacKay, J.R., 2000. Thermally induced movements in ice-wedge polygons, western arctic coast: a long-term study. Géographie physique et Quaternaire, 54(1): 41-68.

Mackay, J.R. and Burn, C.R., 2011. A Century (1910–2008) of Change in a Collapsing Pingo, Parry Peninsula, Western Arctic Coast, Canada. Permafrost and Periglacial Processes, 22(3): 266-272.

Mackay, J.R., Rampton, V.N. and Fyles, J.G., 1972. Relic Pleistocene Permafrost, Western Arctic, Canada. Science, 176(4041): 1321-1323.

Malone, L., Lacelle, D., Kokelj, S. and Clark, I.D., 2013. Impacts of hillslope thaw slumps on the geochemistry of permafrost catchments (Stony Creek watershed, NWT, Canada). Chemical Geology, 356: 38-49.

Matthews, J.A., Dahl, S.-O., Berrisford, M.S. and Nesje, A., 1997. Cyclic Development and Thermokarstic Degradation of Palsas in the Mid-Alpine Zone at Leirpullan, Dovrefjell, Southern Norway. Permafrost and Periglacial Processes, 8(1): 107-122.

Mesquita, P., Wrona, F. and Prowse, T., 2008. Effects of retrogressive thaw slumps on sediment chemistry, submerged macrophyte biomass, and invertebrate abundance of upland tundra lakes. In: D.L. Kane and K.M. Hinkel (Editors), Ninth International Conference on Permafrost. Institute of Northern Engineering, University of Alaska Fairbanks Fairbanks …, pp. 1185-1190.

Minár, J., Evans, I.S. and Jenčo, M., 2020. A comprehensive system of definitions of land surface (topographic) curvatures, with implications for their application in geoscience modelling and prediction. Earth-Science Reviews, 211: 103414.

Morgenstern, A., Grosse, G. and Schirrmeister, L., 2008. Genetic, Morphological, and Statistical Characterization of Lakes in the Permafrost-Dominated Lena Delta. In: D.L. Kane and K.M. Hinkel (Editors), Ninth International

Conference on Permafrost. Institute of Northern Engineering, University of Alaska Fairbanks, Fairbanks, Alaska, pp. 1239-1244.

Morgenstern, A., Ulrich, M., Günther, F., Roessler, S., Fedorova, I.V., Rudaya, N.A., Wetterich, S., Boike, J. and Schirrmeister, L., 2013. Evolution of thermokarst in East Siberian ice-rich permafrost: A case study. Geomorphology, 201: 363-379.

Morice, C.P., Kennedy, J.J., Rayner, N.A., Winn, J.P., Hogan, E., Killick, R.E., Dunn, R.J.H., Osborn, T.J., Jones, P.D. and Simpson, I.R., 2021. An Updated Assessment of Near-Surface Temperature Change From 1850: The HadCRUT5 Data Set. Journal of Geophysical Research: Atmospheres, 126(3): e2019JD032361.

Mortensen, J.K., 1992. Pre-Mid-Mesozoic tectonic evolution of the Yukon-Tanana Terrane, Yukon and Alaska. Tectonics, 11(4): 836-853.

Munroe, J.S., Doolittle, J.A., Kanevskiy, M.Z., Hinkel, K.M., Nelson, F.E., Jones, B.M., Shur, Y. and Kimble, J.M., 2007. Application of ground-penetrating radar imagery for three-dimensional visualisation of near-surface structures in ice-rich permafrost, Barrow, Alaska. Permafrost and Periglacial Processes, 18(4): 309-321.

Murton, J.B., 2009. Global Warming and Thermokarst. In: R. Margesin (Editor), Permafrost Soils. Springer Berlin Heidelberg, Berlin, Heidelberg, pp. 185-203.

Murton, J.B. and French, H.M., 1994. Cryostructures in permafrost, Tuktoyaktuk coastlands, western arctic Canada. Canadian Journal of Earth Sciences, 31(4): 737-747.

Murton, J.B., Peterson, R. and Ozouf, J.-C., 2006. Bedrock Fracture by Ice Segregation in Cold Regions. Science, 314(5802): 1127-1129.

Myers-Smith, I.H., Forbes, B.C., Wilmking, M., Hallinger, M., Lantz, T., Blok, D., Tape, K.D., Macias-Fauria, M., Sass-Klaassen, U., Lévesque, E., Boudreau, S., Ropars, P., Hermanutz, L., Trant, A., Collier, L.S., Weijers, S., Rozema, J., Rayback, S.A., Schmidt, N.M., Schaepman-Strub, G., Wipf, S., Rixen, C., Ménard, C.B., Venn, S., Goetz, S., Andreu-Hayles, L., Elmendorf, S., Ravolainen, V., Welker, J., Grogan, P., Epstein, H.E. and Hik, D.S., 2011. Shrub expansion in tundra ecosystems: dynamics, impacts and research priorities. Environmental Research Letters, 6(4): 045509.

Natural Resources Canada, 2013. Canadian Digital Elevation Model, Government of Canada, Ottawa, ON.

Natural Resources Canada, 2022. High Resolution Digital Elevation Model (HRDEM). In: G.o.C. Natural Resources Canada (Editor), Ottawa, ON.

Nelder, J.A. and Wedderburn, R.W.M., 1972. Generalized Linear Models. Journal of the Royal Statistical Society. Series A (General), 135(3): 370-384.

Nelson, F.E., Anisimov, O.A. and Shiklomanov, N.I., 2002. Climate Change and Hazard Zonation in the Circum-Arctic Permafrost Regions. Natural Hazards, 26(3): 203-225.

Nelson, F.E., Barendregt, R.W. and Villeneuve, M., 2009. Stratigraphy of the Fort Selkirk Volcanogenic Complex in central Yukon and its paleoclimatic significance: Ar/Ar and paleomagnetic data. Canadian Journal of Earth Sciences, 46(5): 381-401.

Nelson, F.E., Shiklomanov, N.I. and Nyland, K.E., 2021. Cool, CALM, collected: the Circumpolar Active Layer Monitoring program and network. Polar Geography, 44(3): 155-166.

Nitze, I., Heidler, K., Barth, S. and Grosse, G., 2021. Developing and Testing a Deep Learning Approach for Mapping Retrogressive Thaw Slumps. Remote Sensing, 13(21): 4294.

Niu, F., Lin, Z., Lu, J., Luo, J. and Wang, H., 2015. Assessment of terrain susceptibility to thermokarst lake development along the Qinghai–Tibet engineering corridor, China. Environmental Earth Sciences, 73(9): 5631-5642.

Niu, F., Luo, J., Lin, Z., Liu, M. and Yin, G., 2014. Morphological Characteristics of Thermokarst Lakes along the Qinghai-Tibet Engineering Corridor. Arctic, Antarctic, and Alpine Research, 46(4): 963-974.

Nolan, M., 2018. Fairbanks Fodar, Fairbanks, AK. https://fairbanksfodar.com/ (Accessed Dec 2024).

Northwest Territories Geological Survey, 2019. Northwest Territories Thermokarst Mapping Collective. Northwest Territories Geological Survey, Yellowknife, NWT.

Nossov, D.R., Jorgenson, M.T., Kielland, K. and Kanevskiy, M.Z., 2013. Edaphic and microclimatic controls over permafrost response to fire in interior Alaska. Environmental Research Letters, 8(3): 035013.

O'Neill, H.B., Roy-Leveillee, P., Lebedeva, L. and Ling, F., 2020. Recent advances (2010–2019) in the study of taliks. Permafrost and Periglacial Processes, 31(3): 346-357.

O'Neill, H.B., Wolfe, S.A. and Duchesne, C., 2019. New ground ice maps for Canada using a paleogeographic modelling approach. The Cryosphere, 13(3): 753-773.

O'Neill, H.B., Wolfe, S.A. and Duchesne, C., 2022. Ground ice map of Canada, Version 1.1. Geological Survey of Canada.

Obu, J., 2021. How Much of the Earth's Surface is Underlain by Permafrost? Journal of Geophysical Research: Earth Surface, 126(5): e2021JF006123.

Obu, J., Westermann, S., Bartsch, A., Berdnikov, N., Christiansen, H.H., Dashtseren, A., Delaloye, R., Elberling, B., Etzelmüller, B., Kholodov, A., Khomutov, A., Kääb, A., Leibman, M.O., Lewkowicz, A.G., Panda, S.K., Romanovsky, V., Way, R.G., Westergaard-Nielsen, A., Wu, T., Yamkhin, J. and Zou, D., 2019. Northern Hemisphere permafrost map based on TTOP modelling for 2000–2016 at 1 km^2 scale. Earth-Science Reviews, 193: 299-316.

Ohlmacher, G.C., 2007. Plan curvature and landslide probability in regions dominated by earth flows and earth slides. Engineering Geology, 91(2): 117-134.

Olefeldt, D., Goswami, S., Grosse, G., Hayes, D., Hugelius, G., Kuhry, P., McGuire, A.D., Romanovsky, V.E., Sannel, A.B.K., Schuur, E.A.G. and Turetsky, M.R., 2016. Circumpolar distribution and carbon storage of thermokarst landscapes. Nature Communications, 7(1): 13043.

Orlov, T.V., Victorov, A.S., Arkhipova, M.V. and Zverev, A.V., 2020. Impact assessment and stochastic modeling of morphometric parameters of thermokarst hazard for unpaved roads. Geography, Environment, Sustainability, 13(4): 98-106.

Pearson, C.A., 2020. Quantifying recent thermokarst changes in the Northwest Territories, Canada and Alaska, USA using ArcticDEM, University of Exeter, Exeter, United Kingdom, 135 pp.

Perovich, D.K., 2007. Light reflection and transmission by a temperate snow cover. Journal of Glaciology, 53(181): 201-210.

Péwé, T.L., 1963. Ice-wedges in Alaska - Classification, Distribution, and Climatic Significance, Permafrost International Conference. National Academy of Sciences - National Research Council, Lafayette, Indiana, pp. 76-81.

Pierce, K.B., Lookingbill, T. and Urban, D., 2005. A simple method for estimating potential relative radiation (PRR) for landscape-scale vegetation analysis. Landscape Ecology, 20(2): 137-147.

Poggio, L., de Sousa, L.M., Batjes, N.H., Heuvelink, G.B.M., Kempen, B., Ribeiro, E. and Rossiter, D., 2021. SoilGrids 2.0: producing soil information for the globe with quantified spatial uncertainty. SOIL, 7(1): 217-240.

Porter, C.M., Paul; Howat, Ian; Noh, Myoung-Jon; Bates, Brian; Peterman, Kenneth; Keesey, Scott; Schlenk, Matthew; Gardiner, Judith; Tomko, Karen; Willis, Michael; Kelleher, Cole; Cloutier, Michael; Husby, Eric; Foga, Steven; Nakamura, Hitomi; Platson, Melisa; Wethington, Michael, Jr.; Williamson, Cathleen; Bauer, Gregory; Enos, Jeremy; Arnold, Galen; Kramer, William; Becker, Peter; Doshi, Abhijit; D'Souza, Cristelle; Cummens, Pat; Laurier, Fabien; Bojesen, Mikkel, 2018. ArcticDEM, Version 3. In: P.G. Centre (Editor). Harvard Dataverse, V1.

Price, L.W., 1991. Subsurface Movement on Solifluction Slopes in the Ruby Range, Yukon Territory, Canada — A 20-Year Study. Arctic and Alpine Research, 23(2): 200-205.

R Core Team, 2022. R: A Language and Environment for Statistical Computing. R Foundation for Statistical Computing, Vienna, Austria.

Ran, Y., Li, X., Cheng, G., Che, J., Aalto, J., Karjalainen, O., Hjort, J., Luoto, M., Jin, H., Obu, J., Hori, M., Yu, Q. and Chang, X., 2022. New high-resolution estimates of the permafrost thermal state and hydrothermal conditions over the Northern Hemisphere. Earth Syst. Sci. Data, 14(2): 865-884.

Raynolds, M.K., Walker, D.A., Ambrosius, K.J., Brown, J., Everett, K.R., Kanevskiy, M., Kofinas, G.P., Romanovsky, V.E., Shur, Y. and Webber, P.J., 2014. Cumulative geoecological effects of 62 years of infrastructure and climate change in ice-rich permafrost landscapes, Prudhoe Bay Oilfield, Alaska. Global Change Biology, 20(4): 1211-1224.

Richter, H., 1962. Eine neue Methode der grossmasstäbigen Kartierung des Reliefs. Petermanns Geographische Mitteilungen, 106: 309-312.

Riegel, R.P., Alves, D.D., Schmidt, B.C., de Oliveira, G.G., Haetinger, C., Osório, D.M.M., Rodrigues, M.A.S. and de Quevedo, D.M., 2020. Assessment of susceptibility to landslides through geographic information systems and the logistic regression model. Natural Hazards, 103(1): 497-511.

Rieke, R.D., Vinson, T.S. and Mageau, D.W., 1982. The role of specific surface area and related index properties in the frost susceptibility of soils, 4th. International Conference on Permafrost, Fairbanks, Alaska.

Roddick, J.A., 1967. Tintina Trench. The Journal of Geology, 75(1): 23-33.

Romanovsky, V.E., Smith, S.L. and Christiansen, H.H., 2010. Permafrost thermal state in the polar Northern Hemisphere during the international polar year 2007–2009: a synthesis. Permafrost and Periglacial Processes, 21(2): 106-116.

Roy-Léveillée, P. and Burn, C.R., 2017. Old Crow Flats: Thermokarst Lakes in the Forest–Tundra Transition. In: O. Slaymaker (Editor), Landscapes and Landforms of Western Canada. Springer, Cham, pp. 267-276.

Rudy, A.C.A., Lamoureux, S.F., Treitz, P. and van Ewijk, K.Y., 2016. Transferability of regional permafrost disturbance susceptibility modelling using generalized linear and generalized additive models. Geomorphology, 264: 95-108.

Saito, K., Machiya, H., Iwahana, G., Ohno, H. and Yokohata, T., 2020. Mapping simulated circum-Arctic organic carbon, ground ice, and vulnerability of ice-rich permafrost to degradation. Progress in Earth and Planetary Science, 7(1): 31.

Saito, K., Machiya, H., Iwahana, G., Yokohata, T. and Ohno, H., 2021. Numerical model to simulate long-term soil organic carbon and ground ice budget with permafrost and ice sheets (SOC-ICE-v1.0). Geosci. Model Dev., 14(1): 521-542.

Schädel, C., Bader, M.K.F., Schuur, E.A.G., Biasi, C., Bracho, R., Čapek, P., De Baets, S., Diáková, K., Ernakovich, J., Estop-Aragones, C., Graham, D.E., Hartley, I.P., Iversen, C.M., Kane, E., Knoblauch, C., Lupascu, M., Martikainen, P.J., Natali, S.M., Norby, R.J., O'Donnell, Jonathan A., Chowdhury, T.R., Šantrůčková, H., Shaver, G., Sloan, Victoria L., Treat, C.C., Turetsky, M.R., Waldrop, M.P. and Wickland, K.P., 2016. Potential carbon emissions dominated by carbon dioxide from thawed permafrost soils. Nature Climate Change, 6(10): 950-953.

Schirrmeister, L., Froese, D., Tumskoy, V., Grosse, G. and Wetterich, S., 2013. Yedoma: Late Pleistocene Ice-Rich Syngenetic Permafrost of Beringia. In: S.A. Elias and C.J. Mock (Editors), Encyclopedia of Quaternary Science.

Schrott, L., 1998. The hydrological significance of high mountain permafrost and its relation to solar radiation. A case study in the high Andes of San Juan, Argentina. Bamberger Geographische Schriften, 15: 71-84.

Schuur, E.A.G. and Abbott, B., 2011. High risk of permafrost thaw. Nature, 480(7375): 32-33.

Schuur, E.A.G., McGuire, A.D., Schädel, C., Grosse, G., Harden, J.W., Hayes, D.J., Hugelius, G., Koven, C.D., Kuhry, P., Lawrence, D.M., Natali, S.M., Olefeldt, D., Romanovsky, V.E., Schaefer, K., Turetsky, M.R., Treat, C.C. and Vonk, J.E., 2015. Climate change and the permafrost carbon feedback. Nature, 520(7546): 171-179.

Seppälä, M., 1988. Palsas and related forms. In: M.J. Clark (Editor), Advances in periglacial geomorphology. John Wiley, Chichester, pp. 247-278.

Seppälä, M., 2006. Palsa mires in Finland. In: T. Lindholm and R. Heikkilä (Editors), The Finnish Environment, pp. 155-162.

Serreze, M.C. and Barry, R.G., 2011. Processes and impacts of Arctic amplification: A research synthesis. Global and Planetary Change, 77(1): 85-96.

Shur, Y.L. and Jorgenson, M.T., 1998. Cryostructure development on the floodplain of the Colville River Delta, northern Alaska, Proceedings of the Seventh International Conference on Permafrost. Centre d'études nordiques, Université Laval, Québec: Yellowknife, Canada, pp. 993-1000.

Shur, Y.L. and Jorgenson, M.T., 2007. Patterns of permafrost formation and degradation in relation to climate and ecosystems. Permafrost and Periglacial Processes, 18(1): 7-19.

Smith, M.W. and Riseborough, D.W., 2002. Climate and the limits of permafrost: a zonal analysis. Permafrost and Periglacial Processes, 13(1): 1-15.

Smith, S., Burgess, M. and Riseborough, D., 2008. Ground temperature and thaw settlement in frozen peatlands along the Norman Wells pipeline corridor, NWT Canada: 22 years of monitoring. In: D.L. Kane and K.M. Hinkel (Editors), Ninth International Conference on Permafrost. Institute of Northern Engineering, University of Alaska Fairbanks, Fairbanks, Alaska, pp. 1665-1670.

Smith, S.L., O'Neill, H.B., Isaksen, K., Noetzli, J. and Romanovsky, V.E., 2022. The changing thermal state of permafrost. Nature Reviews Earth & Environment, 3(1): 10-23.

Soloviev, P.A., 1962. Alas relief of Central Yakutia and its formation, Permafrost and accompanying phenomena on the territory of the Yakutian ASSR. USSR Academy of Sceinces, Moscow, USSR.

Spencer, W., Rustigian, H., Scheller, R. and Strittholt, J., 2007. Baseline evaluation of fisher habitat and population status in the southern Sierra Nevada. Produced by the Conservation Biology Institute.

St. Pierre, K.A., Zolkos, S., Shakil, S., Tank, S.E., St. Louis, V.L. and Kokelj, S.V., 2018. Unprecedented Increases in Total and Methyl Mercury Concentrations Downstream of Retrogressive Thaw Slumps in the Western Canadian Arctic. Environmental Science & Technology, 52(24): 14099-14109.

Statistics Canada, 2021. 2021 Census of Population, Ottawa, Ontario.

Statistics Canada, 2023. Population estimates, quarterly. In: S. Canada (Editor), Table 17-10-0009-01, Ottawa, ON.

Steedman, A.E., Lantz, T.C. and Kokelj, S.V., 2017. Spatio-Temporal Variation in High-Centre Polygons and Ice-Wedge Melt Ponds, Tuktoyaktuk Coastlands, Northwest Territories. Permafrost and Periglacial Processes, 28(1): 66-78.

Stiling, P., 2001. Ecology: Theories and Applications. Prentice Hall, Lebanon, IN, U.S.A.

Strauss, J., Schirrmeister, L., Wetterich, S. and Kunitsky, V., 2014. Yedoma - loess or not loess - that's the question, 4th European Conference on Permafrost. University of Lisbon and the University of Évora, Évora, Portugal.

Swanson, D.K. and Nolan, M., 2018. Growth of Retrogressive Thaw Slumps in the Noatak Valley, Alaska, 2010–2016, Measured by Airborne Photogrammetry. Remote Sensing, 10(7): 983.

Swindles, G.T., Morris, P.J., Mullan, D., Watson, E.J., Turner, T.E., Roland, T.P., Amesbury, M.J., Kokfelt, U., Schoning, K., Pratte, S., Gallego-Sala, A., Charman, D.J., Sanderson, N., Garneau, M., Carrivick, J.L., Woulds, C., Holden, J., Parry, L. and Galloway, J.M., 2015. The long-term fate of permafrost peatlands under rapid climate warming. Scientific Reports, 5(1): 17951.

Taber, S., 1929. Frost Heaving. Journal of Geology, 37(5): 428-461.

Turetsky, M.R., Abbott, B.W., Jones, M.C., Walter Anthony, K., Olefeldt, D., Schuur, E.A., Koven, C., McGuire, A.D., Grosse, G., Kuhry, P., Hugelius, G., Lawrence, D.M., Gibson, C. and Sannel, A.B.K., 2019. Permafrost collapse is accelerating carbon release. Nature, 569(7754): 32-34.

Umbrella Final Agreement, 1992. between the Government of Canada, the Council for Yukon Indians and the Government of the Yukon. https://www.rcaanc-cirnac.gc.ca/eng/1297278586814/1542811130481 (Accessed Dec 2023).

van Brahana, J., 2008. Karst Aquifers. In: S.W. Trimble (Editor), Encyclopedia of Water Science (2nd ed.). CRC Press, Boca Raton, FL, pp. 693-697.

Van Dam, R.L., 2012. Landform characterization using geophysics—Recent advances, applications, and emerging tools. Geomorphology, 137(1): 57-73.

van Huissteden, J., Berrittella, C., Parmentier, F.J.W., Mi, Y., Maximov, T.C. and Dolman, A.J., 2011. Methane emissions from permafrost thaw lakes limited by lake drainage. Nature Climate Change, 1(2): 119-123.

Veremeeva, A. and Glushkova, N., 2016. Formation of relief in the regions of Ice Complex deposits distribution: remote sensing and GIS studies in the Kolyma lowland tundra. Earth's Cryosphere, XX(1): 14-24.

Vionnet, V., Mortimer, C., Brady, M., Arnal, L. and Brown, R., 2021. Canadian historical Snow Water Equivalent dataset (CanSWE, 1928–2020). Earth Syst. Sci. Data, 13(9): 4603-4619.

Vtyurin, B.I., 1989. Ground ice on Svalbard. Polar Geography and Geology, 13(1): 1-8.

Walter, K.M., Edwards, M.E., Grosse, G., Zimov, S.A. and Chapin, F.S., 2007. Thermokarst Lakes as a Source of Atmospheric CH_4 During the Last Deglaciation. Science, 318(5850): 633-636.

Walter, K.M., Zimov, S.A., Chanton, J.P., Verbyla, D. and Chapin, F.S., 2006. Methane bubbling from Siberian thaw lakes as a positive feedback to climate warming. Nature, 443(7107): 71-75.

Wang, R., Guo, L., Yang, Y., Zheng, H., Liu, L., Jia, H., Diao, B. and Liu, J., 2023. Thermokarst Lake Susceptibility Assessment Induced by Permafrost Degradation in the Qinghai-Tibet Plateau Using Machine Learning Methods. Remote Sensing, 15(13): 3331.

Warner, B.G., Rubec, C.D.A., Canada Committee on Ecological Land Classification. National Wetlands Working, G., Canadian Wildlife, S. and University of Waterloo. Wetlands Research, C., 1997. The Canadian wetland classification system. University of Waterloo, Wetlands Research Centre, Waterloo, ON.

Washburn, A.L., 1956. Classification of Patterned Ground and Review of Suggested Origins. Bulletin of the Geological Society of America, 67: 823-866.

Washburn, A.L., 1980. Geocryology: A survey of periglacial processes and environments. John Wiley & Sons, NY.

Watanabe, K., 2002. Relationship between growth rate and supercooling in the formation of ice lenses in a glass powder. Journal of Crystal Growth, 237-239: 2194-2198.

Way, R.G. and Lapalme, C.M., 2021. Does tall vegetation warm or cool the ground surface? Constraining the ground thermal impacts of upright vegetation in northern environments. Environmental Research Letters, 16(5): 054077.

Webb, E.E. and Liljedahl, A.K., 2023. Diminishing lake area across the northern permafrost zone. Nature Geoscience, 16(3): 202-209.

Wei, Z., Du, Z., Wang, L., Lin, J., Feng, Y., Xu, Q. and Xiao, C., 2021. Sentinel-Based Inventory of Thermokarst Lakes and Ponds Across Permafrost Landscapes on the Qinghai-Tibet Plateau. Earth and Space Science, 8(11): e2021EA001950.

Westermann, S., Duguay, C.R., Grosse, G. and Kääb, A., 2015. Remote sensing of permafrost and frozen ground. In: M. Tedesco (Editor), Remote Sensing of the Cryosphere. Wiley, pp. 307-344.

Williams, P.J. and Smith, M.W., 1989. The Frozen Earth: Fundamentals of Geocryology. Studies in Polar Research. Cambridge University Press, Cambridge.

Wolfe, S., Murton, J., Bateman, M. and Barlow, J., 2020. Oriented-lake development in the context of late Quaternary landscape evolution, McKinley Bay Coastal Plain, western Arctic Canada. Quaternary Science Reviews, 242: 106414.

Wolfe, S.A., Morse, P.D., Parker, R. and Phillips, M.R., 2023. Distribution and morphometry of pingos, western Canadian Arctic, Northwest Territories, Canada. Geomorphology, 431: 108694.

Woo, M.-k., Lewkowicz, A.G. and Rouse, W.R., 1992. Response of the Canadian permafrost environment to climatic change. Physical Geography, 13(4): 287-317.

Wu, T., Li, S., Cheng, G. and Nan, Z., 2005. Using ground-penetrating radar to detect permafrost degradation in the northern limit of permafrost on the Tibetan Plateau. Cold Regions Science and Technology, 41(3): 211-219.

Wysocki, D.A., Schoeneberger, P.J. and LaGarry, H., 2000. Geomorphology of soil landscapes. Handbook of soil science, 1: 315-321.

Yin, G., Luo, J., Niu, F., Lin, Z. and Liu, M., 2021. Machine learning-based thermokarst landslide susceptibility modeling across the permafrost region on the Qinghai-Tibet Plateau. Landslides, 18(7): 2639-2649.

Yoshikawa, K., Bolton, W.R., Romanovsky, V.E., Fukuda, M. and Hinzman, L.D., 2002. Impacts of wildfire on the permafrost in the boreal forests of Interior Alaska. Journal of Geophysical Research: Atmospheres, 107(D1): FFR 4-1-FFR 4-14.

Young, J.M., Alvarez, A., van der Sluijs, J., Kokelj, S.V., Rudy, A., McPhee, A., Stoker, B.J., Margold, M. and Froese, D., 2022. Recent Intensification (2004–2020) of Permafrost Mass-Wasting in the Central Mackenzie Valley Foothills Is a Legacy of Past Forest Fire Disturbances. Geophysical Research Letters, 49(24): e2022GL100559.

Yukon Ecoregions Working Group, 2004a. Ecoregions of the Yukon Territory: Biophysical properties of Yukon landscapes. In: C.A.S. Smith, J.C. Meikle, C.F. Roots and G. Yukon Ecoregions Working (Editors). Agriculture and Agri-Food Canada, Summerland, BC, pp. 313.

Yukon Ecoregions Working Group, 2004b. Klondike Plateau. In: C.A.S. Smith, J.C. Meikle, C.F. Roots and G. Yukon Ecoregions Working (Editors), Ecoregions of the Yukon Territory: Biophysical properties of Yukon landscapes. Agriculture and Agri-Food Canada, Summerland, BC, pp. 313.

Yukon Geological Survey, 2020a. Surficial Geology Dataset, Whitehorse, YT.

Yukon Geological Survey, 2020b. Yukon Glacial Limits, Whitehorse, YT.

Zevenbergen, L.W. and Thorne, C.R., 1987. Quantitative analysis of land surface topography. Earth Surface Processes and Landforms, 12(1): 47-56.

Zhang, T., Heginbottom, J.A., Barry, R.G. and Brown, J., 2000. Further statistics on the distribution of permafrost and ground ice in the Northern Hemisphere. Polar Geography, 24(2): 126-131.

Zoltai, S.C., 1975. Tree Ring Record of Soil Movements on Permafrost. Arctic and Alpine Research, 7(4): 331-340.

Zoltai, S.C. and Tarnocai, C., 1974. Soils and vegetation of hummocky terrain, no. 74-5. Environmental-Social Committee, Northern Pipelines, Task Force on Northern Oil Development, Ottawa.

Zoltai, S.C. and Tarnocai, C., 1975. Perennially Frozen Peatlands in the Western Arctic and Subarctic of Canada. Canadian Journal of Earth Sciences, 12(1): 28-43.

Zoltai, S.C. and Vitt, D.H., 1995. Canadian wetlands: Environmental gradients and classification. Vegetatio, 118(1): 131-137.

Zwieback, S. and Meyer, F.J., 2021. Top-of-permafrost ground ice indicated by remotely sensed late-season subsidence. The Cryosphere, 15(4): 2041-2055.

Appendix

Landform polygons and morphometry values will be made available in an online data repository.